

Abstract

HUNG, FRANCISCO RODOLFO. Capillary Condensation and Freezing of Simple Fluids Confined in Cylindrical Nanopores. (Under the direction of Keith E. Gubbins).

We present a molecular simulation study aimed at understanding the phase behavior of pure simple fluids, when they are confined inside nanopores of cylindrical geometry. In this situation, new surface-driven phases can appear, and phase transitions typical of bulk systems (gas-liquid, freezing) can be shifted to different conditions. A fundamental understanding of these phenomena is necessary for applications in separations, catalysis and nanotechnology. Studies of these phenomena can also provide important insights on the effect of surface forces, confinement and reduced dimensionality on the phase behavior of host molecules. We have performed two independent, but directly related studies: (1) freezing of carbon tetrachloride within multi-walled carbon nanotubes (MWCNT) of different diameters, and (2) capillary condensation and freezing of krypton within templated mesoporous silica materials (MCM-41). MWCNT and MCM-41 are representative of materials with strongly and weakly attractive walls, respectively. In the first part of this project, the structure and thermodynamic stability of the confined phases, as well as the temperatures and the order of the phase transitions were determined using dielectric relaxation spectroscopy measurements and Monte Carlo simulations in the grand canonical ensemble. A rich phase behavior with multiple transition temperatures was observed for such systems. In the second part of this project we developed realistic, atomistic models of MCM-41 type materials that include pore surface roughness and morphological defects in agreement with experimental results. Grand Canonical Monte Carlo simulations show that these variables have a profound influence on gas-liquid and freezing transitions in confinement.

**CAPILLARY CONDENSATION AND FREEZING OF SIMPLE
FLUIDS CONFINED IN CYLINDRICAL NANOPORES**

by

FRANCISCO RODOLFO HUNG

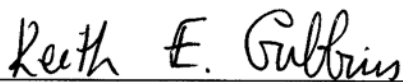
A dissertation submitted to the Graduate Faculty of
North Carolina State University
in partial fulfillment of the requirements for the
Degree of Doctor of Philosophy

CHEMICAL AND BIOMOLECULAR ENGINEERING

Raleigh

2005

APPROVED BY:



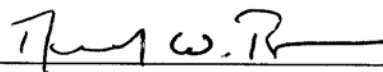
Keith E. Gubbins, Chair



Carol K. Hall



Orlin D. Velev



Donald W. Brenner

*A Desirée y Arianna,
a mi familia, especialmente mis padres,
a Dios y la Virgen Milagrosa.
Gracias por bendecir mi existencia.*

*To Desirée and Arianna,
to my family, especially my parents,
to God and Virgin Mary.
Thanks for blessing my life.*

... and to Murphy.

Biography

Francisco R. Hung was born on November 5, 1973 in Caracas, Venezuela, to his parents Yun Wun Hung and Lai Ngor de Hung, both originally from China. He was raised in Caracas, along with his older brothers Daniel and Julio. Francisco attended Universidad Simón Bolívar in Caracas to study Chemical Engineering, earning a scholarship from Pequiven (the Venezuelan petrochemical industry) in 1991. Francisco graduated *cum laude* and first of his class in 1996. He then started his graduate studies in Chemical Engineering at Universidad Simón Bolívar, and at the same time, he was hired as a Lecturer by the Department of Thermodynamics and Transport Phenomena. He was in charge of teaching a number of undergraduate courses, such as Thermodynamics and Transport Phenomena laboratories, while taking graduate courses and doing his research project. Under the supervision of Professor Erich A. Müller, Francisco studied adsorption of water vapor and methane mixtures on activated carbons using molecular simulation techniques. He obtained his M.S. in Chemical Engineering (honor mention) from Universidad Simón Bolívar in 1999, and became an Assistant Professor. Francisco started his Ph.D. studies in the Department of Chemical Engineering at North Carolina State University in 2000. He joined Prof. Keith E. Gubbins' research group, where he carried out the work presented here. After defending his dissertation, Francisco will join Prof. Juan J. de Pablo's research group at the University of Wisconsin-Madison, to work as a postdoctoral research associate.

Twelve days before coming to Raleigh, on July 29, 2000, Francisco married his sweetheart, Minerva Desirée Vignola, who was then a journalist working in a radio station in Caracas. They are the proud and happy (and sometimes exhausted) parents of Arianna, a fully-energetic and always-smiling little girl who was born in Cary, North Carolina, on May 1, 2003.

Acknowledgments

I have been blessed to have Keith E. Gubbins as my advisor. He always provided the right level of guidance in my research, giving me the freedom to pursue my own ideas. I am deeply grateful to him for his invaluable career advice, as well as for sharing with me his vision of science, people, world and life in general. Keith, thanks for giving me this opportunity, and for always encouraging me to aim high; I will always regard you as a mentor and, most important, as a friend.

I want to thank all the outstanding scientists that I had the privilege to work with. I am especially in debt with my main collaborators, Benoit Coasne, Erik Santiso and Flor Siperstein: thanks for all the helpful discussions, your advice and, most important, for your friendship. I am also thankful to Malgorzata Sliwinska-Bartkowiak, Grazyna Dudziak and Monika Jazdzewska, for always being willing to collaborate and for performing the experiments of freezing within carbon nanotubes. I also extend my gratitude to all the outstanding scientists I had the opportunity to interact with: Supriyo Bhattacharya, Henry Bock, John Brennan, Naresh Chennamsetty, Coray Colina, Surendra Jain, Milen Kostov, Martin Lisal, Joshua Moore, Roland Pellenq, Jorge Pikunic, Ravi Radhakrishnan, Erik Santiso, Lauriane Scanu, Martin Schoen and Heath Turner (also to any others I am sure I am forgetting to mention here). I am also grateful to my committee members, as well as to Jan Genzer, John van Zanten and my former advisor, Erich A. Müller, for all their advice and help. Also, I would like to give special thanks to Sandra Bailey, Sheila Hayes and June McKoy, for always being there to help me with so many things.

This work was supported by grants from the National Science Foundation (CTS-0211792) and the Committee of Scientific Research of Poland (KBN 2P03B 014 24). International cooperation was possible thanks to a NATO Collaborative Linkage Grant (PST.CLG.978802). This research used supercomputing resources from the San Diego Supercomputer Center (SDSC) and the National Center for Supercomputing Applications (NCSA), under NSF grants NRAC MCA93SO11, and MRAC CHE050047S. We also used supercomputing resources from the National Energy Research Scientific Computing Center (NERSC), under DOE grant DE-FGO2-98ER14847; and from the High Performance Computing centers at North Carolina State University and University of North Carolina at Chapel Hill.

Finally, I want to thank all our friends who made our stay in Raleigh such a wonderful experience, especially to the Gubbins' group actual and former members, as well as the Bock, Castaño-Colina, Hohl, Prado-Ramos, Santiso, Santos and Scanu families: your friendship has been a blessing for us. I am also very grateful to my family. My parents, my brothers and sisters, and especially my wife Desirée and my daughter Arianna, gave me all the support, patience and love I needed, and much more. Thanks for being such an important part of my life.

Table of Contents

List of Tables	ix
List of Figures	x
Chapter 1. Introduction	1
1.1. Previous Studies of Freezing/Melting in Confinement	3
1.2. Overview of our Work	8
1.3. References	12
Chapter 2. Freezing/Melting Behavior of CCl₄ within Multi-Walled Carbon Nanotubes	16
2.1. Experimental Section	17
2.2. Simulation Details	19
2.2.1. Models	19
2.2.2. Methods	20
2.2.3. Structure analysis	21
2.2.4. Free energy calculations	26
2.3. Experimental Results	30
2.4. Simulation Results	33
2.4.1. Grand canonical Monte Carlo simulations	33
2.4.2. Free energy calculations	39
2.5. Concluding Remarks	45
2.6. References	46

Chapter 3. Effect of Confinement on Freezing of CCl₄ within Multi-Walled Carbon Nanotubes	49
3.1. Experimental Section	50
3.2. Simulation Details	50
3.3. Experimental Results	53
3.3.1. Comparison with experimental results, MWCNT with $D = 5.0$ nm	55
3.4. Simulation Results	56
3.4.1. Comparison with simulation results, MWCNT with $D^* = 9.7$ ($D = 5$ nm)	63
3.4.2. Comparison with experimental results	65
3.5. Conclusions	66
3.6. References	69
Chapter 4. Capillary Condensation of Krypton within Realistic Models of Templated Mesoporous Silica Materials	71
4.1. Simulation Details	73
4.1.1. Preparation of atomistic silica mesopore models	73
4.1.2. Kr adsorption	80
4.2. Results	82
4.3. Concluding Remarks	88
4.4. References	90

Chapter 5. Freezing of Krypton within Mesoporous Silica Materials: Effect of Pore Morphology and Surface Roughness	93
5.1. Simulation Details	97
5.1.1. Models and methods	97
5.1.2. Structure analysis	100
5.2. Results	102
5.3. Concluding Remarks and Future Work	113
5.4. References	114
Chapter 6. Conclusions and Future Directions	118
References	124

List of Tables

2.1.	Values of the 3D bond orientational order parameters for some common 3D crystals. Taken from Ref. 22.	25
2.2.	Thermodynamic transition temperatures and phases involved, for LJ CCl ₄ confined within a MWCNT with $D^* = 9.7$, as determined from free energy calculations. See text for descriptions of the different phases.	44
3.1.	Temperature range of each structure for LJ CCl ₄ confined within MWCNT with $D^* = 7.5$ and 5.5 , as determined from PT-GCMC simulations. See text for descriptions of the different structures.	62
4.1.	Potential parameters used for the canonical Monte Carlo simulation of the surface relaxation of the MCM-41 silica pore. Oxygen atoms forming an OH bond at the pore surface and oxygen atoms in bulk region have the same properties in this model. All interactions were determined using two-body potentials of the BKS type [21], except the interaction between H and O atoms forming a hydroxyl group, which was modeled using a Morse potential [24,25]. Note that the following interactions are purely coulombic: Si/Si, Si/H and H/H. This set of parameters is taken from Refs. [21] and [24].	76
4.2.	PN-TraZ potential parameters for Kr adsorption in silica pores. Parameters are in atomic units: $E_h = 3.1578 \cdot 10^5$ K, $a_0 = 0.529177$ Å. Taken from Ref. [19]	81

List of Figures

- 2.1. Schematic view of the experimental setup used in dielectric relaxation spectroscopy (DRS). A suspension of CCl_4 -filled MWCNT in bulk CCl_4 is introduced between the parallel plates of a capacitor (empty capacitance $C_0 = 4.2$ pF). Phase changes (such as melting) in the system are determined by monitoring the capacitance C of the system as a function of temperature T , upon an electric field with voltage V oscillating at a frequency ω . 18
- 2.2. Density profile along the radial direction, and snapshots of typical configurations of LJ CCl_4 confined within structureless MWCNT, at different temperatures for $D^* = 9.7$ ($D = 5.0$ nm). The carbon walls are not shown in the snapshots for clarity. Front views of the same snapshots depicting the adsorbed molecules with a reduced diameter are also provided, to help visualize the formation of concentric layers as the temperature decreases. 22
- 2.3. Capacitance C as a function of temperature T for CCl_4 adsorbed on open-tip MWCNT, with average internal and external pore diameters of 5.0 nm and 10 nm. The measurements were performed at frequencies ω equal to 30 kHz (circles), 100 kHz (squares) and 600 kHz (triangles). The error bars for the capacitance and temperature are equal to ± 0.01 pF and ± 0.1 K, respectively. 32
- 2.4. Amount adsorbed as a function of temperature for LJ CCl_4 confined in a model structureless, multi-walled carbon nanotube with $D^* = 9.7$ ($D = 5.0$ nm), from PT-GCMC simulations. The black filled symbol represent results from a GCMC simulation performed at $T = 177$ K. The thick dashed line represents the bulk solid-fluid phase transition temperature. 34
- 2.5. Average values of the bond order parameters measured for LJ CCl_4 confined in a structureless MWCNT with $D^* = 9.7$ ($D = 5.0$ nm), as a function of temperature. $\Phi_{6,j}$ was measured for the contact, second and third layers, and $Q_{6,inner}$ is reported for the adsorbate in the center of the pore (fourth and innermost layers). The black filled symbols represent results from a GCMC simulation performed at $T = 177$ K. The thick dotted line at 251 K represents the bulk 35

melting point of LJ CCl₄. The three thin dotted lines at 205, 234 and 259 K represent the experimental transition temperatures of CCl₄ within MWCNT with $D = 5.0$ nm, from dielectric relaxation spectroscopy measurements.

- 2.6. 2D positional and bond orientational correlation functions, $g_j(r)$ and $G_{6,j}(r)$, for the first three molecular layers of adsorbate, and 3D positional correlation function corrected by excluded volume effects, $g(R)$, for the adsorbate in the center of the pore. r is the in-layer distance, and R represents the 3D distance. Five different confined phases A, B, C, D and E (see text for descriptions) can be observed for LJ CCl₄ within a structureless MWCNT of $D^* = 9.7$ at different temperatures. For clarity, the $g_j(r)$ functions corresponding to the contact, second and third layers have been shifted by +6, +4 and +2, respectively. In a similar way, the $G_{6,j}(r)$ functions corresponding to the contact and second layers have been displaced by +0.8 and +0.4, respectively. 38
- 2.7. First order distribution functions of the probability P for LJ CCl₄ within a structureless MWCNT of $D^* = 9.7$ at $T = 252$ K. The distribution function $P^{(1)}(\Phi_{6,contact})$ was obtained by numerically integrating P with respect to all the order parameters except $\Phi_{6,contact}$; the same principle applies to $P^{(1)}(\Phi_{6,second})$, $P^{(1)}(\Phi_{6,third})$, and $P^{(1)}(Q_{6,inner})$. 40
- 2.8. Grand free energy Ω of the different phases as a function of temperature T , for LJ CCl₄ confined within a structureless MWCNT of $D^* = 9.7$. To facilitate visualization, the difference of grand free energy of each phase with respect to phase A is presented, and three plots are provided for temperature ranges close to the transition points. 42
- 2.9. 3D positional correlation function $g(R)$, corrected by excluded volume effects, for the all molecules of LJ CCl₄ confined within structureless MWCNT with $D^* = 9.7$, at different temperatures. 45
- 3.1. Density profile along the radial direction, and snapshots of typical configurations of LJ CCl₄ confined within structureless MWCNT, at different temperatures for $D^* = 7.5$ ($D = 3.9$ nm). The carbon walls are not shown in the snapshots for clarity. Front views of the same snapshots depicting the adsorbed molecules with a reduced diameter 52

are also provided, to help visualize the formation of concentric layers as the temperature decreases.

- | | | |
|------|---|----|
| 3.2. | Capacitance C as a function of temperature T for CCl_4 in open-tip MWCNT with an average internal pore diameter of 4.0 nm. The measurements were performed at frequencies ω equal to 100 kHz (circles) and 600 kHz (triangles). The error bars for the capacitance and temperature are equal to ± 0.01 pF and ± 0.1 K, respectively. | 54 |
| 3.3. | Capacitance C as a function of temperature T for CCl_4 in open-tip MWCNT with an average internal pore diameter of 2.8 nm. The measurements were performed at frequencies ω equal to 600 kHz. The error bars for the capacitance and temperature are equal to ± 0.01 pF and ± 0.1 K, respectively. | 55 |
| 3.4. | Amount adsorbed as a function of temperature for LJ CCl_4 confined within a structureless MWCNT of (a) $D^* = 7.5$ ($D = 3.9$ nm), and (b) $D^* = 5.5$ ($D = 2.8$ nm). The thick dotted line represents the bulk melting point of LJ CCl_4 for all cases. | 57 |
| 3.5. | Average values of the 2D bond order parameters $\Phi_{6,j}$ (open symbols, left ordinate axis), and reduced local density for the innermost layer ρ_{inner}^* (black filled circles, right ordinate axis), as a function of temperature, for (a) $D^* = 7.5$ ($D = 3.9$ nm), and (b) $D^* = 5.5$ ($D = 2.8$ nm). The thick dotted line represents the bulk melting point of LJ CCl_4 for all cases. | 59 |
| 3.6. | 3D positional correlation function $g(R)$, corrected by excluded volume effects, for the all molecules of LJ CCl_4 confined within structureless MWCNT: (a) $D^* = 7.5$, and (b) $D^* = 5.5$, at different temperatures. | 63 |
| 4.1. | Scheme of the procedure used to generate atomistic silica pore models used in this study. Front views and/or cross sections of the three pore models are also shown. Oxygen, silicon and hydrogen atoms are depicted in white, tan and black, respectively. For model C, we have represented two simulation boxes aligned in the axial direction z . | 77 |
| 4.2. | Left: pore size distribution R for model A, estimated from the distance between hydrogen atoms at the pore surface and the pore | 78 |

center. Right: average pore size $R(z)$ as a function of the position on the pore axis z for model A. $R(z)$ was estimated from the average distance to the pore center of hydrogen atoms located at a position z . In both figures, the black and red lines corresponds to samples 1 and 2 (see text).

- 4.3. Small angle neutron scattering spectra for pore model A (red line) and pore model B (black line). The Bragg peaks of cubic cristobalite are in very good agreement with the experimental x-ray peaks: 1.52, 2.49, 2.90, 3.03, 3.83 and 4.55 \AA^{-1} . The two straight lines correspond to an algebraic decay over the range 0.05-0.55 \AA^{-1} with the exponent 3.6 for model A and 4.0 for model B (see text). 79
- 4.4. Adsorption-desorption isotherms for Kr at (a) $T = 100$ K, and (b) $T = 87$ K. Results for pore models A, B and C are depicted by triangles, diamonds and circles, respectively; squares represent experimental results on SBA-15 with a similar mean pore diameter (6.4 nm) [37]. Open and closed symbols represent adsorption and desorption, respectively. 83
- 4.5. Isothermic heat of adsorption q_{st} as a function of coverage fraction N/N_0 , for Kr adsorption on atomistic silica mesopores at 100 K: (a) total q_{st} , and (b) adsorbate-wall (filled symbols) and adsorbate-adsorbate (open symbols) contributions to q_{st} . Symbols as in Figure 4.4. 85
- 4.6. Local density profile $\rho(r, z)$, and front views or cross sections of representative simulation snapshots of the confined phase inside (a) pore model A, (b) pore model B, and (c) pore model C, for different values of P/P_0 at $T = 100$ K. Two simulation boxes aligned in the axial direction z are represented in the snapshots for pore model C, to help visualization of the confined phase features. 87
- 4.7. 3D positional pair correlation function $g(R)$ for Kr at $T = 87$ K and $P/P_0 = 1$. 88
- 5.1. Scheme of the procedure used to generate atomistic silica pore models used in this study. Front views and/or cross sections of the three pore models are also shown. Oxygen, silicon and hydrogen atoms are depicted in red, tan and black, respectively. For model C, we have represented two simulation boxes aligned in the axial direction z . 99

- 5.2. Kr within a siliceous regular cylindrical pore with $D = 6.4$ nm (pore model B) at $T = 79$ K. (a) Cross section of a representative simulation snapshot. Crystal-like and noncrystal-like Kr molecules are depicted in gray and purple, respectively; oxygen, silicon and hydrogen atoms in the pore walls are represented in red, tan and black, respectively. (b) Average number of connections per particle, as a function of reduced radial and axial coordinates r^* and z^* . A Kr molecule is considered crystal-like if its number of connections is equal or larger than seven. (c) 3D positional pair correlation functions $g(R)$ for all Kr molecules inside the pore, and for Kr molecules with $r^* \leq 4$. For clarity, the latter function has been shifted by +1. 104
- 5.3. Kr within pore model B at $T = 70$ K. (a) Cross section of a representative simulation snapshot. (b) Average number of connections per particle, as a function of reduced radial and axial coordinates r^* and z^* . (c) 3D positional pair correlation functions $g(R)$ for all Kr molecules inside the pore, and for Kr molecules with $r^* \leq 4$. Details are the same as in Figure 5.2. 105
- 5.4. Kr within a siliceous cylindrical pore of diameter 8.2 nm with a constriction of diameter 4.1 nm (pore model C) at $T = 79$ K. (a) Cross section of a representative simulation snapshot. Crystal-like and noncrystal-like Kr molecules are depicted in gray and purple, respectively; oxygen, silicon and hydrogen atoms in the pore walls are represented in red, tan and black, respectively. We have represented two simulation boxes aligned in the axial direction z to facilitate visualization. (b) Average number of connections per particle, as a function of reduced radial and axial coordinates r^* and z^* . A Kr molecule is considered crystal-like if its number of connections is equal or larger than seven. (c) 3D positional pair correlation functions $g(R)$ for all Kr molecules inside the pore, and for Kr molecules with $r^* \leq 4$. For clarity, the latter function has been shifted by +1. 107
- 5.5. Kr within pore model C at $T = 75$ K. (a) Cross section of a representative simulation snapshot. (b) Average number of connections per particle, as a function of reduced radial and axial coordinates r^* and z^* . (c) 3D positional pair correlation functions $g(R)$ for all Kr molecules inside the pore, and for Kr molecules with $r^* \leq 4$. Details are the same as in Figure 5.4. 108

- 5.6. Kr within pore model C at $T = 67$ K. (a) Cross section of a representative simulation snapshot. (b) Average number of connections per particle, as a function of reduced radial and axial coordinates r^* and z^* . (c) 3D positional pair correlation functions $g(R)$ for all Kr molecules inside the pore, and for Kr molecules with $r^* \leq 4$. Details are the same as in Figure 5.4. 109
- 5.7. Kr within a siliceous cylindrical pore with average diameter of 6.4 nm (pore model A) at $T = 79$ K. (a) Cross section of a representative simulation snapshot. Crystal-like and noncrystal-like Kr molecules are depicted in gray and purple, respectively; oxygen, silicon and hydrogen atoms in the pore walls are represented in red, tan and black, respectively. (b) Average number of connections per particle, as a function of reduced radial and axial coordinates r^* and z^* . A Kr molecule is considered crystal-like if its number of connections is equal or larger than seven. (c) 3D positional pair correlation functions $g(R)$ for all Kr molecules inside the pore, and for Kr molecules with $r^* \leq 4$. For clarity, the latter function has been shifted by +1. 111
- 5.8. Kr within pore model A at $T = 70$ K. (a) Cross section of a representative simulation snapshot. (b) Average number of connections per particle, as a function of reduced radial and axial coordinates r^* and z^* . (c) 3D positional pair correlation functions $g(R)$ for all Kr molecules inside the pore, and for Kr molecules with $r^* \leq 4$. Details are the same as in Figure 5.7. 112

Chapter 1

Introduction

The aim of this research project is to use molecular simulation techniques to understand the phase behavior of pure simple fluids, when they are confined inside materials with cylindrical, non-interconnected nanopores, e.g. carbon nanotubes and templated mesoporous silica materials (MCM-41). A wide range of physical behavior can arise when molecules are confined inside pores with dimensions on the order of a few molecular diameters. New surface-driven phases not observed in bulk systems can appear, and phase transitions (e.g. gas-liquid, freezing) can be shifted to different conditions of temperature, composition, etc. A fundamental understanding of these phenomena is necessary for many industrial applications: porous materials are widely used in the chemical, oil and gas, food and pharmaceutical industries for pollution control, mixture separation and catalysis. In addition, porous materials with very regular morphology are finding applications in nanofabrication and nanotechnology. From a fundamental viewpoint, studies of these phenomena can provide important insights on the effect of surface forces, confinement and reduced dimensionality on the phase behavior of host molecules.

There are a number of experimental techniques that can be used to measure different properties of the confined phases. However, it is difficult to obtain a complete picture of these phenomena from experiment alone. Metastable states are more likely in confined systems than in bulk phases; for example, for freezing in confinement it is difficult to know if the experimental system is in thermodynamic equilibrium, and in some particular cases [1] equilibrium may not be reached in a reasonable time. Scattering techniques commonly used to determine the nature of bulk phases are more difficult to apply to confined phases. In addition, complex

pore geometries (irregular pore shapes, interconnected pores, etc.) and poor characterization of porous materials can make problematic the interpretation of experimental results. These difficulties are not present or can be overcome in simulations; however other problems arise, such as inaccuracies in the intermolecular potentials and limitations in time and length scales accessible to current supercomputers. Since the difficulties in simulations are not present in experiments and viceversa, both studies can be of complementary nature; a comparison of results from both approaches can help in their analysis, and can lead to important new insights in this area. Therefore, whenever possible, the simulation results from this research project are compared with experimental measurements.

Out of the many possible phase transitions that can be observed in confined systems [1], we concentrate mainly on freezing/melting transitions in pores that are completely filled with adsorbate molecules. However, in one of our studies we developed atomistic models of MCM-41 type materials that include pore morphological defects and surface roughness. Therefore, we have included results for gas-liquid (capillary condensation) equilibria, since a comparison between simulation and experimental results for gas adsorption provide an assessment of our pore models as compared to the real material. The rest of this chapter is organized as follows. In Section 1.1 we present a summary of previous experimental and simulation studies on freezing and melting of molecules confined in nanopores. Even though we are mainly interested in studies using materials with cylindrical, non-interconnected nanopores, e.g. carbon nanotubes and templated mesoporous silica materials (MCM-41), we also summarize some important results from studies on cylindrical, interconnected pores (controlled pore glasses, Vycor, SBA-15, etc.), as well as on pores with slit-like geometry (activated carbon fiber, the mica plates of the surface force apparatus). Since a couple of comprehensive

review papers about this topic have been published recently [1,2], we make some emphasis in summarizing very recent simulation studies not included in such reviews. Finally, an overview of the work presented in the next chapters is presented in Section 1.2.

1.1. Previous Studies of Freezing/Melting in Confinement

A large amount of experimental evidence [1,2] clearly indicates that the phase diagram of a substance can be significantly altered when confined within a porous material. Most of the early experimental studies [1,2], as well as recent works on freezing in confinement have been carried out using different siliceous materials (mainly controlled pore glass, Vycor, MCM-41 and SBA-15) and a wide variety of adsorbates, such as water [3-7], methyl chloride [8], methanol [9], nitrobenzene [10,11], aniline [12], carbon tetrachloride [10], nitrogen [13,14], carbon monoxide [13-15], krypton [13,16], argon [15,17-19], carbon dioxide [20], oxygen [21,22], benzene [4,23-25], cyclohexane [4,23], and acetonitrile [26], among others. Significant hysteresis effects between freezing and melting were observed, as well as evidence of different freezing behaviors for the adsorbate in the central regions of the pore and the contact layer (the adsorbed molecules adjacent to the pore wall), suggesting the presence of inhomogeneous confined phases (see, e.g. [1,2,6,14,18,24]). In most cases, the structure of the confined solid was found to deviate from the bulk crystal phase, and the morphology of the confined solid was strongly dependent on pore size. For instance, the confined material was found to crystallize only partially below certain pore sizes, and for even smaller pores amorphous solids were always observed. All those studies indicate that the freezing temperature inside the weakly attractive silica pores is lower than that for the bulk. For pore sizes larger than 5 nm, the depression in the confined freezing

temperature becomes larger as the pore size decreased, in agreement with the Gibbs-Thomson equation [1,2]. This macroscopic equation was found to break down for systems confined in pores of small sizes, up to a few adsorbate molecular diameters [1,2], where the depression in the freezing temperature inside the pore becomes non-monotonically larger with reduction of the pore size.

In contrast, some experimental studies have shown that an elevation in the freezing point is observed for systems where the adsorbate-wall attractive interactions are strong compared to the adsorbate-adsorbate interactions, and there is matching between the morphologies of the porous media and the confined solid phase. For instance, Klein and Kumacheva [27] studied cyclohexane and octamethylcyclotetrasiloxane (OMCTS) confined between parallel mica plates in a surface force apparatus (SFA). Upon reduction of the separation between the surfaces, it was observed that the confined film could sustain a finite shear stress for macroscopic times, and the film rigidity (quantified by an “effective viscosity”) increased. This was interpreted as a liquid to solid phase transition occurring at temperatures well above the bulk freezing point, which was believed to be due to strong attraction between the confined fluid molecules and potassium in the mica surface. More recently, and after the systematic molecular simulation studies of Miyahara and Gubbins [28], and Maddox and Gubbins [29], a number of experiments using activated carbon fibers (ACF) have reported that the freezing temperature in confinement may be lower (water [30-32], octanol [33] and undecanol [33]) or higher (methanol [32], carbon tetrachloride [34], benzene [35], aniline [36], OMCTS [37] and cyclohexane [37]) than the bulk value; in some cases (nitrobenzene [38]), no appreciable change in the freezing temperature was observed.

Miyahara and Gubbins [28] performed systematic Grand Canonical Monte Carlo (GCMC) simulations of freezing and melting of Lennard-Jones (LJ) methane confined within slit pores. When the adsorbate-wall attractive interactions were weaker compared to the adsorbate-adsorbate interactions, the freezing temperature in confinement was significantly lower than in the bulk, as reported in most of the experiments for silica pores. In contrast, a large increase in the freezing temperature was found for strongly attractive materials, such as porous carbons. No appreciable change in the freezing temperature was observed when the adsorbate-wall and adsorbate-adsorbate interactions were similar. Moreover, the contact layers were found to freeze at temperatures higher or lower than the rest of the adsorbed fluid for the cases of strongly or weakly attractive walls, respectively. Those findings were further confirmed in simulation studies where the free energy of the confined phases were calculated, using a thermodynamic integration method [39] and a Landau-Ginzburg approach [40,41]. By combining the latter approach with corresponding states theory, Radhakrishnan *et al.* [38,41] obtained phase diagrams for a wide range of adsorbates and slit pore walls, in terms of the reduced pore width H^* and a parameter α measuring the ratio of the fluid-wall to the fluid-fluid interaction:

$$H^* = \frac{H}{\sigma_{ff}} \quad (1.1)$$

$$\alpha = \frac{\rho_w \varepsilon_{fw} \sigma_{fw}^2 \Delta}{\varepsilon_{ff}} \quad (1.2)$$

where H is the pore width, σ_{ff} is the size parameter of the adsorbate, ρ_w is the atom density of the pore wall, ε_{fw} and ε_{ff} are the interaction energy parameters fluid-wall

and fluid-fluid, respectively, σ_{fw} is the fluid-wall size parameter and Δ is the spacing between the atomic layers that conform the pore wall. Recent simulations [41,42] and experiments [42] for CCl_4 within ACF have suggested the existence of hexatic phases in temperature ranges between those for the hexagonal crystal and liquid phases. Such hexatic phases are quasi-2D systems with quasi-long-range six-fold bond orientational order and positional disorder. The liquid-hexatic and hexatic-crystal transitions for the molecular layers of adsorbate were found [42] to be consistent with the Kosterlitz-Thouless-Halperin-Nelson-Young (KTHNY) theory for 2-D melting [43-45]. Recent simulation studies [46-49] have investigated solid-solid transitions for LJ fluids within slit pores. Strong layering was observed in the systems studied, and transformations between square and triangular lattices were observed in the layers of adsorbate upon changes in the pore width H . These transitions produced variations in density and in the solvation force [46-49].

For pores of cylindrical geometries, Maddox and Gubbins [29] investigated freezing of confined LJ methane using a combined GCMC and Molecular Dynamics (MD) simulation approach. Freezing temperatures lower than the bulk freezing point were obtained inside structureless weakly attractive pores, in analogy to the findings of Miyahara and Gubbins [28] for slit pores. In contrast, for a structureless strongly attractive pore Maddox and Gubbins [29] found that the fluid near the pore walls experienced an increase in the freezing point, but in the center the freezing temperature was depressed due to geometrical constraints. The freezing temperatures in cylindrical pores were found to be lower than those obtained within slit pores of similar characteristics, due to the additional degree of confinement. Kanda *et al.* [50] also studied freezing of LJ methane within structureless model carbon cylindrical pores by means of GCMC simulations, finding a non-monotonic dependence of freezing point against pore diameter. This

was interpreted as a result of the competition between geometric constraints and fluid-wall interaction effects. Sliwinska-Bartkowiak *et al.* [11] reported both experimental and simulation results for freezing of nitrobenzene and CCl_4 in porous glasses and MCM-41; a structureless cylindrical pore was used in the simulations to represent the MCM-41 silica material. It was found that the confined fluid is able to crystallize when the average pore diameter D is greater than $20\sigma_{ff}$, where σ_{ff} is the size parameter of the adsorbate. For smaller pore diameters, the confined fluid solidifies forming either frustrated crystals or amorphous solids. Hoffmann and Nielaba [51] performed classical and path integral Monte Carlo simulations in the canonical (NVT) ensemble to study freezing of argon and neon within structureless cylindrical pores. For strongly attractive pores, the adsorbate was found to freeze in concentric layers, with the contact layer freezing at temperatures higher than the rest of the system. Structures with local fcc or hcp order were observed for pores with weak fluid-wall interactions.

The simulation studies mentioned in the previous paragraph were performed using smooth, structureless cylindrical pores. Very recently, Arcidiacono *et al.* [52] performed MD simulations to investigate the solidification of gold nanoparticles within atomistic models of carbon nanotubes of different diameters. They found that the gold nanoparticles exhibit a higher solidification temperature than the corresponding isolated clusters, due to the presence of the strongly attractive carbon nanotube walls. In a series of recent studies, Nishio *et al.* [53-55] performed MD simulations of freezing of LJ argon within a cylindrical pore representing a silica material. Such a nanopore was carved out of a cubic box containing oxygen atoms; the interactions of Ar with Si were ignored. Both ends of the cylindrical pore were in contact with gas reservoirs, a simulation scheme similar to that proposed by Sarkisov and Monson [56]. In these studies [53-55], it

was found that Ar crystallized for pores with diameter $D \geq 15\sigma_{ff}$ when the cooling rate is lower than a certain critical value. In contrast, for $D = 10\sigma_{ff}$ crystallization was not observed even at very low cooling rates, in agreement with the GCMC results of Sliwinska *et al.* [11] for structureless silica pores. Solid, amorphous Ar within a pore of $D = 10\sigma_{ff}$ exhibited a local icosahedral symmetry [53-55].

1.2. Overview of our Work

As stated before, the main objective of this work is to use molecular simulation techniques to understand the phase behavior (mainly freezing/melting transitions) of simple fluids confined inside porous materials with cylindrical, non-interconnected nanopores. In that sense, we have performed two independent, but directly related studies: (1) freezing of carbon tetrachloride within multi-walled carbon nanotubes (MWCNT), and (2) capillary condensation and freezing of krypton within templated mesoporous silica materials (MCM-41).

Our combined experimental and simulation studies of freezing of CCl_4 confined within multi-walled carbon nanotubes are presented in Chapters 2 and 3. CCl_4 was selected since it is a substance convenient to study from both simulation and experimental points of view. MWCNT were selected because they are representative of materials with cylindrical pores and strongly attractive walls, where the wall-adsorbate interactions are stronger than the adsorbate-adsorbate interactions. As mentioned in Section 1.1, previous experimental studies of freezing in confinement have been carried out using weakly attractive siliceous materials with cylindrical pores (controlled pore glasses, Vycor, MCM-41, SBA-15), or materials with strongly attractive pores of slit-like geometry (the mica surfaces of the surface force apparatus, activated carbon fibers). In Chapter 2 we

report results for freezing and melting of CCl_4 within multi-walled carbon nanotubes with an average internal diameter of 5.0 nm. This study was aimed at obtaining a rigorous picture of the solid-fluid phase behavior for such a system. The experimental melting points were determined from dielectric relaxation spectroscopy measurements performed by our experimental collaborators in Adam Mickiewicz University in Poznan, Poland. From the molecular simulation point of view, we have extended the parallel tempering grand canonical Monte Carlo methodology [57] to investigate the freezing behavior of the confined adsorbate. We also determined the free energy of the different phases present in the system, in order to rigorously determine the structure and thermodynamic stability of the confined phases, as well as the temperatures and the order of the phase transitions. These results have been published elsewhere [58-60]. To study the effect of confinement on freezing of confined CCl_4 , we have considered multi-walled carbon nanotubes with two additional pore sizes. Results from this combined experimental and simulation investigation are presented in Chapter 3 and published elsewhere [60,61]. A comparison between our results from the parallel tempering scheme and the free energy calculations shows that the former methodology is capable of giving true equilibrium results for confined systems [60]. Parallel tempering techniques have also been used in a different study to investigate the freezing behavior of binary Lennard-Jones mixtures, having either a simple solid solution or an hylotropic [62] solid-liquid phase diagram, when they are confined within slit pores [63-66].

Most of the simulation studies of freezing in confinement reported so far have considered simple, structureless pore geometries (slit, cylindrical). Some freezing studies considering atomistic pore models have been reported very recently [52-55], but still pores with regular cylindrical shape were used. Real materials can exhibit complex pore geometries: some of them have non-connected pores, such as

carbon nanotubes and templated mesoporous materials, but others present a highly networked porous structure, such as activated carbons and silica glasses. Realistic models of some porous materials have been developed recently using simulation protocols; those include silica glasses [67,68], porous carbons [69-71], and templated mesoporous silica materials (MCM-41) [72,73]. Since the latter materials present negligible pore networking effects [74,75], we have selected those for simplicity for our studies. In addition, MCM-41 is representative of porous materials with weakly attractive walls for most non-polar adsorbates. Therefore, a comparison with the results presented in Chapters 2 and 3 will allow us to address the effect of fluid-walls interactions on freezing in confinement.

In most simulation and theoretical studies, MCM-41 materials have been modeled as pores with a regular cylindrical geometry. Recent simulation studies of gas adsorption [76-79] and freezing [53-55] have used different atomistic models of these materials. It is unclear whether those models are realistic representations of MCM-41, due to the lack of conclusive experimental data regarding its pore surface roughness and morphology. Some experimental results [80,81] attribute some surface roughness to the pore walls, whereas others [82,83] suggest a smooth surface at molecular scales (3-7 Å) with roughness and other morphological defects (constrictions, tortuosity) at larger length scales (20-50 Å). One possible approach to model porous solids is to mimic the synthesis process of the real material using simulations, a strategy used in the past [67] to develop realistic models for silica glasses. Recently, Siperstein and Gubbins [72,73] used lattice Monte Carlo simulations to study the behavior of surfactant-inorganic oxide-solvent systems and mimic the synthesis of templated mesoporous silica materials. Low values of the surfactant/inorganic oxide concentration ratio led to formation of hexagonally ordered porous structures that resemble that of the MCM-41 material. Pores with an important degree of surface roughness and structural

defects were obtained from this mesoscale simulation protocol. In Chapter 4 we report the preparation of realistic, atomistic silica mesopores that keep the morphological features of the MCM-41 lattice model developed by Siperstein and Gubbins [72,73]. In doing this “downscaling” process, atomic details are included in our model, more accurate potentials are used for the adsorbate-wall interactions, and the effect of structural defects on the adsorbate phase behavior can be assessed. We performed Grand Canonical Monte Carlo (GCMC) simulations of krypton adsorption at 100 K and 87 K, for which we report adsorption isotherms and isosteric heats of adsorption. Kr adsorption at low temperatures (77, 87 K) has been used in the past for characterization of porous materials with very low surface areas and volumes [84,85]. We discuss the effect of pore shape and morphology, by comparing adsorption results obtained in this pore model with those obtained in two additional atomistic silica pore models with similar diameters, a regular cylindrical nanopore and a cylindrical pore with constrictions. In addition, an assessment of our pore models as compared to the real material is provided, by comparing simulation and experimental results for small angle neutron scattering (SANS) spectra and gas adsorption. Results presented in this chapter have been reported elsewhere [86-88]. In a separate study [89], we have used a similar technique to generate atomistic models for other templated mesoporous silica materials such as SBA-15, based on mesoscale models from lattice Monte Carlo simulations.

In Chapter 5 we present a preliminary account of our GCMC results for freezing of Kr within the same silica mesopore models described before, with an average pore diameter of 6.4 nm. We discuss the effect of pore surface roughness and morphological defects on the freezing temperatures and the structure of the confined phases, and we include a comparison with experimental results for an equivalent system. Full details of this study will be published elsewhere [90].

Finally, our concluding remarks are presented in Chapter 6, together with our suggestions for future extensions of this work.

1.3. References

- [1] L. D. Gelb, K. E. Gubbins, R. Radhakrishnan and M. Sliwinska-Bartkowiak, *Rep. Prog. Phys.* **62**, 1573 (1999).
- [2] H. K. Christenson, *J. Phys.: Condens. Matter* **13**, R95 (2001).
- [3] K. Morishige and K. Kawano, *J. Chem. Phys.* **110**, 4867 (1999).
- [4] D. Morineau, G. Dosseh, C. Alba-Simionesco, and P. Llewellyn, *Philos. Mag. B* **79**, 1847 (1999)
- [5] P. Smirnov, T. Yamaguchi, S. Kittaka, S. Takahara, and Y. Kuroda, *J. Phys. Chem. B* **104**, 5498 (2000).
- [6] A. Schreiber, I. Ketelsen, and G. H. Findenegg, *Phys. Chem. Chem. Phys.* **3**, 1185 (2001).
- [7] K. Morishige and H. Iwasaki, *Langmuir* **19**, 2808 (2003).
- [8] K. Morishige and K. Kawano, *J. Phys. Chem. B* **103**, 7906 (1999).
- [9] K. Morishige and K. Kawano, *J. Chem. Phys.* **112**, 11023 (2000).
- [10] M. Sliwinska-Bartkowiak, J. Gras, R. Sikorski, R. Radhakrishnan, L. Gelb, and K. E. Gubbins, *Langmuir* **15**, 6060 (1999).
- [11] M. Sliwinska-Bartkowiak, G. Dudziak, R. Sikorski, R. Gras, R. Radhakrishnan, and K. E. Gubbins, *J. Chem. Phys.* **114**, 950 (2001).
- [12] M. Sliwinska-Bartkowiak, G. Dudziak, R. Radhakrishnan and K. E. Gubbins, *Stud. Surf. Sci. Catal.* **144**, 467 (2002).
- [13] K. Morishige and K. Kawano, *J. Phys. Chem. B* **104**, 2894 (2000).
- [14] P. Huber, D. Wallacher, and K. Knorr, *Phys. Rev. B* **60**, 12666 (1999).
- [15] D. Wallacher, V. P. Soprunyuk, A. V. Kityk, and K. Knorr, *Phys. Rev. B* **66**, 014203 (2002).
- [16] K. Morishige, K. Kawano, and T. Hayashigi, *J. Phys. Chem. B* **104**, 10298 (2000).
- [17] P. Huber and K. Knorr, *Phys. Rev. B* **60**, 12657 (1999).
- [18] D. Wallacher and K. Knorr, *Phys. Rev. B* **63**, 104202 (2001).
- [19] V. P. Soprunyuk, D. Wallacher, P. Huber, K. Knorr, and A. V. Kityk, *Phys. Rev. B* **67**, 144105 (2003).
- [20] J. A. Duffy and M. A. Alam, *Langmuir* **16**, 9513 (2000).
- [21] K. Morishige and Y. Ogisu, *J. Chem. Phys.* **114**, 7166 (2001).
- [22] D. Wallacher, R. Ackermann, P. Huber, M. Enderle, and K. Knorr, *Phys. Rev. B* **64**, 184203 (2001).

-
- [23] G. Dosseh, D. Morineau, and C. Alba-Simionesco, *J. Phys. IV* **10**, Pr7-99 (2000)
- [24] E. Gedat, A. Schreiber, J. Albrecht, Th. Emmeler, I. Shenderovich, G. H. Findenegg, H. -H. Limbach, and G. Buntkowsky, *J. Phys. Chem. B* **106**, 1977 (2002).
- [25] G. Dosseh, Y. Xia, and C. Alba-Simionesco, *J. Phys. Chem. B* **107**, 6445 (2003).
- [26] D. Wallacher, V. P. Sopronyuk, K. Knorr and A. V. Kityk, *Phys. Rev. B* **69**, 134207 (2004).
- [27] J. Klein and E. Kumacheva, *Science* **269**, 816 (1995); *J. Chem. Phys.* **108**, 6996 (1998); **108**, 7010 (1998).
- [28] M. Miyahara and K. E. Gubbins, *J. Chem. Phys.* **106**, 2865 (1997).
- [29] M. Maddox and K. E. Gubbins, *J. Chem. Phys.* **107**, 9659 (1997).
- [30] U. Raviv, P. Laurat, and J. Klein, *Nature* **413**, 51 (2001).
- [31] U. Raviv, S. Giasson, J. Frey, and J. Klein, *J. Phys.: Condens. Matter* **14**, 9275 (2002).
- [32] M. Sliwinska-Bartkowiak, G. Dudziak, R. Sikorski, R. Gras, K. E. Gubbins, and R. Radhakrishnan, *Phys. Chem. Chem. Phys.* **3**, 1179 (2001).
- [33] F. Mugele, B. Persson, S. Zilberman, A. Nitzan, and M. Salmeron, *Tribol. Lett.* **12**, 123 (2002).
- [34] K. Kaneko, A. Watanabe, T. Iiyama, R. Radhakrishnan, and K. E. Gubbins, *J. Phys. Chem. B* **103**, 7061 (1999).
- [35] A. Watanabe and K. Kaneko, *Chem. Phys. Lett.* **305**, 71 (1999).
- [36] M. Sliwinska-Bartkowiak, R. Radhakrishnan, and K. E. Gubbins, *Mol. Simul.* **27**, 323 (2001).
- [37] M. Miyahara, M. Sakamoto, H. Kanda, and K. Higashitani, *Stud. Surf. Sci. Catal.* **144**, 411 (2002).
- [38] R. Radhakrishnan, K. E. Gubbins, and M. Sliwinska-Bartkowiak, *J. Chem. Phys.* **112**, 11048 (2000).
- [39] H. Dominguez, M. P. Allen, and R. Evans, *Mol. Phys.* **96**, 209 (1998).
- [40] R. Radhakrishnan and K. E. Gubbins, *Mol. Phys.* **96**, 1249 (1999).
- [41] R. Radhakrishnan, K. E. Gubbins, and M. Sliwinska-Bartkowiak, *J. Chem. Phys.* **116**, 1147 (2002).
- [42] R. Radhakrishnan, K. E. Gubbins, and M. Sliwinska-Bartkowiak, *Phys. Rev. Lett.* **89**, 076101 (2002).
- [43] For a review, see K. J. Strandburg, *Rev. Mod. Phys.* **60**, 161 (1988)
- [44] B. I. Halperin and D. R. Nelson, *Phys. Rev. Lett.* **41**, 121 (1978); D. R. Nelson and B. I. Halperin, *Phys. Rev. B* **19**, 2457 (1979).
- [45] A. P. Young, *Phys. Rev. B* **19**, 1855 (1979)
- [46] C. Ghatak and K. G. Ayappa, *Phys. Rev. E* **64**, 051507 (2001); K. G. Ayappa and C. Ghatak, *J. Chem. Phys.* **117**, 5373 (2002).

-
- [47] A. Vishnyakov and A. V. Neimark, *J. Chem. Phys.* **118**, 7585 (2003).
- [48] A. Patrykiewicz, L. Sałamacha, and S. Sokołowski, *J. Chem. Phys.* **118**, 1891 (2003).
- [49] H. Bock, K. G. Ayappa and K. E. Gubbins, *J. Chem. Phys.* **122**, 094709 (2005).
- [50] H. Kanda, M. Miyahara, and K. Higashitani, *Langmuir* **16**, 8529 (2000).
- [51] J. Hoffmann and P. Nielaba, *Phys. Rev. E* **67**, 036115 (2003).
- [52] S. Arcidiacono, J. H. Walther, D. Poulikakos, D. Passerone and P. Koumoutsakos, *Phys. Rev. Lett.* **94**, 105502 (2005).
- [53] K. Nishio, J. Kōga, T. Yamaguchi and F. Yonezawa, *J. Phys. Soc. Japan* **73**, 627 (2004).
- [54] K. Nishio, J. Kōga, T. Yamaguchi and F. Yonezawa, *Phys. Rev. B* **69**, 214201 (2004).
- [55] K. Nishio, W. Shinoda, T. Morishita and M. Mikami, *J. Chem. Phys.* **122**, 124715 (2005).
- [56] L. Sarkisov and P. A. Monson, *Langmuir* **17**, 7600 (2001).
- [57] Q. Yan, and J. J. de Pablo, *J. Chem. Phys.* **111**, 9509 (1999).
- [58] F. R. Hung, G. Dudziak, M. Sliwinska-Bartkowiak and K. E. Gubbins, *Mol. Phys.* **102**, 223 (2004).
- [59] M. Sliwinska-Bartkowiak, F. R. Hung, E. E. Santiso, B. Coasne, F. R. Siperstein and K. E. Gubbins, *Adsorption* **11**, 391 (2005).
- [60] F. R. Hung, B. Coasne, K. E. Gubbins, E. E. Santiso, F. R. Siperstein and M. Sliwinska-Bartkowiak, *J. Chem. Phys.* **122**, 144706 (2005).
- [61] M. Jazdzewska, F. R. Hung, K. E. Gubbins and M. Sliwinska-Bartkowiak, *Phys. Chem. Chem. Phys.*, submitted (2005).
- [62] J. M. Prausnitz, R. N. Lichtenthaler and E. Gomes de Azevedo, *Molecular Thermodynamics of Fluid Phase Equilibria* 3rd edition, Prentice-Hall, Englewood Cliffs (1999).
- [63] B. Coasne, K. E. Gubbins, F. R. Hung and M. Sliwinska-Bartkowiak, *Mol. Phys.* **102**, 2149 (2004).
- [64] B. Coasne, J. Czwartos, K. E. Gubbins, F. R. Hung and M. Sliwinska-Bartkowiak, *Adsorption* **11**, 301 (2005).
- [65] J. Czwartos, B. Coasne, K. E. Gubbins, F. R. Hung and M. Sliwinska-Bartkowiak, *Mol. Phys.*, in press (2005).
- [66] B. Coasne, J. Czwartos, K. E. Gubbins, F. R. Hung and M. Sliwinska-Bartkowiak, *Stud. Surf. Sci. Catal.*, accepted (2005)
- [67] L. D. Gelb and K. E. Gubbins, *Langmuir* **14**, 2097 (1998)
- [68] R. J.-M. Pellenq and P. E. Levitz, *Mol. Phys.* **100**, 2059 (2002).
- [69] J. Pikunic, C. Clinard, N. Cohaut, K. E. Gubbins, J. M. Guet, R. J.-M. Pellenq, I. Rannou and J.-N. Rouzaud, *Langmuir* **19**, 8565 (2003).

-
- [70] S. K. Jain, J. Pikunic, R. J.-M. Pellenq and K. E. Gubbins, *Adsorption* **11**, 355 (2005).
- [71] M. J. Biggs, A. Buts and D. Williamson, *Langmuir* **20**, 5786 (2004).
- [72] F. R. Siperstein and K. E. Gubbins, *Mol. Simul.* **27**, 339 (2001).
- [73] F. R. Siperstein and K. E. Gubbins, *Langmuir* **19**, 2049 (2003).
- [74] R. Ryoo, C. H. Ko, M. Kruk, V. Antochshuk and M. Jaroniec, *J. Phys. Chem. B* **104**, 11465 (2000).
- [75] S. Jun, S. H. Joo, R. Ryoo, M. Kruk, M. Jaroniec, Z. Liu, T. Ohsuna and O. Terasaki, *J. Am. Chem. Soc.* **122**, 10712 (2000).
- [76] M. W. Maddox, J. P. Olivier and K. E. Gubbins, *Langmuir* **13**, 1737 (1997).
- [77] B. Coasne, A. Grosman, C. Ortega and R. J. M. Pellenq, *Stud. Surf. Sci. Catal.* **144**, 35 (2002).
- [78] Y. He and N. A. Seaton, *Langmuir* **19**, 10132 (2003).
- [79] B. Coasne and R. J.-M. Pellenq, *J. Chem. Phys.* **121**, 3767 (2004); **120**, 2913 (2004).
- [80] V. B. Fenelonov, A. Y. Derevyankin, S. D. Kirik, L. A. Solovyov, A. N. Shmakov, J.-L. Bonardet, A. Gedeon and V. N. Romannikov, *Micropor. Mesopor. Mat.* **44-45**, 33 (2001).
- [81] A. Berenguer-Murcia, J. García-Martínez, D. Cazorla-Amorós, A. Martínez-Alonso, J. M. D. Tascón and A. Linares-Solano, *Stud. Surf. Sci. Catal.* **144**, 83 (2002).
- [82] K. J. Edler, P. A. Reynolds and J. W. White, *J. Phys. Chem. B* **102**, 3676 (1998).
- [83] C. G. Sonwane, S. K. Bhatia and N. J. Calos, *Langmuir* **15**, 4603 (1999).
- [84] S. J. Gregg and K. S. W. Sing, *Adsorption, Surface Area and Porosity*, 2nd edition, Academic Press, London (1982).
- [85] T. Takei and M. Chikazawa, *J. Ceram. Soc. Jpn.* **106**, 353 (1998).
- [86] B. Coasne, F. R. Hung, R. J.-M. Pellenq, F. R. Siperstein and K. E. Gubbins, *Langmuir*, submitted (2005).
- [87] F. R. Hung, B. Coasne, K. E. Gubbins, F. R. Siperstein, M. Thommes and M. Sliwinska-Bartkowiak, *Stud. Surf. Sci. Catal.*, accepted (2005).
- [88] B. Coasne, F. R. Hung, F. R. Siperstein and K. E. Gubbins, *Ann. Chim-Sci. Mat.*, in press (2005).
- [89] S. Bhattacharya, B. Coasne, F. R. Hung and K. E. Gubbins, *Stud. Surf. Sci. Catal.*, accepted (2005).
- [90] F. R. Hung, B. Coasne, M. Sliwinska-Bartkowiak and K. E. Gubbins, *Phys. Rev. B*, to be submitted (2005).

Chapter 2

Freezing/Melting Behavior of CCl₄ within Multi-Walled Carbon Nanotubes

In this chapter, we report experimental and molecular simulation results on freezing and melting of carbon tetrachloride (CCl₄) confined within multi-walled carbon nanotubes (MWCNT) of diameter $D = 5.0$ nm. This combined experimental and simulation study was aimed at obtaining a rigorous picture of the solid-fluid phase behavior for this system. Dielectric relaxation spectroscopy (DRS) measurements were used to determine the experimental melting points of confined CCl₄. The freezing behavior of the adsorbate was also investigated by means of molecular simulations in the grand canonical ensemble, as well as free energy calculations. The structure and thermodynamic stability of the confined phases were determined from the simulations, as well as the temperatures and the order of the phase transitions. Both simulations and experiments show evidence of a rich phase behavior in confinement, with a number of inhomogeneous phases that are stable over extended temperature ranges. Multiple transition temperatures both above and below the bulk melting point were obtained from experiments and simulations, with good agreement between both series of results. Contents of this chapter have been published elsewhere [1-3]. The rest of this chapter is organized as follows. In Sections 2.1 and 2.2 we present details of our experimental and simulation methodology. Our dielectric relaxation spectroscopy results are presented and discussed in Section 2.3. Section 2.4 includes results from our molecular simulations and free energy calculations, as well as a comparison between experiments and simulations. Finally, our concluding remarks are summarized in Section 2.5.

2.1. Experimental Section

The multi-walled carbon nanotube (MWCNT) samples were synthesized at CNRS-Orléans through the catalytic decomposition of acetylene at 600 °C on a $\text{Co}_x\text{Mg}_{(1-x)}\text{O}$ solid solution [4]. The MWCNT samples were purified using concentrated HCl; some of the samples were oxidized by a treatment with CO_2 to open the nanotube tips. Scanning and transmission electron microscopy (SEM/TEM), and nitrogen adsorption measurements showed that the MWCNT had seven molecular layers and a narrow pore size distribution, with average internal and external diameters of 5.0 and 10.0 nm. The carbon tetrachloride samples were reagent grade chemicals, and were distilled twice at reduced pressure before their use in experiments. The conductivity of the purified CCl_4 samples was found to be less than $10^{-16} \Omega^{-1}\text{m}^{-1}$. The MWCNT were kept under vacuum (10^{-3} torr) prior to and during the introduction of the CCl_4 samples; in addition, the MWCNT were heated to 120 °C to remove traces of air and moisture.

Dielectric relaxation spectroscopy (DRS) was used to determine the experimental melting points of confined CCl_4 . The experimental setup consisted of a parallel plate capacitor of empty capacitance $C_0 = 4.2$ pF. A schematic view of the experimental setup is shown in Figure 2.1. The capacitance C and the tangent loss, $\tan(\delta)$ (where δ is the angle by which current leads the voltage) of the capacitor filled with the sample were measured at different temperatures T using a Solartron 1260 gain impedance analyzer for frequencies ω between 1 Hz and 10 MHz. The complex dielectric permittivity $\kappa^* = \kappa_r - i\kappa_i$ is related to the measured quantities by $\kappa_r = C/C_0$, $\kappa_i = \tan(\delta)/\kappa_r$. [5,6]. As a solid phase sample is heated, phase changes such as melting manifest themselves by changes in the C vs. T behavior. The melting temperatures for pure, bulk CCl_4 was determined to be -22.9 °C

(250.3 K). For the case of confined CCl_4 , the sample was introduced between the capacitor plates as a suspension of CCl_4 -filled MWCNT in bulk CCl_4 ; the measurement thus yields an effective permittivity for the sample. During the experiments, the temperature of the sample was controlled with an accuracy of 0.1 K using a cryostat. A measurement of the relaxation times of CCl_4 , which could have given information of the dynamics of the confined phase, was not attempted. The relaxation times for CCl_4 are considerably faster than those for polar molecules such as nitrobenzene, and thus only slow-dynamics processes such as MWS polarization and crystal relaxation would be detected. Moreover, the non-polar nature of CCl_4 produces weak signals in the experiments since the relaxations are mostly due to induced polarization (with frequencies in the range of GHz), rather than orientational polarizability effects, as is the case for adsorption of polar fluids such as nitrobenzene [1,6,7]. Further details of the experimental method are presented elsewhere [5,6].

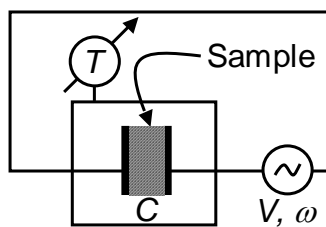


Figure 2.1. Schematic view of the experimental setup used in dielectric relaxation spectroscopy (DRS). A suspension of CCl_4 -filled MWCNT in bulk CCl_4 is introduced between the parallel plates of a capacitor (empty capacitance $C_0 = 4.2$ pF). Phase changes (such as melting) in the system are determined by monitoring the capacitance C of the system as a function of temperature T , upon an electric field with voltage V oscillating at a frequency ω .

2.2. Simulation Details

2.2.1. Models

Carbon tetrachloride was modeled using the Lennard-Jones (LJ) (12, 6) potential, with parameters fitted [8] to reproduce the bulk freezing point and liquid density at bulk coexistence: $\sigma_{ff}=0.514$ nm, $\varepsilon_{ff}/k_B = 366.1$ K. The LJ potential was cut and shifted at a distance of $5\sigma_{ff}$. The multi-walled carbon nanotube was modeled as a structureless, cylindrical pore of density ρ_w , using the potential of Peterson *et al.* [9], so that CCl_4 can only be adsorbed inside the nanotube. The potential parameters for the carbon nanotube were chosen to be equal to those of graphite [10,11]: $\rho_w = 114$ nm⁻³, $\sigma_{ww} = 0.340$ nm and $\varepsilon_{ww}/k_B = 28.0$ K. The Lorentz-Berthelot mixing rules were used to calculate the cross parameters σ_{fw} and ε_{fw} . Modeling the carbon nanotube walls as a structureless solid is expected to be a good approximation, since the size parameter of LJ CCl_4 (0.514 nm) is much larger than the C-C bond length in the carbon nanotubes (0.14 nm), and therefore the effect of surface corrugation is expected to be small. A previous simulation work [12] on freezing/melting of LJ methane ($\sigma_{ff}=0.381$ nm) confined within graphitic slit pores showed quantitatively similar results for both smooth and structured walls.

A cylindrical simulation box with reduced pore diameter $D^* = D/\sigma_{ff} = 9.7$ (corresponding to $D = 5.0$ nm) was considered, and periodic boundary conditions were used at both ends. The reduced cylindrical pore length $L^* = L/\sigma_{ff}$ was fixed at $L^* = 60$, since previous simulations [8,13] of freezing of LJ CCl_4 within slit pores have shown that fluctuations do not destroy the ordered phases for system sizes with $L^* \geq 60$.

2.2.2. Methods

In our simulation runs we followed previous works [12,14] in choosing sets of temperature and chemical potential (T, μ) such that $\mu(T)$ corresponds to the liquid/vapor or solid/vapor coexistence pressure $P(T)$. Such a path implies that the confined phase is always in equilibrium with a saturated vapor in the bulk. The properties of the LJ fluid at coexistence were obtained elsewhere [15].

We have used the parallel tempering scheme in the grand canonical ensemble, as proposed by Yan and de Pablo [16], to determine the equilibrium properties of the adsorbate within the pore. In this method, a grand canonical Monte Carlo (GCMC) simulation is performed simultaneously in n non-interacting replicas with volume V , each one at a different set of values of (T, μ) . Standard GCMC trial moves are attempted at random with equal probability in each one of the replicas. In addition, configuration swaps are randomly attempted between pairs of replicas, subject to specific acceptance criteria [16]. These swap moves provide an effective way to deal with metastability problems and improve phase space sampling. Cell lists [17] were used to speed up the simulation runs, and typical systems had 2800-3800 particles for $D^* = 9.7$ ($D = 5.0$ nm). Thermodynamic properties were averaged over a minimum of 400 million MC steps; however, much longer runs were used for most of the sets of (T, μ) studied, especially near the transition points.

In our parallel tempering grand canonical Monte Carlo (PT-GCMC) simulations, we started from well-equilibrated liquid-like and solid-like configurations obtained from previous GCMC runs at different temperatures. Then, we assigned these configurations randomly to each set of (T, μ) , letting the systems equilibrate. For consistency, we repeated the simulations for $D^* = 9.7$ ($D = 5.0$ nm) using a different set of initial configurations, obtaining similar results. In order to cover all

the phase space of interest and guarantee frequent swaps between replicas, the number of replicas used in a single run was 50 for $D^* = 9.7$ ($D = 5.0$ nm), corresponding to $\Delta T = 2$ K between adjacent replicas. The evolution of the PT-GCMC simulation as a function of the number of Monte Carlo steps was monitored and, after equilibration, it was verified that each configuration visited many sets of (T, μ) along a single simulation run. The acceptance ratio for exchanging configurations was not completely uniform between all the replicas, meaning that the selected conditions of (T, μ) were not optimal and could be further refined. It has been reported [18] that the acceptance probability for swapping moves in a parallel tempering algorithm can be made uniform between all the replicas, by selecting temperature intervals such that all adjacent temperatures are in a fixed ratio. We have not attempted to do that in our simulations. Nevertheless, the ratio T_{i+1}/T_i and μ_{i+1}/μ_i in our simulations had small variations (between 1.01-1.03 for T and 1.005-1.006 for μ); in addition, the fraction of accepted swap moves was over 30% for all the replicas, which is considered satisfactory for a parallel tempering simulation [16,19,20].

2.2.3. Structure analysis

Significant ordering into distinct concentric molecular layers was found for LJ CCl_4 confined within a MWCNT of $D^* = 9.7$ ($D = 5.0$ nm). This is concluded from the analysis of molecular configuration snapshots and the local density profile in the radial direction [21]:

$$\rho^*(\zeta) = \frac{\langle N(\zeta) \rangle}{L\pi \left[(\zeta + \Delta\zeta/2)^2 - (\zeta - \Delta\zeta/2)^2 \right]} \quad (2.1)$$

Where the quantities in brackets $\langle \dots \rangle$ represent ensemble averages, and $N(\zeta)$ is the number of particles with radial coordinate ζ between $(\zeta - \Delta\zeta/2)$ and $(\zeta + \Delta\zeta/2)$. The local density profile of the adsorbed phase along the radial direction is shown in Figure 2.2 at several temperatures, for $D^* = 9.7$ ($D = 5.0$ nm). The maxima in each peak increase and the inter-peak minima decrease as the temperature is reduced, indicating a well-defined layer separation. The density profile at temperatures higher than 229 K exhibits four concentric layers (annuli) of adsorbate and a highly localized quasi-row of particles at the center of the pore; however, five annuli of adsorbate molecules are observed in the density profile at lower temperatures. These observations are corroborated by the snapshots presented in Figure 2.2.

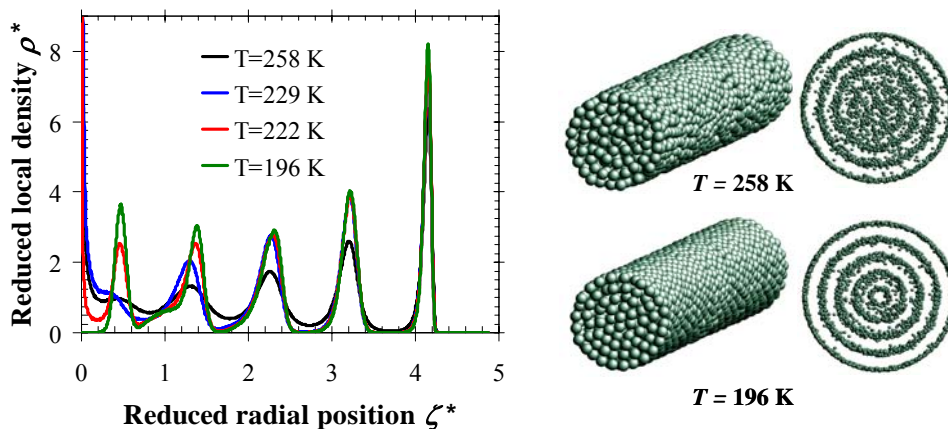


Figure 2.2. Density profile along the radial direction, and snapshots of typical configurations of LJ CCl_4 confined within structureless MWCNT, at different temperatures for $D^* = 9.7$ ($D = 5.0$ nm). The carbon walls are not shown in the snapshots for clarity. Front views of the same snapshots depicting the adsorbed molecules with a reduced diameter are also provided, to help visualize the formation of concentric layers as the temperature decreases.

A representative quasi-2D configuration of the molecules within a layer j can be obtained by cutting the layer along the axial direction z and unrolling it flat. To

study the freezing behavior of each layer, we have followed the methodology of previous works [14,22] in measuring bond order parameters that were sensitive to the degree of crystallinity in the system. First, we identified the nearest neighbors of a given particle i as those molecules k that were in the same layer, and within a distance $r_b = 1.3\sigma_{ff}$ from particle i [14]. This distance corresponds to the first minimum of the radial distribution function in an fcc crystal at bulk coexistence. The vectors \mathbf{r}_{ik} joining the neighbors are called “bonds”. The orientation of such bonds with respect to an arbitrary axis is given by the angle θ_k . Then, the average 2D bond orientational order parameter $\Phi_{6,j}$ of layer j can be determined as [8,23]:

$$\Phi_{6,j} = \langle |\Psi_{6,j}(\mathbf{r})| \rangle \quad (2.2)$$

$$\Psi_{6,j}(\mathbf{r}) = \frac{1}{N_b} \sum_{k=1}^{N_b} \exp(i6\theta_k) \quad (2.3)$$

where N_b is the number of nearest neighbor bonds. The local bond order parameter $\Psi_{6,j}(\mathbf{r})$ measures the hexagonal crystalline bond order of a given molecule at a position \mathbf{r} within layer j . We expect $\Phi_{6,j} = 1$ when the layer has the structure of a perfect, 2D hexagonal crystal and $\Phi_{6,j} = 0$ when the layer has a 2D liquid-like structure (in the thermodynamic limit).

We also monitored the two-dimensional, in-plane positional and orientational pair correlation functions within each layer j . The positional pair correlation function $g_j(r)$ is given by the common radial distribution function measured within the 2D plane formed by each unwrapped layer j , r being the in-layer distance. The orientational pair correlation function $G_{6,j}(r)$ measures correlations between the

local bond order parameter $\Psi_{6,j}$ of two molecules separated by a in-layer distance r , and is given by [8,23]:

$$G_{6,j}(r) = \langle \Psi_{6,j}^*(0) \Psi_{6,j}(r) \rangle \quad (2.4)$$

For the case of $D^* = 9.7$ ($D = 5.0$ nm) we measured $\Phi_{6,j}$, $g_j(r)$ and $G_{6,j}(r)$ for the three outer layers (contact, second and third). The fourth and innermost layers were considered together since we showed they behave similarly upon freezing [1]. In order to get information about the structure of the adsorbate in these inner regions of the pore, we used the 3D bond orientational order parameters proposed by Steinhardt and coworkers [24]:

$$Q_l = \left[\frac{4\pi}{2l+1} \sum_{m=-l}^l |\bar{Q}_{lm}|^2 \right]^{1/2} \quad (2.5)$$

$$W_l = \frac{1}{\left(\sum_{m=-l}^l |\bar{Q}_{lm}|^2 \right)^{3/2}} \sum_{m_1, m_2=-l}^l \begin{pmatrix} l & l & l \\ m_1 & m_2 & -m_1 - m_2 \end{pmatrix} \bar{Q}_{lm_1} \bar{Q}_{lm_2} \bar{Q}_{l(-m_1-m_2)} \quad (2.6)$$

$$\bar{Q}_{lm} = \frac{1}{N_b} \sum_{i=1}^{N_b} Y_{lm}(\theta_i, \varphi_i) \quad (2.7)$$

where θ_i and φ_i are the polar and azimuthal angles giving the orientation of a given nearest neighbor bond, Y_{lm} are spherical harmonics [25], and the matrix in equation (2.6) is a representation of the Wigner $3J$ symbols [26]. We followed previous studies [22] in choosing Q_6 to monitor the freezing behavior in the inner regions of adsorbate; we also measured Q_4 , W_6 and W_4 , finding consistent agreement between

the behavior of the four parameters with temperature. Values of these 3D bond orientational order parameters for some common crystals are presented in Table 2.1.

Table 2.1. Values of the 3D bond orientational order parameters for some common 3D crystals. Taken from Ref. 22.

Crystal	Q_6	Q_4	W_6	W_4
fcc	0.571	0.191	-0.013	-0.159
hcp	0.485	0.097	-0.012	0.134
bcc	0.511	0.036	0.013	0.159
sc	0.354	0.764	0.013	0.159
icosahedral	0.663	0	-0.170	0
liquid	0	0	0	0

To further analyze the structure and the freezing behavior of the adsorbate in the inner regions ($D^* = 9.7$), we generated a “renormalized” 3D positional pair correlation function $g(R)$, given by [27-29]:

$$g(R) = \frac{g_R(R)}{g_u(R)} \quad (2.8)$$

where R represents the 3D distance between molecules in the fourth and innermost layers, $g_R(R)$ is given by the regular 3D radial distribution function, and $g_u(R)$ is the “uniform fluid” pair correlation function. The latter only depends on geometry, and it is a correction due to excluded volume effects [27]. In this particular case, $g_u(R)$ measures the number of pairs separated by a distance R that can be fitted within the cylindrical volume defined by the adsorbate in the inner regions. In addition, to analyze the 3D structure of the confined adsorbate at different temperatures, we measured the renormalized pair correlation function $g(R)$ for all the adsorbate molecules within the pore. The procedure to estimate $g_u(R)$ for this case is similar, the only difference being that the complete pore volume ($D^* = 9.7$)

was considered since the space outside the carbon nanotube was inaccessible to the molecules.

The average properties of the confined phase (amount adsorbed, local density profile in the radial direction, and average order parameters in each layer/region) were determined using the PT-GCMC technique. On the other hand, the in-plane positional and orientational pair correlation functions $g_j(r)$ and $G_{6,j}(r)$, and the “renormalized” 3D positional pair correlation function $g(R)$ were determined from standard GCMC simulations, using the final configurations from parallel tempering as initial configurations for the conditions of interest.

2.2.4. Free energy calculations

Although the use of the parallel tempering technique in simulations greatly reduces the probability of getting trapped in a metastable state, a free energy calculation is required to rigorously determine the thermodynamic stability of each phase, as well as to unambiguously establish the values of the thermodynamic transition temperatures. For the case of $D^* = 9.7$ ($D = 5.0$ nm) we determined the Landau free energy Λ [30] of the adsorbate at different temperatures:

$$\Lambda = -k_B T \ln[P(\Phi_i)] + \text{constant} \quad (2.9)$$

where $P(\Phi_i)$ is the probability distribution function of observing the system having a certain value of a spatially varying order parameter Φ_i . For the case of LJ CCl_4 freezing within a MWCNT with $D^* = 9.7$ ($D = 5.0$ nm), for which there are five layers of adsorbate, the Landau free energy can be expressed as:

$$\Lambda = -k_B T \ln [P(\Phi_{6,contact}; \Phi_{6,second}; \Phi_{6,third}; Q_{6,inner})] + \text{constant} \quad (2.10)$$

The probability distribution function $P(\Phi_{6,contact}; \Phi_{6,second}; \Phi_{6,third}; Q_{6,inner})$ is calculated during a simulation run by collecting statistics of the number of occurrences of combinations of values for these order parameters in a four-dimensional histogram. To collect the statistics, we have combined GCMC simulations and umbrella sampling in partially overlapping windows of an order parameter [8,14,31] with the parallel tempering technique [16] to improve sampling. In essence, the procedure is very similar to that described in Refs. 8 and 31, with some variations to incorporate the parallel tempering scheme. The 2D order parameter of the contact layer, $\Phi_{6,contact}$, was chosen to be the principal coordinate [8,31] for the umbrella sampling procedure, since the adsorbate close to the pore walls is the first to freeze for the case of strongly attractive cylindrical pores [1-3,21,32,33]. The possible range of values of $\Phi_{6,contact}$ was divided into 20 windows, which were found to be enough to ensure the collection of relevant statistics. Starting from well equilibrated liquid phases, we performed a normal PT-GCMC simulation run with 16 replicas, constraining the order parameter $\Phi_{6,contact}$ to be within the range of the first window for all the replicas. During such a simulation, the other three order parameters were not constrained, and the probability distribution function P was calculated for that range of $\Phi_{6,contact}$. After finishing this run, we took the configurations corresponding to the maximum value of $\Phi_{6,contact}$ in the first window, and used them to start the simulations for the second window, which partially overlapped the range of values of $\Phi_{6,contact}$ of the first window. This procedure was repeated until we sampled the complete range of possible values of $\Phi_{6,contact}$. A typical run in each window involved averaging thermodynamic properties over at least 1500 million MC steps.

From this first set of runs we obtained 20 individual pieces of the four-dimensional probability distribution function $P(\Phi_{6,contact}; \Phi_{6,second}; \Phi_{6,third}; Q_{6,inner})$, which can be put together to obtain a continuous function, and obtain the Landau free energies from (10). We could not follow the procedure described in Ref. 31 to join the different pieces of Λ , since the probability P was very close to zero for some regions of phase space, causing Λ to take unphysical high values [see (2.10)]. This situation corresponded to very improbable or even unphysical configurations, e.g., one in which the contact layer is liquid, the second is solid, the third is liquid and the inner regions solid. In order to obtain non-zero values of probability for all possible combinations of our four order parameters, one would need to divide all their possible values in a number of windows, perform simulations constraining these four order parameters to be within the range of each window, and repeat this until all possible combinations of the order parameters would be covered. This would require a prohibitive number of simulations (e.g., if each order parameter range is divided in 10 windows, such a procedure will require 10^4 simulations!).

To overcome these problems, we decided to put together the individual pieces of $P(\Phi_{6,contact}; \Phi_{6,second}; \Phi_{6,third}; Q_{6,inner})$ by adding suitable constants, equal to the average of the differences between probability values found in the overlapping region between adjacent windows of $\Phi_{6,contact}$. This procedure was implemented in the same spirit as the combination of histograms using histogram reweighting techniques [34] After such procedure, we normalized the entire probability distribution function P . In this way, we obtain a single probability distribution hypersurface that is continuous in all the four dimensions, and the values of the four order parameters that correspond to global and local maxima in P (and minima in Λ) can be accurately determined. We do not expect the location of such maxima in P to be altered by the procedure to put together the individual pieces of

P . Those free energy minima can also be compared with PT-GCMC results, providing further assessment of both series of simulations. On the other hand, we are unable to draw conclusions about the accuracy of the free energy barriers between stable and metastable states. Such barriers are subject to strong finite-size effects [8,22,31], and they are not the main objective of our investigation.

Following this procedure, we obtained a first estimate of the probability distribution function $P(\Phi_{6,contact}; \Phi_{6,second}; \Phi_{6,third}; Q_{6,inner})$, by sampling the most important regions of the phase space defined by the four order parameters selected, and without using any weighting function in the umbrella sampling. To further refine the calculation of the probability distribution function, the procedure outlined above was repeated using a weighting function w , in addition to the usual acceptance criteria for parallel tempering GCMC simulations. The weighting function chosen in this case was equal to $w(\Phi_{6,contact}) = 1/P^{(1)}(\Phi_{6,contact})$, where $P^{(1)}(\Phi_{6,contact})$ was calculated by numerically integrating P with respect to all the order parameters except $\Phi_{6,contact}$. The numerical integration was done using the Simpson's rule [35]. It was reported in previous studies [8,22,31] that successive iterations with such a procedure increase the accuracy of the distribution functions, but just one iteration is usually needed to achieve convergence. In this sense, the use of a single order parameter ($Q_{6,inner}$), rather than two ($\Phi_{6,fourth}$ and $\Phi_{6,inner}$), to characterize the degree of order in the inner regions of the pore, reduces the dimensionality of the probability distribution P and facilitates sampling of phase space.

The grand free energy of the phases, $\Omega = -k_B T \ln \Xi$ (where Ξ is the grand partition function) is related to the probability distribution function (and thus to the Landau free energy) by [8,14]:

$$\exp(-\beta\Omega) = \int d\Phi_{6,contact} \int d\Phi_{6,second} \int d\Phi_{6,third} \int dQ_{6,inner} \times P(\Phi_{6,contact}; \Phi_{6,second}; \Phi_{6,third}; Q_{6,inner}) \quad (2.11)$$

where $\beta = 1/k_B T$. To calculate the grand free energy of a phase, the integration in (2.11) is done from the minimum to the maximum values of the four order parameters that characterize the particular phase. The previous calculation determines the grand free energy difference between the phases at a particular value of temperature and chemical potential. To relate the grand free energy of a particular phase at two different values of T and μ , we numerically integrate the following equations [14,36]:

$$\left[\frac{\partial \Omega}{\partial \mu} \right]_{T,V} = -N \quad (2.12)$$

$$\left[\frac{\partial(\Omega/T)}{\partial(1/T)} \right]_{\mu,V} = U - N\mu \quad (2.13)$$

where U and N are the total internal energy and number of molecules of the system, respectively. The thermodynamic transition temperatures and the order of the transitions can be determined from these calculations.

2.3. Experimental Results

Experimental results for the capacitance C as a function of temperature T are presented in Figure 2.3, for CCl_4 confined within open-tip (pretreated with CO_2)

MWCNT with $D = 5.0$ nm. These results were obtained for three different frequencies $\omega = 30, 100$ and 600 kHz. Our experiments started with a sample at $T = 110$ K, to ensure all the CCl_4 is in solid phase. Melting for both bulk and confined CCl_4 is observed in our experiments since the samples consist of a suspension of CCl_4 -filled MWCNT in bulk CCl_4 . All the curves for CCl_4 adsorbed on open-tip carbon nanotubes exhibit a jump at 234 K and changes of slope at five different temperatures: $172, 205, 225, 250$ and 259 K. Bulk CCl_4 melts from a crystalline rhombohedral (Ib) phase to a liquid phase at 250 K, and also undergoes a solid-solid transition between crystalline rhombohedral (Ib) and monoclinic (II) forms at 225 K [37]. Both transitions are observed in our experiments as small changes in the slope of the curves, due to the small volume of bulk CCl_4 in the samples; these transitions were also observed in our experiments with CCl_4 on closed (pristine) MWCNT samples. In Figure 2.3, at temperatures higher than 259 K, C scales with $1/T$; this is a clear sign that all the CCl_4 in the system is liquid. MWCNT are representative of porous materials with strongly attractive walls, where the magnitude of the interactions CCl_4 -carbon walls is high compared to the CCl_4 - CCl_4 interactions. For such systems, experimental and simulation studies have shown that the adsorbate layers near the pore walls are the first to freeze and the last to melt [1-3,8,12,14,21,32,33]. In consequence, the maximum observed for all the curves at 259 K should represent the melting of the confined CCl_4 close to the pore walls. We speculate that the feature observed at the lowest temperature (172 K) may correspond to a possible solid-solid transition inside the pore, although further studies are required to confirm this issue. At 205 K there is a slight change of slope in all the curves, suggesting that an inhomogeneous melting process is starting in the confined phase. These changes take place up to 234 K, where there is a sharp increase in C . Since the adsorbate close to the pore walls melts at 259 K, an inhomogeneous confined phase exists at 234 K and consists of liquid CCl_4 in the center of the pore and solid CCl_4 close to the walls. It is believed

that the nature of the features observed in the C vs. T curves in DRS experiments depend on the amounts of bulk and confined fluid in the sample, since the signal is the sum of the two contributions. Therefore, we varied the amount of CCl_4 in the bulk phase and repeated the DRS experiments; we corroborated our previous results since the changes in the C vs. T curves were observed at essentially the same temperatures.

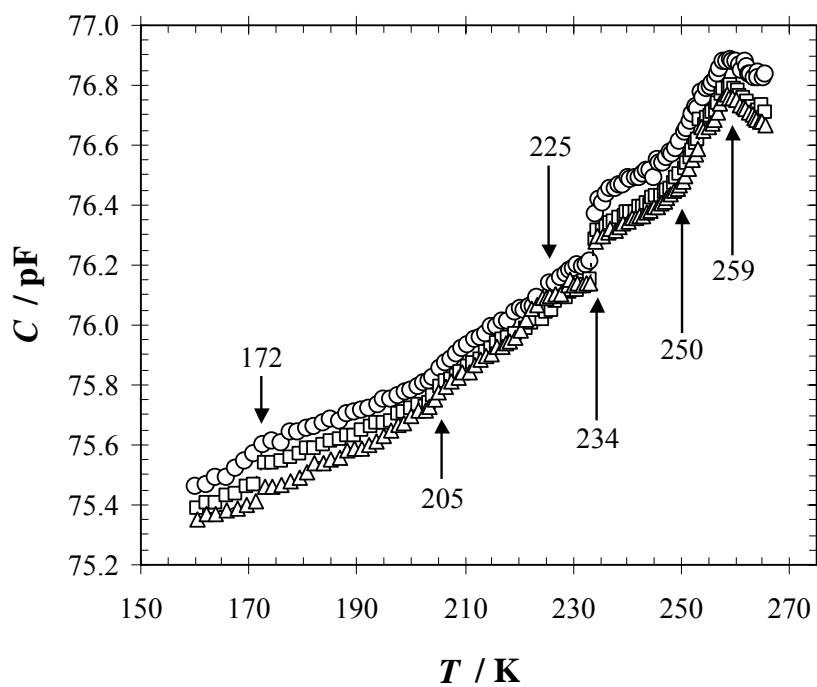


Figure 2.3. Capacitance C as a function of temperature T for CCl_4 adsorbed on open-tip MWCNT, with average internal and external pore diameters of 5.0 nm and 10 nm. The measurements were performed at frequencies ω equal to 30 kHz (circles), 100 kHz (squares) and 600 kHz (triangles). The error bars for the capacitance and temperature are equal to ± 0.01 pF and ± 0.1 K, respectively.

Measurements of the relaxation times for CCl_4 were not attempted. The relaxation times for CCl_4 are considerably faster than those for polar molecules such as nitrobenzene, and thus only slow-dynamics processes such as MWS polarization and crystal relaxation will be detected. Moreover, the non-polar nature of CCl_4

produces weak signals in the experiments since the relaxations are mostly due to induced polarization (with frequencies in the range of GHz), rather than orientational polarizability effects, as is the case for polar fluids such as nitrobenzene. Further experiments are needed to corroborate our analysis. Direct information about the structure of the confined phase cannot be obtained from dielectric relaxation spectroscopy alone. Experimental techniques such as x-ray diffraction and neutron scattering are suitable to determine the structure of the adsorbed phase. On the other hand, comparisons between experiments and simulations can provide some insight and help in the analysis of the results.

2.4. Simulation Results

2.4.1. Grand canonical Monte Carlo simulations

PT-GCMC simulations were performed for LJ CCl_4 within a structureless model MWCNT of $D^* = 9.7$ ($D = 5.0$ nm). The amount of CCl_4 adsorbed within a carbon nanotube is represented as a function of the temperature in Figure 2.4. At relatively high temperatures ($T > 260$ K), the amount adsorbed gradually increase as the temperature decreases. The curve exhibits jumps around 250-260 K and at 210-220 K. Further reduction in the temperature produces slight increases in the amount adsorbed, and GCMC simulations at $T = 177$ K suggest that negligible changes occur at temperatures lower than 192 K. The jumps in the adsorption curve at 250-260 K and 210-220 K suggest that changes in the adsorbate structure take place at these temperature ranges. The confined fluid does not solidify into any of the crystalline lattice structures presented in Table 2.1; rather, the adsorbate forms concentric layers within the pore (Figure 2.1).

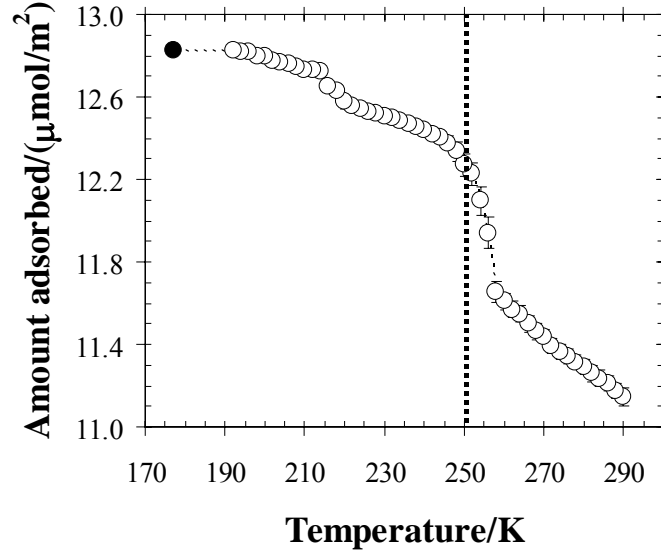


Figure 2.4. Amount adsorbed as a function of temperature for LJ CCl_4 confined in a model structureless, multi-walled carbon nanotube with $D^* = 9.7$ ($D = 5.0$ nm), from PT-GCMC simulations. The black filled symbol represent results from a GCMC simulation performed at $T = 177$ K. The thick dashed line represents the bulk solid-fluid phase transition temperature.

In Figure 2.5 we report the average values of the bond order parameters as a function of temperature. The 2D order parameters $\Phi_{6,j}$ were measured for the three layers close to the walls (contact, second and third), whereas the 3D order parameter $Q_{6,inner}$ was determined for the adsorbate in the center of the pore (fourth and innermost layers). The behavior in the contact and second layers is very similar: a steep increase in $\Phi_{6,j}$ around 250-260 K, followed by slight increases in $\Phi_{6,j}$ with further reduction of the temperature. These results suggest that both molecular layers undergo a transition from isotropic liquid ($\Phi_{6,j} \sim 0.1$, due to finite-size effects) to a defective quasi-2D hexagonal crystal ($\Phi_{6,j} \sim 0.8$) at temperatures around 260 K, which are slightly higher than the bulk freezing point of LJ CCl_4 (251 K). This is in good agreement with the experimental results (Figure 2.3), where the outer layers melt between 250 and 259 K. The change in $\Phi_{6,j}$ for the

third layer in the simulations is more gradual than for the first two layers and occurs over a wider temperature range, around 220-260 K. The adsorbate in the center of the pore shows gradual increases in $Q_{6,inner}$ in the range 220-260 K, followed by a rise between 220 and 190 K, reaching a value of ~ 0.30 at $T=177$ K. This is again in agreement with the experiments (Figure 2.3), where the features observed between 205 and 234 K can be associated with melting in the inner layers. The behavior of the third layer in the simulations, which is intermediate between the behaviors of the outer and inner regions, is probably masked in the experiments by the features we associate with those regions. The transition observed in the experiments at 172 K was not observed in the simulations.

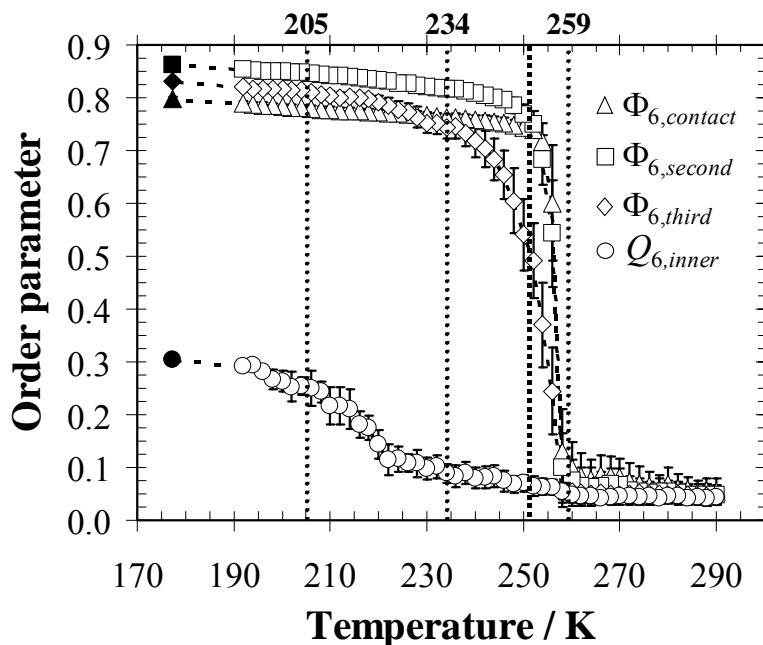


Figure 2.5. Average values of the bond order parameters measured for LJ CCl₄ confined in a structureless MWCNT with $D^* = 9.7$ ($D = 5.0$ nm), as a function of temperature. $\Phi_{6,j}$ was measured for the contact, second and third layers, and $Q_{6,inner}$ is reported for the adsorbate in the center of the pore (fourth and innermost layers). The black filled symbols represent results from a GCMC simulation performed at $T=177$ K. The thick dotted line at 251 K represents the bulk melting point of LJ CCl₄. The three thin dotted lines at 205, 234 and 259 K represent the experimental transition temperatures of CCl₄ within MWCNT with $D = 5.0$ nm, from dielectric relaxation spectroscopy measurements.

In a previous study [1], rather than $Q_{6,inner}$, we measured the 2D order parameters $\Phi_{6,j}$ for the fourth and innermost layers, and we found a similar behavior as the temperature was reduced. This indicates that $Q_{6,inner}$, as well as $\Phi_{6,inner}$ and $\Phi_{6,fourth}$, are equivalent and suitable order parameters to detect freezing of adsorbate in the inner regions, at least for this particular pore size. The difference in the temperature ranges at which each layer undergoes a transition from an isotropic phase to an ordered structure can be explained in terms of a competition between attractive interactions and degree of confinement: strongly attractive walls lead to increases in the adsorbate transition temperatures, whereas geometrical constraints produce depressions in the transition temperatures. The contact layer experiences a strong attraction from the pore wall, and the combined interaction of the pore wall and the contact layer acts upon the second layer. Consequently, these two layers undergo a transition at temperatures slightly higher than the bulk freezing point. In contrast, the fourth and innermost layers experience a weaker effect from the attractive wall potential and are the most geometrically constrained; therefore, the liquid-solid transition occurs at temperatures well below the bulk freezing point, and the ordered phase presents a large number of defects. Finally, the third layer undergoes a transition at intermediate temperatures, since its geometrical constraint is not as severe as in the inner regions and the effect of the pore walls is weaker than in the outer layers.

Results for the 2D positional and bond orientational pair correlation functions $g_j(r)$ and $G_{6,j}(r)$ are shown in Figure 2.6, for the first three layers of CCl_4 within the MWCNT with $D^* = 9.7$ ($D = 5.0$ nm). We also report in this figure the 3D positional pair correlation function $g(R)$ for the inner regions (fourth and innermost layers), which has been corrected for excluded volume effects [27-29]. Correlations in each layer were reported in these figures up to a distance $l = \pi r_l$, where r_l is the radial position where the reduced local density ρ^* reaches a

maximum in each layer [see Figure 2.2]; correlations in the inner regions were arbitrarily reported up to $l \sim 7.25\sigma_{ff}$, the value of l corresponding to the third layer. At $T = 260$ K, $g_j(r)$ and $g(R)$ exhibit liquid-like features and $G_{6,j}(r)$ decays exponentially. Therefore, all adsorbate regions behave as dense liquids (no crystalline order) with short-range positional and bond orientational order (phase A). At $T = 256$ K, the contact and second layers have an intermediate morphology between a quasi-2D hexagonal crystal and a liquid, while the rest of the adsorbate presents liquid-like structure (phase B). The $g_j(r)$ for the contact and second layers shows liquid-like features with extended correlations, as compared to the $g_j(r)$ at 260 K. In addition, the $G_{6,j}(r)$ for these two layers decays at a slower rate, as compared to the $G_{6,j}(r)$ at 260 K; moreover, $\Phi_{6,j}$ for these two layers (figure 2) takes intermediate values between those exhibited by a liquid ($\Phi_{6,j} \sim 0.1$) and a quasi-2D crystal ($\Phi_{6,j} \sim 0.8$). This 2D phase for the contact and second layers resembles a hexatic phase, which is expected in the framework of the KTHNY theory for 2D melting [23,38,39]. This theory involves two continuous transitions: first, between a 2D crystal phase (with quasi-long range positional order and long range bond orientational order) and a hexatic phase (with positional disorder and quasi-long range bond orientational order); and second, between the hexatic phase and the 2D liquid phase (with positional and bond orientational disorder). System size is a key variable in rigorously determining the nature of intermediate phases between 2D crystals and liquids [8,13]. A rigorous system size scaling analysis, which has been done for LJ fluids within slit pores to determine the existence of hexatic phases [13], cannot be performed for cylindrical pores of a few nanometers since the dimensions of the quasi-2D layers of adsorbate are limited by the pore diameter. In consequence, the intermediate phases observed in the contact and second layers at 256 K cannot be rigorously termed hexatic phases; however, they exhibit remnants of hexatic behavior.

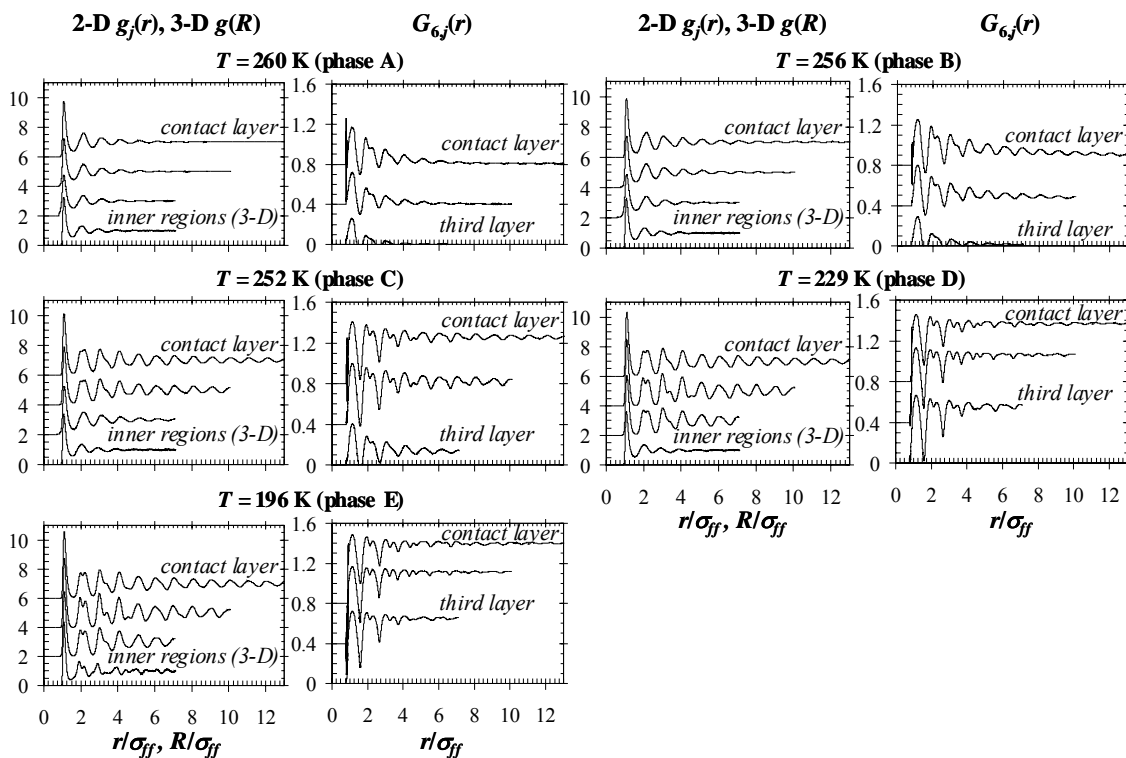


Figure 2.6. 2D positional and bond orientational correlation functions, $g_j(r)$ and $G_{6j}(r)$, for the first three molecular layers of adsorbate, and 3D positional correlation function corrected by excluded volume effects, $g(R)$, for the adsorbate in the center of the pore. r is the in-layer distance, and R represents the 3D distance. Five different confined phases A, B, C, D and E (see text for descriptions) can be observed for LJ CCl_4 within a structureless MWCNT of $D^* = 9.7$ at different temperatures. For clarity, the $g_j(r)$ functions corresponding to the contact, second and third layers have been shifted by +6, +4 and +2, respectively. In a similar way, the $G_{6j}(r)$ functions corresponding to the contact and second layers have been displaced by +0.8 and +0.4, respectively.

At $T = 252$ K, both the contact and second layers appear as quasi-2D hexagonal crystals with defects; the third layer exhibits an intermediate morphology similar to that observed for the first two layers at 256 K, and the center of the pore keeps its isotropic characteristics (phase C). The crystalline nature of both contact and second layers is determined from the features observed in the $g_j(r)$ functions: a large value on the first peak, a first minimum of zero and an incipient splitting in

the second and third peaks. The constant value of $G_{6,j}(r)$ at relatively large r for the two outer layers is also a signature of phases having long range bond orientational order. At $T = 229$ K, the third layer exhibits the same crystalline features as the outer layers, while the inner regions are still liquid-like (phase D). Finally, all the adsorbate has quasi-crystalline morphology at $T = 196$ K (phase E). CCl_4 in the inner regions suffers strong geometrical constraints and consists of frustrated crystals with a large number of defects, as evidenced by the non-zero first minimum in $g(R)$. The temperature must reach values as low as $T = 196$ K to observe non-isotropic features for $g(R)$ in the inner regions of the pore.

2.4.2. Free energy calculations

In order to rigorously determine the thermodynamic stability of each phase, we measured the probability distribution function $P(\Phi_{6,contact}; \Phi_{6,second}; \Phi_{6,third}; Q_{6,inner})$ for the case of LJ CCl_4 within a MWCNT of reduced diameter $D^* = 9.7$ ($D = 5.0$ nm). We used the methodology described in Section 2.2.4 to measure such probabilities at different sets of (T, μ) . In Figure 2.7 we present the first order distribution functions of the probability, $P^{(1)}$, for the four order parameters at a representative temperature, $T = 252$ K. The first order distribution $P^{(1)}$ is obtained by integrating $P(\Phi_{6,contact}; \Phi_{6,second}; \Phi_{6,third}; Q_{6,inner})$ with respect to all the order parameters except one [e.g. $P^{(1)}(\Phi_{6,contact})$ was obtained by integrating P with respect to all the order parameters except $\Phi_{6,contact}$; the same principle applies to $P^{(1)}(\Phi_{6,second})$, $P^{(1)}(\Phi_{6,third})$, and $P^{(1)}(Q_{6,inner})$]. The four $P^{(1)}$ curves span over a wide range of order parameter values, showing that the simulations were able to sample a wide range of phase space. The four global maxima in each of the $P^{(1)}$ functions represent maxima in the total probability distribution function P . Since the Landau free energy Λ is related to the probability

P through (2.10), the combination of the four maxima in $P^{(1)}$ gives the equilibrium configuration within the pore at a given temperature. From Figure 2.7, it can be seen that phase C (contact and second layers as quasi-2D hexagonal crystals with defects, third layer with intermediate morphology between 2D liquid and crystal, and inner regions still liquid-like) is the most stable phase at $T=252$ K, in agreement with results from PT-GCMC simulations (Figures 2.4-2.6). Similar agreement was found for all the temperatures considered in the free energy calculations. This comparison shows that the PT-GCMC simulations are capable of giving results which are at least very close to true equilibrium results, provided that the fraction of accepted swap moves is high enough. For $D^* = 9.7$, such fraction was 30% for the worst case, i.e. between replicas with temperatures around the transition points for the outer layers of adsorbate.

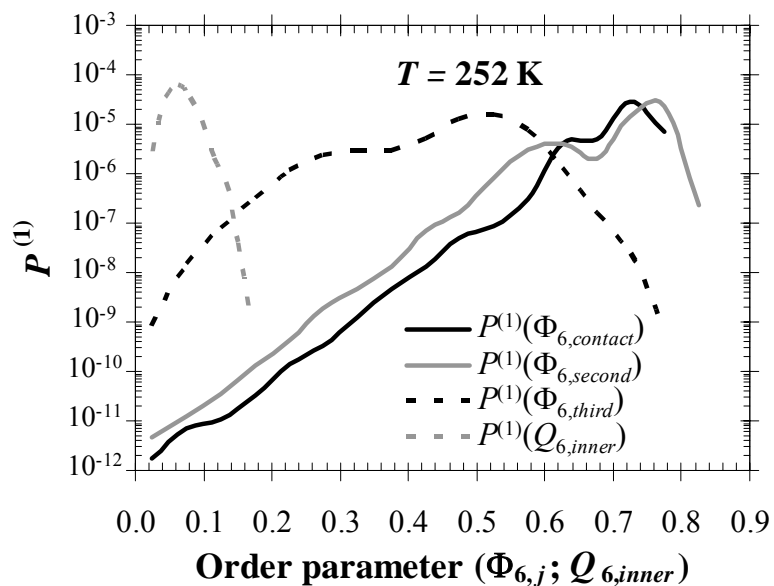


Figure 2.7. First order distribution functions of the probability P for LJ CCl_4 within a structureless MWCNT of $D^* = 9.7$ at $T = 252$ K. The distribution function $P^{(1)}(\Phi_{6,\text{contact}})$ was obtained by numerically integrating P with respect to all the order parameters except $\Phi_{6,\text{contact}}$; the same principle applies to $P^{(1)}(\Phi_{6,\text{second}})$, $P^{(1)}(\Phi_{6,\text{third}})$, and $P^{(1)}(Q_{6,\text{inner}})$.

The grand free energy Ω of the different phases (A-E) can be determined from the probability distribution function $P(\Phi_{6,contact}; \Phi_{6,second}; \Phi_{6,third}; Q_{6,inner})$ by using equations (2.11-2.13). Plots of the grand free energy Ω of the different phases as a function of temperature T near the transition points are shown in Figure 2.8. To facilitate visualization, in each plot we present the difference of grand free energy of each phase with respect to phase A. The most stable phase in each temperature range is the one with the lowest grand free energy, and the intersection between the curves gives us the thermodynamic transition temperatures. The transitions between phases A-B, B-C and C-D occur at $T=256.5$ K, $T=254.0$ K and $T=248.2$ K, and they are first order (the grand free energies intersect with different slopes). These phase transitions involve freezing in the contact, second and third layers of adsorbate. Rather than going directly from quasi-2D isotropic liquid to quasi-2D hexagonal crystals, freezing in these layers occurs via intermediate phases that show remnants of hexatic behavior. According to the KTHNY mechanism of freezing/melting, in a true 2D system the transitions liquid-hexatic and hexatic-crystal are of continuous nature [23,38,39]. Nevertheless, for quasi-2D systems, e.g. LJ fluids confined within narrow slit pores accommodating several molecular layers [8,13], such transitions were found to be first order, due to the interaction between molecules in different layers. For LJ CCl_4 within a cylindrical pore, we have the effect of both interlayer interactions and pore curvature. The latter effect might cause phases B and C (which involve intermediate phases in the contact, second and third layers) to be stable over a relatively small range of temperatures (2.5 K for phase B, 5.8 K for phase C), as compared to what was observed for LJ CCl_4 within strongly attractive slit pores [8], where the hexatic phase was stable over a range of 57 K.

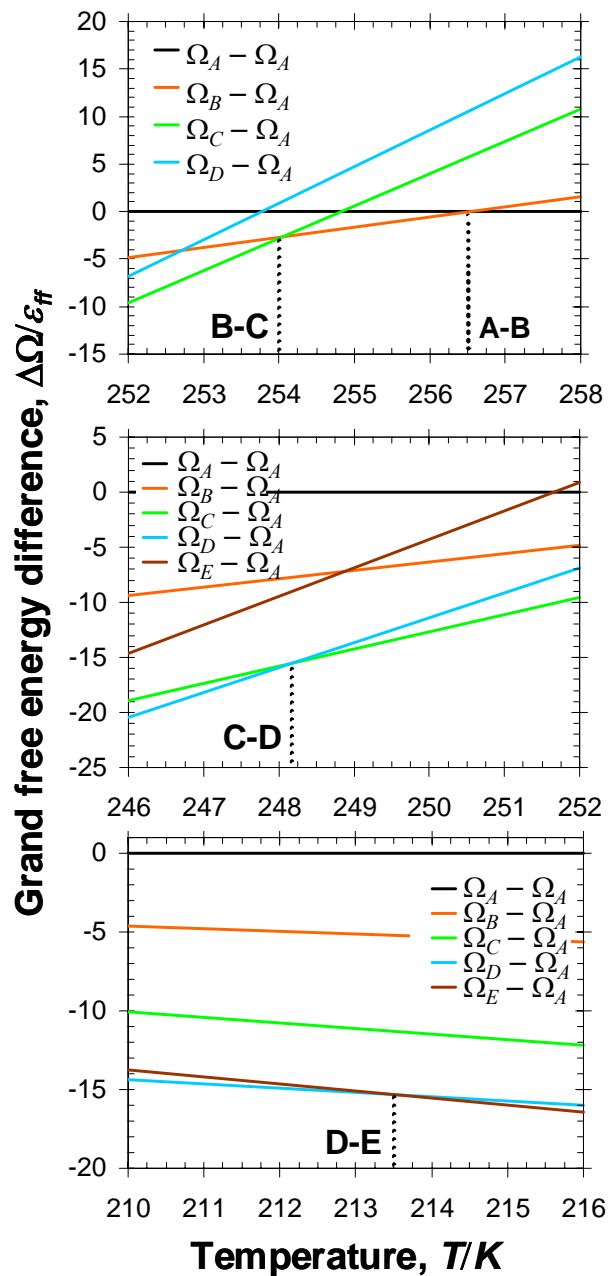


Figure 2.8. Grand free energy Ω of the different phases as a function of temperature T , for LJ CCl_4 confined within a structureless MWCNT of $D^* = 9.7$. To facilitate visualization, the difference of grand free energy of each phase with respect to phase A is presented, and three plots are provided for temperature ranges close to the transition points.

The transition between phases D and E takes place at $T = 213.5$ K, and it is of weaker first order nature as compared to the transitions previously described. The transition temperature and its nature are difficult to establish in this case due to the very small difference in the slopes of Ω . This is in agreement with the results presented in Figure 2.5, where the increase in $Q_{6,inner}$ is more gradual and occurs over a wider temperature range as compared to the contact, second and third layers. The transition between phases D and E involve freezing in the inner regions of the pore, which evolve from liquid-like to frustrated crystal structures with defects due to geometrical constraints. It is reasonable to expect such a transition to be weakly first order, since the differences between these two phases are not very marked. It is important to note that transitions can be observed even in the narrow inner regions, where particles depart from a truly 1D system behavior (with no phase transitions) because of the interactions with the neighboring molecular layers. Similarly, it has been shown [40] that particles forming a 1D system within a zeolite can undergo gas-liquid phase transitions at low temperatures due to pore-pore correlation effects.

The significant changes in the order parameter for the different phases further suggest that all the transitions observed are first order. The change of sign of the grand free energy differences between the phases [i.e., $\Omega_A - \Omega_B > 0$ at the lowest values of (T, μ) , and $\Omega_A - \Omega_B < 0$ at the highest values of (T, μ)], also implies that the phase transitions are first order. All the transition points determined from the free energy calculations are within the range of temperatures determined from the analysis of Figures 2.5 and 2.6. The thermodynamic transition temperatures and the phases involved in each transition are summarized in Table 2.2.

Table 2.2. Thermodynamic transition temperatures and phases involved, for LJ CCl_4 confined within a MWCNT with $D^* = 9.7$, as determined from free energy calculations. See text for descriptions of the different phases.

Transition temperatures	Phases involved
256.5	A-B
254.0	B-C
248.2	C-D
213.5	D-E

In Figure 2.9 we show the 3D positional pair correlation function $g(R)$ for the whole adsorbate within the MWCNT at different temperatures, corrected by excluded volume effects [27-29]. Correlations were measured in this case up to $30\sigma_{ff}$ (half of the total pore length). This function is of particular importance since its Fourier transform can be directly compared with the structure factor measured from scattering experiments. For $D^* = 9.7$, solid-like features in $g(R)$ start to arise at temperatures as high as $T = 252$ K; such features reflect the solidification of the contact and second layers (see Figure 2.5). As the temperature is reduced, the first minimum of $g(R)$ slightly decreases, the splitting in the second peak becomes more evident, and the maximum in all the peaks of $g(R)$ slightly increase. The features observed in $g(R)$ for the whole pore arise since the adsorbate solidifies into different structures in radial and axial directions: molecules form concentric layers in the radial direction, and within each layer, the particles arrange themselves into quasi-2D hexagonal crystals with defects. For distances less than the pore diameter ($R/\sigma_{ff} < 9.7$), $g(R)$ for the whole pore includes characteristics from both structures (in radial and axial directions), and for larger distances the $g(R)$ features mainly reflect the quasi-2D hexagonal crystal morphology. In addition, the features of $g(R)$ for the whole pore indirectly reflect the fact that the different layers of adsorbate solidify at different temperatures.

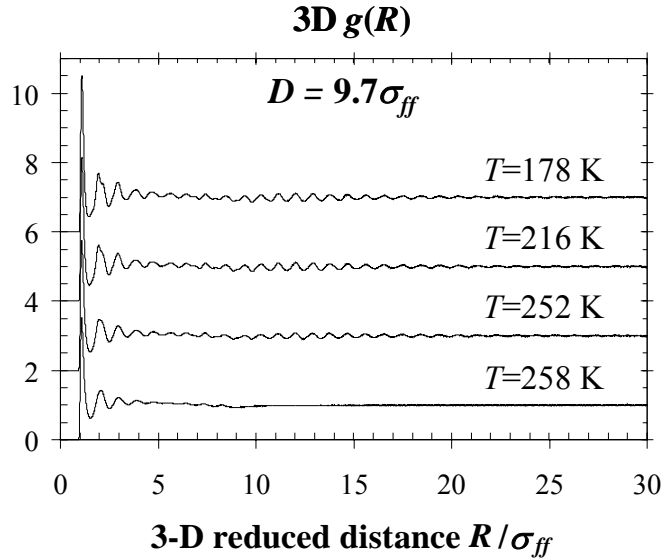


Figure 2.9. 3D positional correlation function $g(R)$, corrected by excluded volume effects, for the all molecules of LJ CCl_4 confined within structureless MWCNT with $D^* = 9.7$, at different temperatures.

2.5. Concluding Remarks

We have presented a combined experimental-simulation study of freezing and melting of carbon tetrachloride confined within multi-walled carbon nanotubes with $D = 5.0$ nm. The structure and thermodynamic stability of the confined phases, as well as the temperatures and the order of the phase transitions, were determined from parallel tempering grand canonical Monte Carlo simulations and free energy calculations using spatially inhomogeneous order parameters. The latter confirm that PT-GCMC simulations give equilibrium results, or at least very close to equilibrium. The simulations show that the adsorbate forms concentric molecular layers that solidify into quasi-2D hexagonal crystals with defects. Freezing in such concentric layers occur via intermediate phases that show remnants of hexatic behavior, in a similar way to the freezing mechanism

previously described for Lennard-Jones particles confined within slit pores [8,13]. The transitions in these layers occur at temperatures that can be above or below the bulk freezing point, depending on pore diameter and distance to the pore wall. Due to strong geometrical constraints, the adsorbate in the inner regions of the pore solidifies into frustrated crystals with a large number of defects at temperatures well below the bulk freezing point. The simulations show evidence of a rich phase behavior in confinement. Five different phases were observed for this particular pore diameter ($D^* = 9.7$). Some of these phases were found to be inhomogeneous (i.e. combinations of crystalline, liquid and frustrated crystalline regions) and stable over extended temperature ranges. The multiple transition temperatures observed in the simulations were consistent with experimental transition temperatures, as determined from dielectric relaxation spectroscopy measurements. Nevertheless, further experiments with different techniques are needed to corroborate our observations. Experimental techniques such as x-ray diffraction and neutron scattering would allow us to determine the structure of the confined adsorbate.

2.6. References

-
- [1] F. R. Hung, G. Dudziak, M. Sliwinska-Bartkowiak and K. E. Gubbins, *Mol. Phys.* **102**, 223 (2004).
 - [2] M. Sliwinska-Bartkowiak, F. R. Hung, E. E. Santiso, B. Coasne, F. R. Siperstein and K. E. Gubbins, *Adsorption* **11**, 391 (2005).
 - [3] F. R. Hung, B. Coasne, K. E. Gubbins, E. E. Santiso, F. R. Siperstein and M. Sliwinska-Bartkowiak, *J. Chem. Phys.* **122**, 144706 (2005).
 - [4] S. Delpeux, K. Szostak, E. Franckowiak, S. Bonnamy and F. Béguin, *J. Nanosc. Nanotec.* **2**, 481 (2002).
 - [5] A. Chelkowski, *Dielectric Physics*, Elsevier, New York (1980).
 - [6] M. Sliwinska-Bartkowiak, J. Gras, R. Sikorski, R. Radhakrishnan, L. Gelb and K. E. Gubbins, *Langmuir* **15**, 6060 (1999).

-
- [7] M. Sliwinska-Bartkowiak, G. Dudziak, R. Sikorski, R. Gras, R. Radhakrishnan and K. E. Gubbins, *J. Chem. Phys.* **114**, 950 (2001).
- [8] R. Radhakrishnan, K. E. Gubbins and M. Sliwinska-Bartkowiak, *J. Chem. Phys.* **116**, 1147 (2002).
- [9] B. K. Peterson, J. P. R. B. Walton and K. E. Gubbins, *J. Chem. Soc., Faraday Trans. 2* **82**, 1789 (1986).
- [10] W. A. Steele, *Surf. Sci.* **36**, 317 (1973)
- [11] W. A. Steele, *The Interaction of Gases with Solid Surfaces*, Pergamon Press, Oxford (1974).
- [12] M. Miyahara and K. E. Gubbins, *J. Chem. Phys.* **106**, 2865 (1997).
- [13] R. Radhakrishnan, K. E. Gubbins and M. Sliwinska-Bartkowiak, *Phys. Rev. Lett.* **89**, 076101 (2002).
- [14] R. Radhakrishnan and K. E. Gubbins, *Mol. Phys.* **96**, 1249 (1999).
- [15] D. A. Kofke, *J. Chem. Phys.* **98**, 4149 (1993); R. Agrawal and D. A. Kofke, *Mol. Phys.* **85**, 43 (1995).
- [16] Q. Yan and J. J. de Pablo, *J. Chem. Phys.* **111**, 9509 (1999).
- [17] D. Frenkel and B. Smit, *Understanding Molecular Simulation: from Algorithms to Applications*, 2nd ed., Academic Press, London (2002).
- [18] D. A. Kofke, *J. Chem. Phys.* **117**, 6911 (2002)
- [19] Y. Sugita, A. Kitao and Y. Okamoto, *J. Chem. Phys.* **113**, 6042 (2000).
- [20] R. Faller, Q. Yan and J. J. de Pablo, *J. Chem. Phys.* **116**, 5419 (2002).
- [21] H. Kanda, M. Miyahara and K. Higashitani, *Langmuir* **16**, 8529 (2000).
- [22] P. R. ten Wolde, M. J. Ruiz-Montero and D. Frenkel, *J. Chem. Phys.* **104**, 9932 (1996); R. M. Lynden-Bell, J. S. van Duijneveldt and D. Frenkel, *Mol. Phys.* **80**, 801 (1993); J. S. van Duijneveldt and D. Frenkel, *J. Chem. Phys.* **96**, 4655 (1992)
- [23] B. I. Halperin and D. R. Nelson, *Phys. Rev. Lett.* **41**, 121 (1978); D. R. Nelson and B. I. Halperin, *Phys. Rev. B* **19**, 2457 (1979).
- [24] P. J. Steinhardt, D. R. Nelson and M. Ronchetti, *Phys. Rev. B* **28**, 784 (1983).
- [25] C. G. Gray and K. E. Gubbins, *Theory of Molecular Liquids*, Clarendon Press, Oxford (1984).
- [26] L. D. Landau and E. M. Lifshitz, *Quantum Mechanics*, Pergamon Press, New York (1965).
- [27] A. K. Soper, F. Bruni and M. A. Ricci, *J. Chem. Phys.* **109**, 1486 (1998); A. K. Soper, *J. Phys.: Condens. Matter* **9**, 2399 (1997).
- [28] D. Morineau and C. Alba-Simionesco, *J. Chem. Phys.* **118**, 9389 (2003)
- [29] P. Gallo, M. A. Ricci, and M. Rovere, *J. Chem. Phys.* **116**, 342 (2002)
- [30] L. D. Landau and E. M. Lifshitz, *Statistical Physics*, 3rd ed., Pergamon Press, London (1980).
- [31] R. Radhakrishnan and B. L. Trout, *J. Chem. Phys.* **117**, 1786 (2002).
- [32] M. Maddox and K. E. Gubbins, *J. Chem. Phys.* **107**, 9659 (1997).

-
- [33] J. Hoffmann and P. Nielaba, *Phys. Rev. E* **67**, 036115 (2003).
- [34] M. Ferrenberg and R. H. Swendsen, *Phys. Rev. Lett.* **61**, 2635 (1988); **63**, 1195 (1989).
- [35] W. H. Press, W. T. Vetterlin, S. A. Teukolsky, B. P. Flannery, *Numerical Recipes in Fortran 77*, 2nd ed., Cambridge Press, New York (2001).
- [36] B. K. Peterson and K. E. Gubbins, *Mol. Phys.* **62**, 215 (1987).
- [37] E. S. Domalski and E. D. Hearing, in *NIST Chemistry WebBook, NIST Standard Reference Database Number 69*, P. J. Linstrom and W. G. Mallard (Eds.), March 2003, National Institute of Standards and Technology, Gaithersburg, MD 20899 (<http://webbook.nist.gov>).
- [38] A. P. Young, *Phys. Rev. B* **19**, 1855 (1979)
- [39] For a review, see K. J. Strandburg, *Rev. Mod. Phys.* **60**, 161 (1988)
- [40] R. Radhakrishnan and K. E. Gubbins, *Phys. Rev. Lett.* **79**, 2847 (1997).

Chapter 3

Effect of Confinement on Freezing of CCl₄ within Multi-Walled Carbon Nanotubes

In this chapter, we present a combined experimental and simulation study aimed at determining the effect of confinement on freezing and melting of CCl₄ inside open-tip multi-walled carbon nanotubes (MWCNT) of different pore sizes. The melting points of the adsorbate were determined from dielectric relaxation spectroscopy measurements, and two different pore diameters D were considered, 4.0 and 2.8 nm. The freezing behavior of Lennard-Jones (LJ) CCl₄ within model MWCNT of similar diameters, 3.9 and 2.8 nm, was also investigated by means of molecular simulations in the grand canonical ensemble. In both cases, a single transition temperature well above the bulk melting point was obtained for confined CCl₄. These results contrast with what was obtained in our previous measurements using carbon nanotubes with a pore diameter of 5.0 nm (Chapter 2), where multiple transition temperatures both above and below the bulk melting point of CCl₄ were observed. Our experimental measurements are consistent with our molecular simulation results. Although the simulations overestimate the temperatures in which melting upon confinement occurs, both simulations and experiments suggest that all regions of adsorbate freeze at the same temperature, and freezing occurs at higher temperatures upon reduction of the pore diameter. Contents from this chapter have been published elsewhere [1,2].

The rest of this chapter is organized as follows. In Sections 3.1 and 3.2 we summarize our experimental and simulation methodology. Our dielectric relaxation spectroscopy results are presented and discussed in Section 3.3; we also compare these experimental results with those previously obtained for MWCNT

with a diameter of 5.0 nm (Section 2.3). Molecular simulation results for LJ CCl₄ within model MWCNT of $D = 3.9$ and 2.8 nm are included in Section 3.4, together with a comparison with simulation results obtained for CCl₄ within MWCNT with $D = 5.0$ nm (Section 2.4), as well as comparisons between experiments and simulations for the smaller MWCNT. Finally, our concluding remarks are summarized in Section 3.5.

3.1. Experimental Section

In our experiments we have used multi-walled carbon nanotubes (MWCNT) purified samples from Nanocyl S.A. (Sambreville, Belgium). The samples were oxidized by a treatment with CO₂ to open the MWCNT tips. We have used two different samples with narrow pore size distributions and two different average inner diameters, 4.0 nm and 2.8 nm, as determined from transmission electron microscopy (TEM), as well as scanning electron microscopy and nitrogen adsorption measurements. The pretreatment of the CCl₄ and MWCNT samples, as well as the details of the dielectric relaxation spectroscopy (DRS) measurements were previously described in Section 2.1.

3.2. Simulation Details

The simulation models were previously described in detail in Section 2.2.1. Two different reduced pore diameter were studied, $D^* = D/\sigma_{ff} = 7.5$ and 5.5 (corresponding to $D = 3.9$ and 2.8 nm, respectively). Regarding the simulation methods, we have used the parallel tempering scheme in the grand canonical

ensemble, as described in Section 2.2.2, to determine the equilibrium properties of the adsorbate within the pore. Typical systems had 1700-2200 molecules for $D^* = 7.5$ ($D = 3.9$ nm), and 900-1100 particles for $D^* = 5.5$ ($D = 2.8$ nm). Thermodynamic properties were averaged over a minimum of 400 million MC steps; however, much longer runs were used for most of the sets of (T, μ) studied, especially near the transition points. In order to cover all the phase space of interest and guarantee frequent swaps between replicas, the number of replicas used in a single run was 28 for $D^* = 7.5$, and 32 for $D^* = 5.5$, corresponding to $\Delta T = 4$ and 5 K, respectively, between adjacent replicas. The rest of the simulation methodology is the same as presented in Section 2.2.2.

Regarding the structure analysis, in the previous chapter it was found that Lennard-Jones (LJ) CCl_4 confined within a MWCNT of $D^* = 9.7$ ($D = 5$ nm) did not solidify into 3D crystalline structures commonly observed in bulk phases. We can expect the same behavior for smaller pore diameters since the geometrical constraints will be more important. As in the previous chapter, significant ordering into distinct concentric molecular layers was found for the two pore diameters considered, as concluded from the analysis of molecular configuration snapshots and the local density profile in the radial direction [equation (2.1)]. The local density profile of the adsorbed phase along the radial direction is shown in Figure 3.1 at several temperatures for $D^* = 7.5$ ($D = 3.9$ nm). The maxima in each peak increase and the inter-peak minima decrease as the temperature is reduced, indicating a well-defined layer separation. For $D^* = 7.5$ there are three annuli of particles and a quasi-row of molecules at the center of the pore, for the whole range of temperatures studied. These observations are corroborated by the snapshots presented in Figure 3.1.

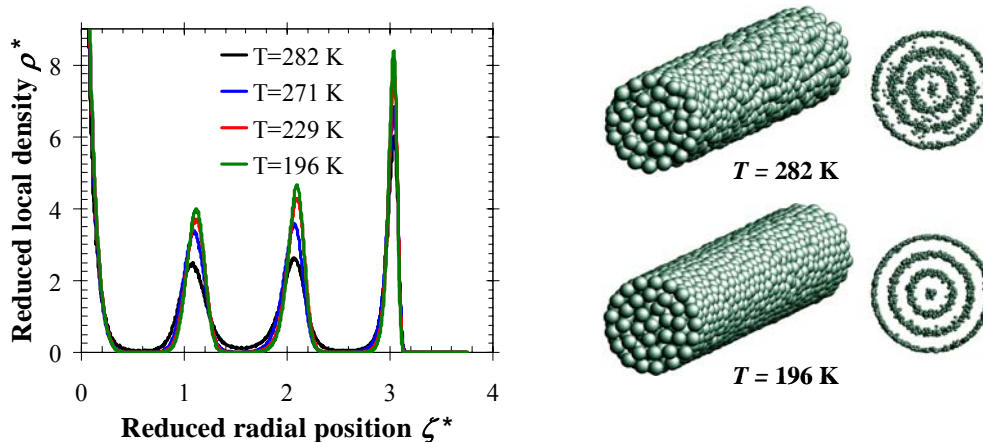


Figure 3.1. Density profile along the radial direction, and snapshots of typical configurations of LJ CCl_4 confined within structureless MWCNT, at different temperatures for $D^* = 7.5$ ($D = 3.9$ nm). The carbon walls are not shown in the snapshots for clarity. Front views of the same snapshots depicting the adsorbed molecules with a reduced diameter are also provided, to help visualize the formation of concentric layers as the temperature decreases.

The density profile for $D^* = 5.5$ (not shown) exhibits two concentric layers and a center quasi-row of molecules for all the temperatures studied, a similar behavior to that observed for $D^* = 7.5$. These results contrast to what was observed for CCl_4 within MWCNT of $D^* = 9.7$ ($D = 5$ nm), where the density profile at temperatures higher than 229 K exhibits four concentric layers (annuli) of adsorbate and a highly localized quasi-row of particles at the center of the pore; however, five annuli of adsorbate molecules are observed in the density profile at lower temperatures (see Figure 2.1). For the case of $D^* = 7.5$ and 5.5, we monitored the 2D order parameters $\Phi_{6,j}$ [equations (2.2) and (2.3)], as well as the two-dimensional, in-plane positional and orientational pair correlation functions $g_j(r)$ and $G_{6,j}(r)$ [equation (2.4)] for all the layers j except the innermost (a highly localized quasi-row of particles at the center of the pore), for which we monitored the local density of adsorbate ρ_{inner}^* . In addition, to analyze the 3D structure of the confined adsorbate at different temperatures, we measured the renormalized pair

correlation function $g(R)$ [equation (2.8)] for all the adsorbate molecules within the two pore diameters considered; to estimate $g_{ii}(R)$ we considered the complete pore volume ($D^* = 7.5$ and 5.5), since the space outside the carbon nanotube was inaccessible to the molecules. A more detailed description of the structure analysis procedure was presented in Section 2.2.3.

3.3. Experimental Results

In Figure 3.2 we present experimental measurements of the capacitance C as a function of temperature T , for CCl_4 confined within MWCNT with an internal diameter $D = 4.0$ nm. These results were obtained for two different frequencies $\omega = 100$ and 600 kHz, for open-tip (pretreated with CO_2) MWCNT. Our experiments started with a sample at $T = 110$ K, to ensure all CCl_4 is in solid phase. Melting for both bulk and confined CCl_4 is observed in our experiments since the samples consist of a suspension of CCl_4 -filled MWCNT in bulk CCl_4 . Both curves exhibit a sharp jump that starts at $T \sim 226$ K and ends at $T \sim 228$ K. This transition should correspond to bulk CCl_4 undergoing a solid-solid transition between crystalline rhombohedral (Ib) and monoclinic (II) forms, which has been reported [3] to occur at 225 K. As the temperature is increased, we observe a small “bump” whose maximum is located at $T \sim 250$ K. This feature corresponds to melting of bulk CCl_4 from a crystalline rhombohedral (Ib) phase to a liquid phase at 250 K [3]. We observe a second “bump” whose maximum is at a much higher temperature, $T \sim 272$ K. This temperature does not correspond to any known transition for bulk CCl_4 , and therefore may represent melting of CCl_4 within the MWCNT. In support of this argument, we note that MWCNT are representative of porous materials with strongly attractive walls, where the magnitude of the interactions CCl_4 -carbon walls is high compared to the CCl_4 - CCl_4 interactions. For such systems we can

expect an increase of the melting temperature in confinement, as compared to the bulk value. It is believed that the nature of the features observed in the C vs. T curves in DRS experiments depend on the amounts of bulk and confined fluid in the sample, since the signal is the sum of the two contributions. Therefore, we varied the amount of CCl_4 in the bulk phase and repeated the DRS experiments; we corroborated our previous results since the changes in the C vs. T curves were observed at essentially the same temperatures.

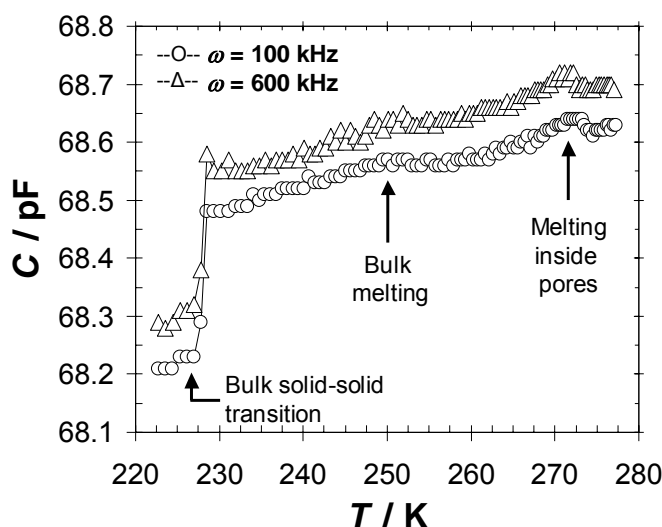


Figure 3.2. Capacitance C as a function of temperature T for CCl_4 in open-tip MWCNT with an average internal pore diameter of 4.0 nm. The measurements were performed at frequencies ω equal to 100 kHz (circles) and 600 kHz (triangles). The error bars for the capacitance and temperature are equal to ± 0.01 pF and ± 0.1 K, respectively.

For the case of CCl_4 within open-tip MWCNT with an internal diameter $D = 2.8$ nm, in Figure 3.3 we show experimental results for the capacitance C as a function of temperature T for a single value of frequency $\omega = 600$ kHz. Two jumps are observed at $T \sim 225$ K and $T \sim 250$ K, and a change of slope takes place at $T \sim 287$ K. As discussed previously, the first two transitions should correspond to the rhombohedral-monoclinic solid-solid transition, and to melting of bulk CCl_4 .

Similarly, the transition taking place at 287 K may represent the point where all CCl_4 within the MWCNT is in liquid phase.

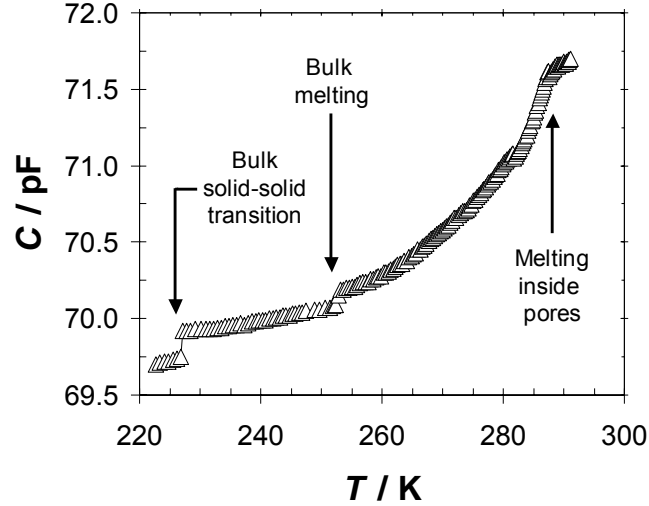


Figure 3.3. Capacitance C as a function of temperature T for CCl_4 in open-tip MWCNT with an average internal pore diameter of 2.8 nm. The measurements were performed at frequencies ω equal to 600 kHz. The error bars for the capacitance and temperature are equal to ± 0.01 pF and ± 0.1 K, respectively.

3.3.1. Comparison with experimental results, MWCNT with $D = 5.0$ nm

The results for freezing/melting of CCl_4 in MWCNT presented in this section present some differences with respect to results reported for CCl_4 within MWCNT with $D = 5.0$ nm (Chapter 2). For this average internal diameter, from the experiments we observed three phase transitions that could be related with melting of confined CCl_4 , at $T \sim 205$ K, $T \sim 234$ K and $T \sim 259$ K (Section 2.3); in addition, those transitions take place at temperatures below and above the bulk melting point of CCl_4 ($T = 250$ K). In contrast, in the present study, only one transition was associated with melting of confined CCl_4 in each case, $T \sim 272$ K ($D = 4.0$ nm, Figure 3.2) and $T \sim 287$ K ($D = 2.8$ nm, Figure 3.3); those temperatures are well above the melting point of bulk CCl_4 . We note that the

melting process upon confinement could have started at lower temperatures, since the C vs. T curves exhibit changes of slope at $T \sim 265$ K ($D = 4.0$ nm, Figure 3.2), and $T \sim 281$ K ($D = 2.8$ nm, Figure 3.3). Our finding of an increase in the confined melting temperature as the pore size is reduced is consistent with results for fluids confined in slit-like, strongly attractive pores by Klein and Kumacheva [4] and Miyahara and coworkers [5]: both studies report that a reduction in pore size leads to a confined liquid to solid phase transition at temperatures well above the bulk freezing point.

Further experiments are needed to corroborate our analysis. Direct information about the structure of the confined phase cannot be obtained from dielectric relaxation spectroscopy alone. Experimental techniques such as x-ray diffraction and neutron scattering are suitable to determine the structure of the adsorbed phase. On the other hand, comparisons between experiments and simulations can provide some insight and help in the analysis of the results.

3.4. Simulation Results

Parallel tempering grand canonical Monte Carlo (PT-GCMC) simulations were performed to study the freezing behavior of LJ CCl_4 confined within structureless MWCNT of diameters $D^* = 7.5$ ($D = 3.9$ nm) and $D^* = 5.5$ ($D = 2.8$ nm). We did not attempt to perform free energy calculations for these pore diameters, since for $D^* = 9.7$ ($D = 5.0$ nm) it was shown that PT-GCMC simulations give results very close to true equilibrium results (see Chapter 2). The amount adsorbed as a function of temperature for $D^* = 7.5$ ($D = 3.9$ nm) and $D^* = 5.5$ ($D = 2.8$ nm) is presented in Figure 3.4.

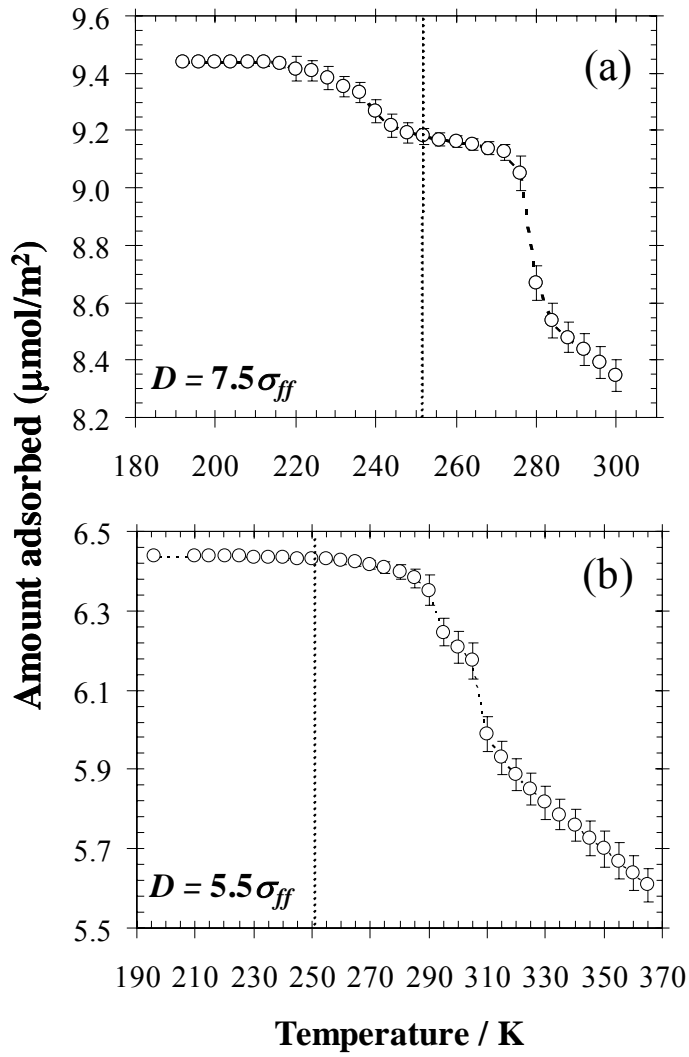


Figure 3.4. Amount adsorbed as a function of temperature for LJ CCl_4 confined within a structureless MWCNT of (a) $D^* = 7.5$ ($D = 3.9$ nm), and (b) $D^* = 5.5$ ($D = 2.8$ nm). The thick dotted line represents the bulk melting point of LJ CCl_4 for all cases.

For $D^* = 7.5$ [Figure 3.4 (a)], the quantity of adsorbate increases gradually as the temperature decreases, up to temperatures around 276-284 K, where a jump is observed. Further reduction in the temperature produces increases in the amount adsorbed within the MWCNT; the slope of the curve is higher for the range $216 \text{ K} < T < 248 \text{ K}$, as compared to that for $248 \text{ K} < T < 276 \text{ K}$. For $T < 216 \text{ K}$,

further reduction of temperature produces negligible variations in the curve. Similarly, for $D^* = 5.5$ [Figure 3.4 (b)] the quantity of adsorbate increases gradually up to 305-310 K, when a steep rise in the curve is observed. The amount adsorbed increases again gradually until another small jump in the curve is seen at 290-295 K and finally reaches a plateau around 265 K.

In Figure 3.5 we show the average 2D bond order parameters $\Phi_{6,j}$ as a function of temperature for the different layers of adsorbate, except the innermost (a highly localized quasi-row of particles at the center of the pore), for which we monitored the local density of adsorbate ρ_{inner}^* . For $D^* = 7.5$, Figure 3.5 (a) shows steep jumps in the average order parameter values of the contact and second layers in the range 276-284 K. The increases in order parameter and local density are slightly more gradual for the third and innermost layers, respectively, and occur for $268 \text{ K} < T < 284 \text{ K}$. Analysis of snapshots from typical configurations indicate that, as the local density increases in the innermost layer with reduction of temperature, molecules in this layer become more localized around the pore axis. Nevertheless, the innermost layer does not become a perfect 1D system even at the lowest temperature studied ($T = 192 \text{ K}$). By comparing Figures 3.4 (a) and 3.5 (a), it can be established that the jump observed in the amount adsorbed around 276-284 K [Figure 3.4 (a)] is associated with freezing of the contact, second and third layers of adsorbate, as well as with the increase in the local density of the innermost layer. All these changes occur at temperatures well above the bulk freezing point (251 K for LJ CCl_4). For temperatures between 216 K and 248 K, the rate of increase of the average order parameter for the second layer [Figure 3.5 (a)] is slightly higher than those for the other layers, and therefore the features observed in the curve of amount adsorbed at $216 \text{ K} < T < 248 \text{ K}$ [Figure 3.4 (a)] can be associated to the increase of crystalline order in the second layer.

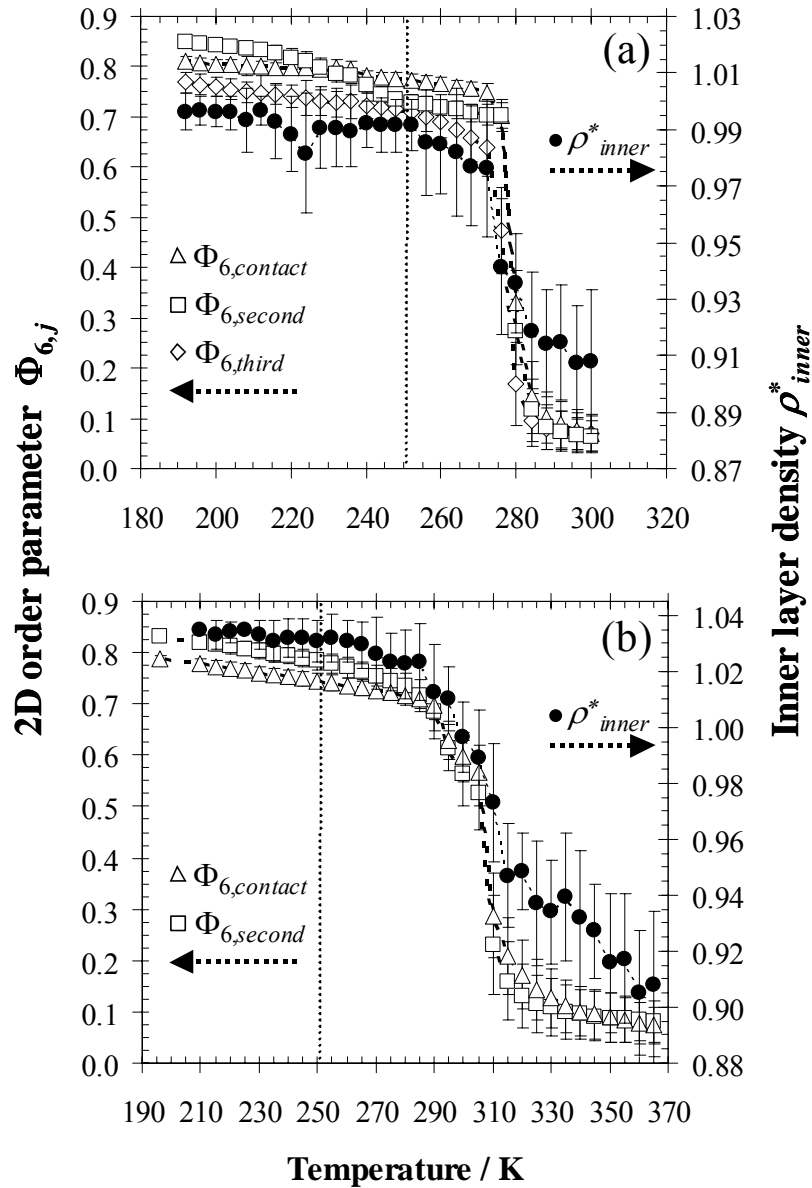


Figure 3.5. Average values of the 2D bond order parameters $\Phi_{6,j}$ (open symbols, left ordinate axis), and reduced local density for the innermost layer ρ_{inner}^* (black filled circles, right ordinate axis), as a function of temperature, for (a) $D^* = 7.5$ ($D = 3.9$ nm), and (b) $D^* = 5.5$ ($D = 2.8$ nm). The thick dotted line represents the bulk melting point of LJ CCl_4 for all cases.

For $D^* = 5.5$ [Figure 3.5 (b)], steep increases in the 2D order parameter values are observed for both contact and second layers at 305-310 K; similarly, the local density for the innermost layer also increases in this temperature range. Therefore, the contact and second molecular layers freeze in this temperature range; similarly, molecules in the innermost layer become more localized around the pore axis around these temperatures, which are significantly higher than the bulk freezing point. All these changes lead to the steep rise in the amount adsorbed at 305-310 K [Figure 3.4 (b)]. The small jump in the amount adsorbed around 290-295 K can be associated with a higher rate of increase of the order parameter for the second layer [Figure 3.5 (b)], as compared to that for the contact, as observed for $D^* = 7.5$.

The structure of the confined phase within the MWCNT with $D^* = 7.5$ and 5.5 can be further determined from the analysis of the in-plane positional and bond orientational pair correlation functions $g_j(r)$ and $G_{6,j}(r)$. For the case of $D^* = 7.5$, at $T = 282$ K the contact, second and third layers have a liquid-like structure, and the innermost layer exhibits relatively low values of local density [structure A, similar to phase A for $D^* = 9.7$ ($D = 5.0$ nm), Figure 2.6]. The intermediate quasi-2D phases are seen again in the contact, second and third layers at $T = 280$ K, and ρ_{inner}^* starts to increase steeply (structure B). At this temperature, the contact, second and third layers exhibit behaviors similar to what was observed for $D^* = 9.7$ at $T = 256$, 256 and 252 K, respectively (Figure 2.6), i.e. extended correlations in $g_j(r)$ and $G_{6,j}(r)$ decays at a slower rate as compared to that observed at $T = 282$ K. Also, the average order parameter of the contact, second and third layers takes intermediate values between those of a quasi-2D liquid and a quasi-2D hexagonal crystal [see Figure 3.5 (a)]. At $T = 270$ K, the contact, second and third layers behave as quasi-2D hexagonal crystals with defects, and the innermost layer presents a relatively high value of ρ_{inner}^* (structure C, equivalent to phase D for

$D^* = 9.7$, Figure 2.6). Further reduction of temperature only produces changes in packing, especially in the second molecular layer.

It is important to mention that, for $D^* = 7.5$ ($D = 3.9$ nm), an intermediate structure between B and C may exist, where the contact and second layers behave as quasi-2D hexagonal crystals with defects and the third and innermost layers exhibit intermediate features (similar to phase C for $D^* = 9.7$, Figure 2.6). Nevertheless, it was difficult to observe such a structure since finite size effects are very important, especially for the third layer where correlations were measured up to distances of only $3.5\sigma_{ff}$. The differences between the quasi-2D isotropic liquid, intermediate phases and hexagonal crystals for the third layer are very subtle; this is especially true for $270 \text{ K} < T < 280 \text{ K}$, where the differences in $g_j(r)$ and $G_{6,j}(r)$ are not large enough to precisely determine the transition points and unambiguously determine the nature of such phases. In a similar way, structure A for $D^* = 5.5$ (contact and second layers as quasi-2D liquids, innermost layer with low local density) was observed around 318 K. Structure B (intermediate phases for contact and second layers, ρ_{inner}^* starts to increase steeply) is observed at approximately 305 K, and at 290 K structure C (contact and second layers as quasi-2D hexagonal crystals with defects, ρ_{inner}^* exhibiting high values) is obtained. Again, further temperature reduction causes packing changes in the adsorbate layers, especially in the second molecular layer. The rate of increase of $\Phi_{6,j}$ and ρ_{inner}^* upon reduction of temperature is more gradual for $D^* = 5.5$, as compared to what is observed for $D^* = 7.5$. The temperature ranges at which each structure was observed for both $D^* = 7.5$ and 5.5, as obtained from PT-GCMC simulations, are summarized in Table 3.1.

Table 3.1. Temperature range of each structure for LJ CCl₄ confined within MWCNT with $D^* = 7.5$ and 5.5 , as determined from PT-GCMC simulations. See text for descriptions of the different structures.

Structure	$D^* = 7.5$	Structure	$D^* = 5.5$
	Temperature range (K)		Temperature range (K)
A	$T \gtrsim 282$	A	$T \gtrsim 318$
B (*)	$270 \lesssim T \lesssim 282$	B	$295 \lesssim T \lesssim 318$
C	$T \lesssim 270$	C	$T \lesssim 295$

(*) For $D^* = 7.5$, an intermediate structure between B and C may exist, where the contact and second layers behave as quasi-2D hexagonal crystals with defects, and the third and innermost layer exhibit intermediate features. See text for further details.

In Figure 3.6 we show the 3D positional pair correlation function $g(R)$ for the whole adsorbate within the three pore diameters studied at different temperatures, corrected by excluded volume effects [6-8]. Correlations were measured in this case up to $30\sigma_{ff}$ (half of the total pore length). This function is of particular importance since its Fourier transform can be directly compared with the structure factor measured from scattering experiments. For $D^* = 7.5$, solid-like features in $g(R)$ start to arise at temperatures as high as $T = 280$ K; such features reflect the solidification of the contact and second layers [see Figure 3.5 (a)]. As the temperature is reduced, the first minimum of $g(R)$ slightly decreases, the splitting in the second peak becomes more evident, and the maximum in all the peaks of $g(R)$ slightly increase. Similar findings were obtained for $D^* = 5.5$, with the solid-like features appearing at $T = 305$ K. The features observed in $g(R)$ for the whole pore arise since the adsorbate solidifies into different structures in radial and axial directions: molecules form concentric layers in the radial direction, and within each layer, the particles arrange themselves into quasi-2D hexagonal crystals with defects. For distances less than the pore diameter [$R/\sigma_{ff} < 7.5$, Figure 3.6 (a); and $R/\sigma_{ff} < 5.5$, Figure 3.6 (c)], $g(R)$ for the whole pore includes characteristics from both structures (in radial and axial directions), and for larger distances the $g(R)$

features mainly reflect the quasi-2D hexagonal crystal morphology. In addition, the features of $g(R)$ for the whole pore indirectly reflect the fact that the different layers of adsorbate solidify at different temperatures, as observed for $D^* = 9.7$ (Figure 2.9).

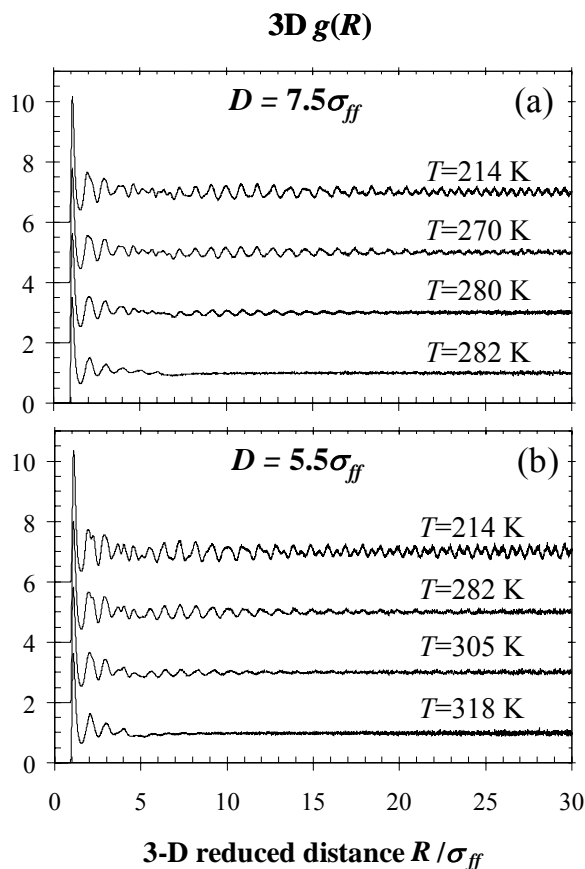


Figure 3.6. 3D positional correlation function $g(R)$, corrected by excluded volume effects, for the all molecules of LJ CCl_4 confined within structureless MWCNT: (a) $D^* = 7.5$, and (b) $D^* = 5.5$, at different temperatures.

3.4.1. Comparison with simulation results, MWCNT with $D^* = 9.7$ ($D = 5 \text{ nm}$)

We note that the freezing behavior of the contact and second layers of LJ CCl_4 is similar for the three pore diameters studied [Figures 2.5, 3.5 (a) and 3.5 (b)]; in

each case they solidify at the same temperature, above the bulk freezing point (251 K for LJ CCl₄). As the pore diameter is reduced, the shift in freezing temperature in these two layers increases: solidification occurs around 305-310 K for $D^* = 5.5$, between 276 and 284 K for $D^* = 7.5$, and at 250-260 K for $D^* = 9.7$. This effect of the pore size has been observed in previous studies [9-12] of strongly attractive pores with cylindrical geometry, and has been explained as follows: the adsorbate-wall attractive interaction becomes stronger as the pore diameter is reduced, leading to larger increases in the solidification temperatures of the molecular layers close to the walls. Similarly, the third molecular layer for $D^* = 7.5$ and $D^* = 9.7$ experiences a more gradual solidification process with temperature, which involves temperatures above the bulk freezing point ($268 \text{ K} < T < 284 \text{ K}$) for $D^* = 7.5$; in contrast, for $D^* = 9.7$ solidification of the third layer involves a much wider range of temperatures ($220 \text{ K} < T < 260 \text{ K}$), above and below the bulk freezing point.

Although the contact and second layers solidify simultaneously for all the pore sizes studied in this work, the average order parameter of the second layer is always higher than that of the contact layer at the lowest temperatures. This effect occurs due to packing considerations: for the three pore sizes, the dimensions of the unfolded second layer [$2\pi r_l \times L$, where r_l is the radial position where the reduced local density ρ^* reaches a maximum in layer l , see Figures 2.2 and 3.1] are commensurate with an integer number of molecules arranged in hexagonal symmetry, but this is not the case for the contact layer. As a result, molecules in the second layer can pack more efficiently than those in the contact layer, making the average order parameter and the in-plane density larger for the second layer. This finding is in agreement with the GCMC results of Kanda and coworkers [10], who obtained a higher in-plane density for the second layer of adsorbate as compared to that of the contact layer. This effect is dependent on pore size: a small

change in this variable can lead to a more efficient packing in the contact layer. Such an effect, which was not observed in slit pores [13-15], emphasizes the role of geometric constraints in pores of cylindrical geometry. It is important to note again that transitions can be observed in the narrow inner regions of adsorbate within the MWCNT with $D^* = 7.5$ and 5.5 , since particles do not form a truly 1D system (for which phase transitions are not possible for $T > 0$ K).

All layers/regions of LJ CCl_4 confined within the model carbon nanotubes studied in this work were able to experience morphology changes upon reduction of temperature, including the highly constrained molecules in the center of the pores. This behavior is in agreement with previous results obtained for strongly attractive cylindrical pores [9-12]. On the other hand, these findings for strongly attractive pores contrast with previous results obtained by Sliwinska-Bartkowiak *et al.* [16] for weakly attractive silica pores. The authors reported amorphous phases for pore sizes with $D < 15\sigma_{ff}$, with the contact layer exhibiting remnants of hexatic behavior without crystallization, even at very low temperatures. These differences suggest that the strength of the adsorbate-wall interaction can produce both shifts in the confined transition temperatures and changes in the adsorbate structure upon reduction of temperature.

3.4.2. Comparison with experimental results

Our DRS results for CCl_4 inside MWCNT with $D = 4.0$ nm and $D = 2.8$ nm (Section 3.3) are in qualitative agreement with our molecular simulation results for LJ CCl_4 within model MWCNT with similar diameters, $D = 3.9$ nm and $D = 2.8$ nm (Section 3.4). For both of these model systems, parallel tempering simulations in the grand canonical ensemble show that all regions of adsorbate experience a sharp change in their local degree of crystallinity simultaneously as T is varied

(Section 3.4). This is consistent with what was observed in our DRS experiments, where only one transition was observed for confined CCl_4 for both pore diameters. The simulations suggest that the melting process take place in the temperature range 270-282 K ($D = 3.9$ nm) and 295-318 K ($D = 2.8$ nm), a somewhat reduced temperature range when compared to that observed for LJ CCl_4 freezing within a MWCNT of $D = 5.0$ nm (190-260 K, Section 2.4). In our DRS measurements, we note that the melting process upon confinement could have started at temperatures lower than $T \sim 272$ K ($D = 4.0$ nm) and $T \sim 287$ K ($D = 2.8$ nm), since the C vs. T curves exhibit changes of slope at temperatures lower than those (starting at $T \sim 265$ K for $D = 4.0$ nm, Figure 3.2, and $T \sim 281$ K for $D = 2.8$ nm, Figure 3.3). Our previous DRS results for CCl_4 within MWCNT with $D = 5.0$ nm (Section 2.3) suggest that melting upon confinement takes place in the temperature range 205-259 K. The simulations overestimate the range of temperatures in which melting upon confinement occurs, with the discrepancy becoming larger as the pore diameter is reduced. This suggests that the potential adsorbate-wall used in our simulations [17] is an accurate representation of the real adsorbate-wall interaction for the case of $D = 5.0$ nm, but becomes somewhat too attractive for smaller pore diameters since the adsorbate-wall attractive interaction becomes stronger as the pore diameter is reduced. Nevertheless, the simulations show that all regions of adsorbate freeze simultaneously at the same temperature, and freezing occurs at higher temperatures upon reduction of the pore diameter, in qualitative agreement with our experimental results.

3.5. Conclusions

We have presented dielectric relaxation spectroscopy measurements of the melting points of carbon tetrachloride within open-tip multi-walled carbon nanotubes with

two different pore diameters, 4.0 and 2.8 nm. In both cases, we have observed one transition corresponding to melting of the confined adsorbate, at temperatures well above the bulk freezing point of CCl_4 ($T \sim 272$ K for $D = 4.0$ nm, and $T \sim 287$ K for $D = 2.8$ nm). These results contrast with our previous DRS measurements for carbon nanotubes with a pore diameter of 5.0 nm (Section 2.3), where multiple transition temperatures both above and below the bulk melting point of CCl_4 were observed. Our results show that the melting temperatures of CCl_4 confined in MWCNT increase as the pore diameter decreases, in contrast to what was observed for adsorbates confined within weakly attractive, siliceous cylindrical pores. These results are in agreement with previous experimental studies in strongly attractive slit pores where the pore width was varied [4,5]. Our DRS measurements also agree with molecular simulation results of freezing of fluids within strongly attractive cylindrical pores [9-12].

We also have reported simulation results for freezing and melting of LJ CCl_4 confined within model MWCNT of similar diameters, 3.9 and 2.8 nm. As for the case of $D = 5.0$ nm (Section 2.4), the simulations show that the adsorbate forms concentric molecular layers that solidify into quasi-2D hexagonal crystals with defects. Freezing in such concentric layers occur via intermediate phases that show remnants of hexatic behavior, in a similar way to the freezing mechanism previously described for Lennard-Jones particles confined within slit pores [15]. For $D = 3.9$ and 2.8 nm, the transitions in these layers occur at temperatures that are above the bulk freezing point, in contrast to what was observed for $D = 5$ nm (Section 2.4), where the layers close to the pore walls and in the central regions of the pore freeze at temperatures above or below the bulk freezing point, respectively. Due to strong geometrical constraints, the adsorbate in the inner regions of the pore forms a highly localized row of particles at the center of the pore, exhibiting increases in the local density ρ_{inner}^* at temperatures above the bulk

freezing point ($D^* = 7.5$ and 5.5). The simulations show evidence of a rich phase behavior in confinement. Three different structures were found for the other two pore sizes examined ($D^* = 7.5$ and 5.5). Some of these phases were found to be inhomogeneous (i.e. combinations of crystalline, liquid and frustrated crystalline regions) and stable over extended temperature ranges. A comparison between the experimental and simulation results reported in this chapter shows that the simulations overestimate the temperatures in which melting in confinement occurs, with the discrepancy becoming larger as the pore diameter is reduced. This suggests that the potential adsorbate-wall used in the simulations [17] is somewhat too attractive for $D < 3.9$ nm. Nevertheless, the simulations show that all regions of adsorbate freeze simultaneously at the same temperature, and freezing occurs at higher temperatures upon reduction of the pore diameter, in qualitative agreement with our experimental results.

Further experiments with different techniques are needed to corroborate our observations. Differential scanning calorimetry experiments should corroborate the measured transition temperatures, while techniques such as x-ray diffraction and neutron scattering are suitable to determine the structure of the adsorbed phase. From the simulation viewpoint, our future work will focus on how freezing in confinement is affected by the pore shape, surface roughness, chemical heterogeneity and morphological defects, in addition to the ratio of the pore-adsorbate to the adsorbate-adsorbate interactions [18,19]. It would also be interesting to determine the effect of bulk pressure on freezing in cylindrical pores, which has been studied in the past for slit pores [20,21] In addition, it will be of interest to study the possibility of solid-solid transformations within each layer of adsorbate upon changes on the diameter of the cylindrical pore, in direct analogy with previous studies in slit pore geometries [22-25].

3.6. References

- [1] F. R. Hung, B. Coasne, K. E. Gubbins, E. E. Santiso, F. R. Siperstein and M. Sliwinska-Bartkowiak, *J. Chem. Phys.* **122**, 144706 (2005).
- [2] M. Jazdzewska, F. R. Hung, K. E. Gubbins and M. Sliwinska-Bartkowiak, *Phys. Chem. Chem. Phys.*, submitted (2005).
- [3] E. S. Domalski and E. D. Hearing, in *NIST Chemistry WebBook, NIST Standard Reference Database Number 69*, ed. P. J. Linstrom and W. G. Mallard, National Institute of Standards and Technology, Gaithersburg, Maryland, 2003 (<http://webbook.nist.gov>).
- [4] J. Klein and E. Kumacheva, *Science* **269**, 816 (1995); *J. Chem. Phys.* **108**, 6996 (1998).
- [5] M. Miyahara, M. Sakamoto, H. Kanda and K. Higashitani, *Stud. Surf. Sci. Catal.*, 2002, **144**, 411.
- [6] A. K. Soper, F. Bruni and M. A. Ricci, *J. Chem. Phys.* **109**, 1486 (1998); A. K. Soper, *J. Phys.: Condens. Matter* **9**, 2399 (1997).
- [7] D. Morineau and C. Alba-Simionesco, *J. Chem. Phys.* **118**, 9389 (2003)
- [8] P. Gallo, M. A. Ricci, and M. Rovere, *J. Chem. Phys.* **116**, 342 (2002)
- [9] M. Maddox and K. E. Gubbins, *J. Chem. Phys.* **107**, 9659 (1997).
- [10] H. Kanda, M. Miyahara, and K. Higashitani, *Langmuir* **16**, 8529 (2000).
- [11] J. Hoffmann and P. Nielaba, *Phys. Rev. E* **67**, 036115 (2003).
- [12] S. Arcidiacono, J. H. Walther, D. Poulikakos, D. Passerone and P. Koumoutsakos, *Phys. Rev. Lett.* **94**, 105502 (2005).
- [13] M. Miyahara and K. E. Gubbins, *J. Chem. Phys.* **106**, 2865 (1997).
- [14] R. Radhakrishnan and K. E. Gubbins, *Mol. Phys.* **96**, 1249 (1999).
- [15] R. Radhakrishnan, K. E. Gubbins, and M. Sliwinska-Bartkowiak, *J. Chem. Phys.* **116**, 1147 (2002).
- [16] M. Sliwinska-Bartkowiak, G. Dudziak, R. Sikorski, R. Gras, R. Radhakrishnan, and K. E. Gubbins, *J. Chem. Phys.* **114**, 950 (2001).
- [17] B. K. Peterson, J. P. R. B. Walton, and K. E. Gubbins, *J. Chem. Soc., Faraday Trans. 2* **82**, 1789 (1986).
- [18] F. R. Hung, B. Coasne, K. E. Gubbins, F. R. Siperstein and M. Sliwinska-Bartkowiak, *Stud. Surf. Sci. Catal.*, accepted (2005).
- [19] F. R. Hung, B. Coasne, M. Sliwinska-Bartkowiak and K. E. Gubbins, *Phys. Rev. B*, to be submitted (2005).
- [20] M. Miyahara, H. Kanda, M. Shibao and K. Higashitani, *J. Chem. Phys.* **112**, 9909 (2000).
- [21] H. Kanda, M. Miyahara and K. Higashitani, *J. Chem. Phys.* **120**, 6173 (2004).
- [22] C. Ghatak and K. G. Ayappa, *Phys. Rev. E* **64**, 051507 (2001); K. G. Ayappa and C. Ghatak, *J. Chem. Phys.* **117**, 5373 (2002).
- [23] A. Vishnyakov and A. V. Neimark, *J. Chem. Phys.* **118**, 7585 (2003).

-
- [24] A. Patrykiewicz, L. Salamacha, and S. Sokołowski, *J. Chem. Phys.* **118**, 1891 (2003).
- [25] H. Bock, K. E. Gubbins and K. G. Ayappa, *J. Chem. Phys.* **122**, 094709 (2005).

Chapter 4

Capillary Condensation of Krypton within Realistic Models of Templated Mesoporous Silica Materials

Templated mesoporous silica material MCM-41 [1] consists of hexagonal arrays of cylindrical pores with diameters between 1.5 and 20 nm, narrow pore size distributions and negligible pore networking. These properties make these materials ideal for fundamental studies aimed at determining the effect of surface forces, confinement and reduced dimensionality on the phase behavior of host molecules. The features of MCM-41 materials [2] make them suitable for a number of applications in catalysis, adsorption, optics, as low dielectric constant materials to insulate integrated circuits, and as host materials for polymers, nanoparticles and enzymes [2].

The gas-liquid transition of adsorbates in templated mesoporous silica materials has been extensively studied by experiment, theory and molecular simulation [3]. From a molecular simulation viewpoint, a number of silica pore models have been used recently [4-7] to study adsorption of different pure substances and mixtures on MCM-41 type materials. Most of these pore models exhibit a regular cylindrical geometry, but it is unclear whether those models are realistic representations of MCM-41, due to the lack of conclusive experiments regarding its pore surface roughness and morphology. Some experimental results [8,9] attribute some surface roughness to the pore walls, whereas others [10,11] suggest a smooth surface at molecular scales (3-7 Å) with roughness and other morphological defects (constrictions, tortuosity) at larger length scales (20-50 Å). One possible approach to model porous solids is to mimic the synthesis process of the real material using simulations, a strategy used in the past [12] to develop realistic models for Vycor

and controlled pore glasses (CPG). Recently, Siperstein and Gubbins [13] used lattice Monte Carlo simulations to study the behavior of surfactant-inorganic oxide-solvent systems and mimic the synthesis of templated mesoporous silica materials. Low values of the surfactant/inorganic oxide concentration ratio led to formation of hexagonally ordered porous structures that resemble that of MCM-41 material. Pores with an important degree of surface roughness and structural defects were obtained from this mesoscale simulation protocol.

In this work we report the preparation of an atomistic silica mesopore model that keep the morphological features of the MCM-41 lattice model developed by Siperstein and Gubbins [13]. The porous material is generated by carving out of a silica block, the skeleton of the MCM-41 pore that was obtained from lattice Monte Carlo simulations. In doing this “downscaling” process, atomic details can be included, more accurate potentials can be used for the adsorbate-wall interactions, and the effect of structural defects on the adsorbate phase behavior can be assessed. Three pore models with similar pore diameters were considered in this study: 1) a pore that keeps the morphological features of the mesoscale model of Siperstein and Gubbins; 2) a pore with regular cylindrical shape; and 3) a cylindrical pore with constrictions. We performed Grand Canonical Monte Carlo (GCMC) simulations of krypton adsorption at 100 K and 87 K, for which we report adsorption isotherms and isosteric heats of adsorption. We discuss the effect of surface roughness and structural defects, and we compare with experimental results available in the literature. Kr adsorption at low temperatures (77, 87 K) has been used in the past for characterization of porous materials with very low surface areas and volumes [14,15]. Comparison with adsorption and neutron scattering experiments suggests that our realistic model of MCM-41 pores is too rough at the molecular scale, but reproduces reasonably the surface disorder of real MCM-41 at larger length scales. Results presented in this chapter have been published

elsewhere [16,17]. Similar results for argon and xenon adsorption on atomistic silica mesopores have been presented in other publications [16,18].

The rest of this chapter is organized as follows. In Section 4.1 we describe the numerical method used to generate the atomistic silica MCM-41 pores used in this study. Our simulation results are presented and discussed in Section 4.2, and we present our concluding remarks in Section 4.3.

4.1. Simulation Details

4.1.1. Preparation of atomistic silica mesopore models

The mimetic simulation procedure to obtain mesoscale, lattice models of MCM-41 type materials has been described in detail in previous publications [13]. The lattice positions of the inorganic oxide segments from the mimetic simulations were scaled to obtain a material with an average pore diameter $D = 6.4$ nm and a length $L = 28$ nm [13]. Our atomistic pores were generated using the method originally proposed by Pellenq and Levitz [19] to model Vycor glass; Coasne *et al.* [5,7] showed that this technique can be used to prepare pores of various morphologies and/or topologies, such as cylindrical, hexagonal, ellipsoidal and constricted pores. We isolated one of the pores obtained from lattice Monte Carlo simulations [13] and carved out its morphology from an atomistic box with $19 \times 19 \times 39$ unit cells of non-porous cristoballite, corresponding to a simulation box of $13.5 \text{ nm} \times 13.5 \text{ nm} \times 27.8 \text{ nm}$. Following that, silicon atoms that are in an incomplete tetrahedral environment are removed, as well as oxygen atoms with two dangling bonds. This procedure ensures that all silicon atoms have no dangling bonds, all oxygen atoms have at least one saturated bond with a silicon atom, and

the pore surface is modeled in a realistic way. To ensure that the atomistic simulation box has no net electrical charge, oxygen atoms with one dangling bond are saturated with hydrogen atoms; these are placed perpendicularly to the pore surface (in the pore void), at a distance of 1 Å from the closest unsaturated oxygen atom. It has been shown [19] that the density of OH group obtained using such a procedure is close to that obtained experimentally for porous silica glasses (7-8 OH per nm²) [20].

To mimic an amorphous silica surface we followed Pellenq and Levitz [19], and in a first step we slightly displaced all the O, Si and H atoms a random distance. In a final step, the porous structure was further relaxed by performing a *NVT* Monte Carlo simulation. The interactions between atoms *i* and *j* separated by a distance *r_{ij}* were calculated using two-body potentials of the BKS type [21]:

$$U_{ij} = \frac{q_i q_j}{r_{ij}} + A_{ij} \exp\left(-\frac{r_{ij}}{\rho_{ij}}\right) - \frac{f_{6,ij}(r_{ij}) C_{6,ij}}{r_{ij}^6} \quad (4.1)$$

The three terms included in the potential function given by equation (4.1) represent the coulomb interaction, the short-range repulsion and the dispersion interaction, respectively. The first of these energy terms was computed without the use of Ewald summation; Puibasset and Pellenq [22] have shown that the correction due to the long-range contribution is very small for a large simulation box (we note that our box size is larger than that in Ref. [22]). The $f_{6,ij}(r_{ij})$ term in the dispersive interaction of equation (4.1) is a damping function that avoids the divergence of the dispersive energy when *r_{ij}* tends to 0. This divergence comes from the mathematical expansion in powers of $1/r_{ij}^{2n}$, which becomes non-valid for small distances *r_{ij}* [23]. The function $f_{6,ij}(r_{ij})$ has the following form:

$$f_{\delta,ij}(r_{ij}) = 1 - \sum_{k=0}^6 \frac{(r_{ij}/\rho_{ij})^k}{k!} \exp\left(-\frac{r_{ij}}{\rho_{ij}}\right) \quad (4.2)$$

where ρ_{ij} is characteristic of the overlap at short distances of the wavefunctions of the two interacting atoms [see equation (4.1)]. The damping function in equation (4.2) varies steeply from 0 up to 1 as the distance r_{ij} between the two atoms increases. In our canonical MC simulations for the pore relaxation process, all interactions were determined using equation (4.1), except the interaction between H and O atoms forming a hydroxyl group that was modeled using a Morse potential [24,25]:

$$U_{ij} = D \{1 - \exp[-\alpha(r_{ij} - r_0)]\}^2 - D \quad (4.3)$$

The values of parameters for equations (4.1) and (4.3), as well as the partial charges used in the canonical MC simulation of the relaxation process are reported in Table 4.1. In order to accelerate the canonical MC simulation run, only atoms located at a distance smaller than 15 Å from the H atoms at the pore surface were allowed to move. The canonical Monte Carlo simulations were performed at a temperature of $T = 2500$ °C, which is in the same order of magnitude of temperatures used in previous simulations of amorphous silica [26]. The maximum displacement allowed for the particle moves was initially set to $\delta = 0.5$ Å. This rather large step in particle displacement allows checking for the stability of the porous structure by sampling configurations where chemical bonds are broken (the equilibrium distances of the OH and SiO bonds are 0.9 Å and 1.7 Å, respectively). Afterwards, we refined the equilibration process by gradually reducing the parameter δ down to 0.05 Å.

Table 4.1. Potential parameters used for the canonical Monte Carlo simulation of the surface relaxation of the MCM-41 silica pore. Oxygen atoms forming an OH bond at the pore surface and oxygen atoms in bulk region have the same properties in this model. All interactions were determined using two-body potentials of the BKS type [21], except the interaction between H and O atoms forming a hydroxyl group, which was modeled using a Morse potential [24,25]. Note that the following interactions are purely coulombic: Si/Si, Si/H and H/H. This set of parameters is taken from Refs. [21] and [24].

Partial charges			
Si	+2.4		
H	+0.6		
O (SiO group)	-1.2		
O (OH group)	-1.2		
Equations (4.1), (4.2)	A (eV)	ρ (Å)	C (eV Å⁶)
Si ^{2.4+} - O ^{1.2-} [21]	18003.7572	0.20520	133.5381
O ^{1.2-} - O ^{1.2-} [21]	1388.7730	0.36232	175.0000
H ^{0.6+} - O ^{1.2-} [24]	311.97000	0.25000	0.000000
Morse potential	D (eV)	ρ (Å⁻¹)	r_0 (Å)
H ^{0.6+} - O ^{1.2-} [24]	7.05250	3.17490	0.94285

The atomistic silica mesopore generated with such a procedure (termed model A, see Figure 4.1) has an average pore radius of 3.2 nm with a dispersion of ± 1 nm. This average pore size was estimated as the distribution of the distances between hydrogen atoms at the pore surface and the center of the pore; the latter was estimated as the center of mass of the distribution of hydrogen atoms. This pore size distribution is shown in Figure 4.2. In order to characterize the surface roughness, we also calculated the average pore radius as a function of the position on the pore axis z (see Figure 4.2). It was found that the average pore dispersion along the pore axis is about ± 0.5 nm. For checking purposes, we isolated a second pore from the mesoscale, lattice Monte Carlo simulations [13], and followed the same procedure to prepare a second atomistic porous sample. The two atomistic pore models were found to have very similar pore size distributions and surface roughness (Figure 4.2). Consequently, the pore model shown in Figure 4.1 was considered representative of the porous solid. We used a similar simulation

protocol to generate two additional silica pores: a regular cylindrical pore with $D = 6.4$ nm (model B, see Figure 4.1), and a cylindrical pore of diameter $D = 8.2$ nm with a constriction of $D = 4.1$ nm (model C, see Figure 4.1). Similar constricted pores were considered in previous simulation studies [5,7,27,28]. The dimensions of pore model C are such that model B is an equivalent regular cylindrical pore with the same length, volume, and on average, the same degree of confinement. Both pore models B and C have a length of 15 nm, and periodic boundary conditions were applied in the axial direction for all three pore models.

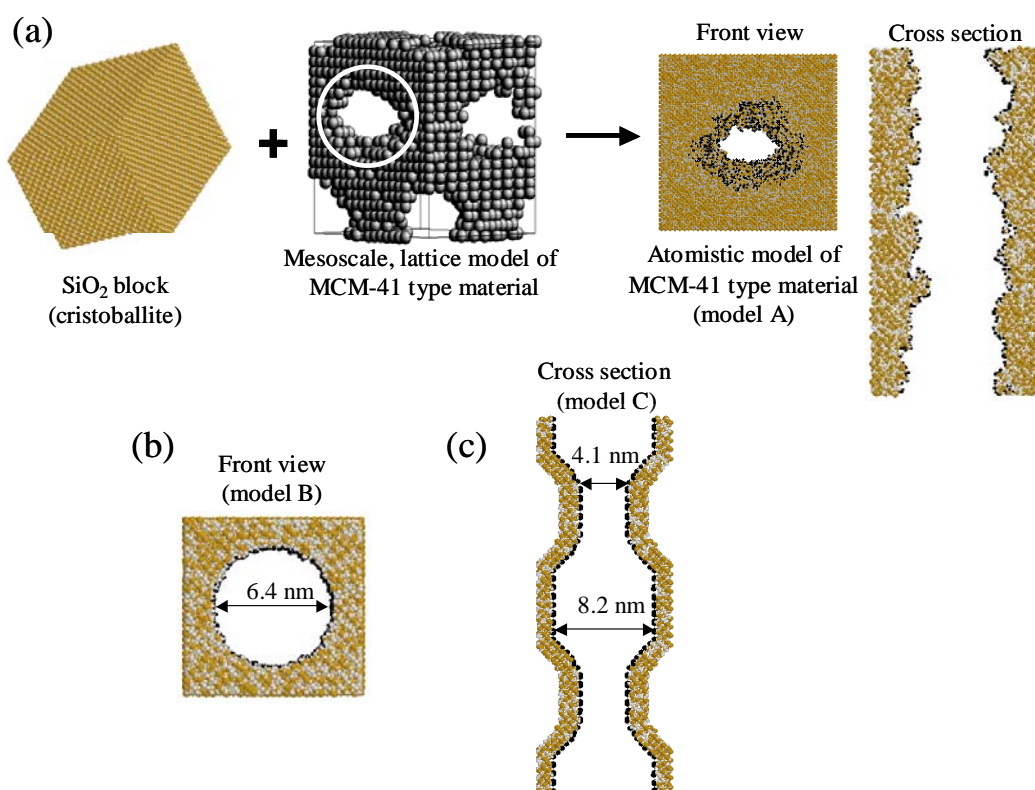


Figure 4.1. Scheme of the procedure used to generate atomistic silica pore models used in this study. Front views and/or cross sections of the three pore models are also shown. Oxygen, silicon and hydrogen atoms are depicted in white, tan and black, respectively. For model C, we have represented two simulation boxes aligned in the axial direction z .

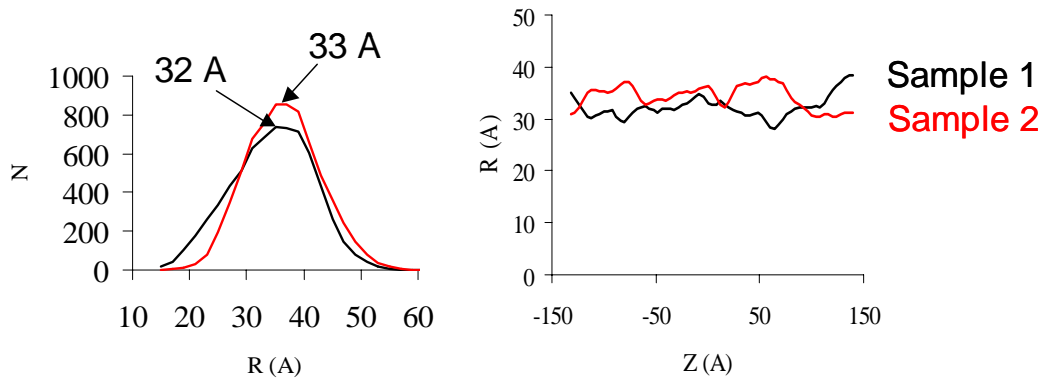


Figure 4.2. Left: pore size distribution R for model A, estimated from the distance between hydrogen atoms at the pore surface and the pore center. Right: average pore size $R(z)$ as a function of the position on the pore axis z for model A. $R(z)$ was estimated from the average distance to the pore center of hydrogen atoms located at a position z . In both figures, the black and red lines corresponds to samples 1 and 2 (see text).

Small angle neutron scattering spectra (SANS) were calculated for each numerical porous material considered in this work, following the work by Pellenq and Levitz [19]. Such spectra $I(Q)$ provide information regarding the surface properties of the material in the Porod range, i.e. $QD > 1$, where D is the size of the pore [29]. SANS spectra are shown in Figure 4.3 for pore models A and B. Calculations were corrected for the non-physical periodicity introduced by the finite size of the porous samples. Peaks obtained at large momentum transfer ($Q > 1 \text{ \AA}^{-1}$) are in very good agreement with experimental x-ray data for the structure of cristoballite: 1.52, 2.49, 2.90, 3.03, 3.83 and 4.55 \AA^{-1} . Spectra were fitted using an algebraic decay law $I(Q) = Q^{-x}$ over the range $0.05\text{-}0.55 \text{ \AA}^{-1}$, in order to determine the Porod exponent x that characterizes the surface roughness of the porous solids at length scales between 10 \AA and 50 \AA .

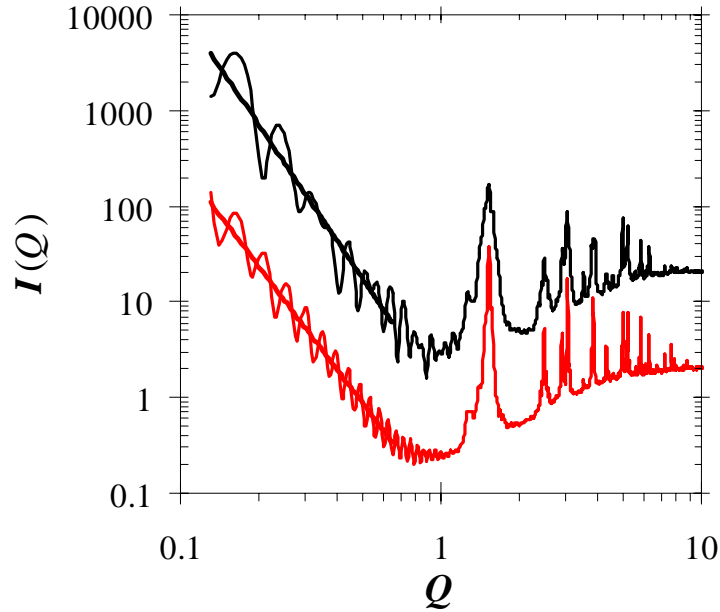


Figure 4.3. Small angle neutron scattering spectra for pore model A (red line) and pore model B (black line). The Bragg peaks of cubic cristobalite are in very good agreement with the experimental x-ray peaks: 1.52, 2.49, 2.90, 3.03, 3.83 and 4.55 \AA^{-1} . The two straight lines correspond to an algebraic decay over the range 0.05-0.55 \AA^{-1} with the exponent 3.6 for model A and 4.0 for model B (see text).

For pore model B (regular cylindrical pore), we obtained that $x = 4.0 \pm 0.1$, as expected for a cylindrical pore having a smooth pore/void interface with only atomistic surface roughness. In contrast, for pore model A we obtained $x = 3.6 \pm 0.1$, which is close to the value found for disordered porous silica samples such as Vycor [30,31] or silica gel [11,32]. Such a value is in good agreement with SAXS and SANS experimental investigations of the surface disorder for MCM-41 materials: Edler *et al.* [10] reported that the Porod exponent x of MCM-41 samples obtained from ordinary preparation methods is comprised between 3 and 3.5. This result was later confirmed by Sonwane *et al.* [11], who showed that x is in the range 3-4 for their MCM-41 samples with different pore sizes.

4.1.2. Kr adsorption

Krypton was modeled as a Lennard-Jones (LJ) fluid with parameters taken from Ref. [19]: $\sigma_{ff} = 0.369$ nm, $\varepsilon_{ff}/k_B = 170$ K. The interaction of Kr atoms with O, Si and H atoms in the substrate was modeled using the PN-TraZ potentials and parameters, which have been used in the past to model gas adsorption in zeolites [33] and Vycor glass [19]. In this potential, the interaction energy U_i of a rare gas atom i with the substrate is given by:

$$U_i = \sum_{j \in \{O, Si, H\}} \left[A_{ij} e^{-b_{ij} r_{ij}} - \sum_{n=3}^5 f_{2n} \frac{C_{2n,ij}}{r_{ij}^{2n}} \right] - \frac{\alpha_i E_i^2}{2} \quad (4.4)$$

$$f_{2n} = 1 - \sum_{k=0}^{2n} \frac{(b_{ij} r_{ij})^k}{k!} \exp(-b_{ij} r_{ij}) \quad (4.5)$$

where the sum runs over all atoms in the substrate (Si, O and H). The terms in equation (4.4) represent the short-range repulsion, the dispersion interaction and the induction interaction, respectively [19]. The f_{2n} terms represent damping functions similar to those presented previously in equation (4.2). More details about the intermolecular potential functions can be found in the previous work of Pellenq and Levitz [19]. The different parameters for Kr adsorption are summarized in Table 4.2.

Table 4.2. PN-TraZ potential parameters for Kr adsorption in silica pores. Parameters are in atomic units: $E_h = 3.1578 \cdot 10^5$ K, $a_0 = 0.529177$ Å. Taken from Ref. [19]

	Kr-O	Kr-Si	Kr-H
$C_6/E_h a_0^6$	71.36	26.71	19.73
$C_8/E_h a_0^8$	1190.2	399.00	457.5
$C_{10}/E_h a_0^{10}$	41500	-	-
A/E_h	603.8	1206.6	17.78
b/a_0^{-1}	1.907	1.981	1.980
Partial charges			
$q_O = -1e$	$q_{Si} = +2e$	$q_H = +0.5e$	
Polarizabilities			
$\alpha(Kr) = 16.75a_0^3$			

We performed Grand Canonical Monte Carlo (GCMC) [34,35] simulations of Kr adsorption at $T = 100$ K and 87 K. The ideal gas equation and the properties of the LJ fluid at coexistence [36] were used to calculate chemical potentials μ from relative pressures P/P_0 . To speed up our simulation runs, we have used an energy grid [19] with an elementary cube size of about 1 \AA^3 to compute the adsorbate-wall potential energy. An accurate estimation of the energy is then obtained by linearly interpolating between the grid values. Thermodynamic properties were averaged over a minimum of 10^5 MC steps per particle (typical systems had up to $N = 15000$ particles); however, much longer runs were considered near the phase transitions. We also determined the isosteric heat of adsorption q_{st} [35]:

$$q_{st} = q_{st}^{ff} + q_{st}^{fw} = \left[RT - \frac{\langle U_{ff} N \rangle - \langle U_{ff} \rangle \langle N \rangle}{\langle N^2 \rangle - \langle N \rangle^2} \right] + \left[- \frac{\langle U_{fw} N \rangle - \langle U_{fw} \rangle \langle N \rangle}{\langle N^2 \rangle - \langle N \rangle^2} \right] \quad (4.6)$$

where q_{st}^{ff}, q_{st}^{fw} represent the adsorbate-adsorbate and the adsorbate-wall contributions to q_{st} . The quantities in brackets $\langle \dots \rangle$ represent ensemble averages, R is the gas constant, and U_{ff} and U_{fw} represent the adsorbate-adsorbate and adsorbate-wall potential energy. In our GCMC simulations we also measured the local density profile ρ , and the “renormalized” 3D positional pair correlation function $g(R)$ (where R is the in-pore distance) following the procedure reported in Section 2.2.3.

4.2. Results

Kr adsorption isotherms are presented in Figure 4.4 for the three atomistic silica mesopore models. The adsorbed amounts were normalized with respect to the quantity of adsorbate when each pore is filled. At a fixed T , the adsorption curves exhibit different features and are significantly affected by the pore morphology. For pore model B there is one vertical jump due to capillary condensation, whereas two discontinuities were observed for model C. The adsorption isotherm for pore model A also exhibits two small jumps that are not as sharp as those observed in models B and C. The surface area of pore model A is larger than that of model C, which in turn is larger than that of model B. In addition, pore model A exhibits an important degree of surface roughness and therefore there are more sites where molecules can get preferentially adsorbed. These factors cause pore model A to exhibit a lower capillary condensation pressure, a larger value of N/N_0 at any given P/P_0 , and an adsorption curve that looks smoother than those for the other pore models. Pore model C fills at a lower value of P/P_0 than model B, and at a fixed value of P/P_0 , model C exhibits a larger value of N/N_0 than that for model B. Pore model A shows an asymmetrical hysteresis loop, which is typical of adsorption on

materials with interconnected pores, e.g. Vycor [7,12,19], but were also observed in unconnected pores with morphological defects [5,7].

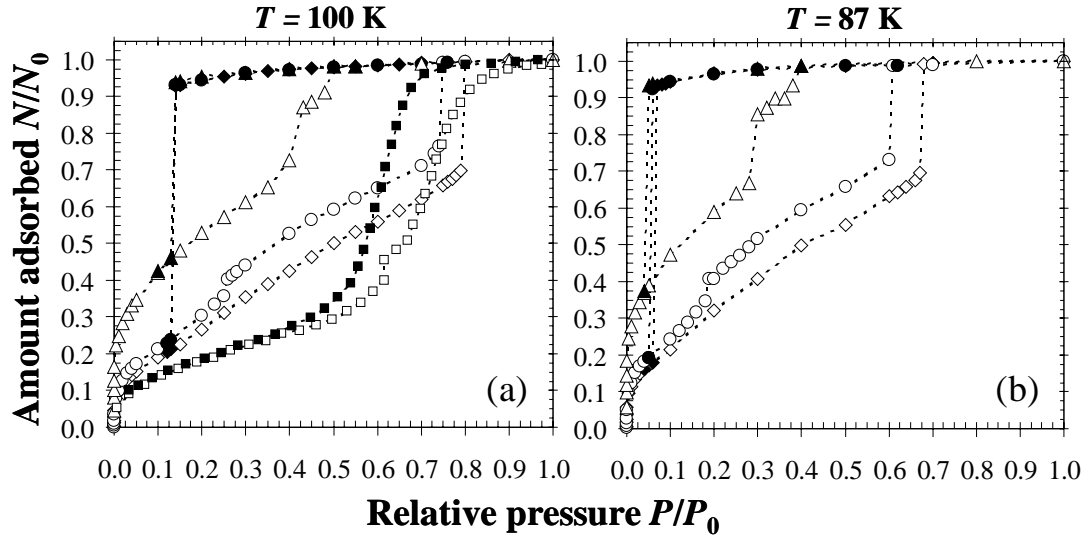


Figure 4.4. Adsorption-desorption isotherms for Kr at (a) $T = 100$ K, and (b) $T = 87$ K. Results for pore models A, B and C are depicted by triangles, diamonds and circles, respectively; squares represent experimental results on SBA-15 with a similar mean pore diameter (6.4 nm) [37]. Open and closed symbols represent adsorption and desorption, respectively.

Evaporation takes place approximately at the same value of P/P_0 in the three pore models. Due to the use of periodic boundary conditions, there is no interface with the bulk and evaporation occurs via nucleation of a gas bubble (cavitation) in the center of the pore. The mean pore sizes in term of Kr molecular diameters ($\sigma_{\text{Kr}} = 0.369$ nm) are such that the desorption process does not seem to be affected by the pore morphology. Our adsorption-desorption simulation study of Ar ($\sigma_{\text{Ar}} = 0.34$ nm) on pore model A [16] shows a desorption curve similar to that of Kr, but for Xe ($\sigma_{\text{Xe}} = 0.410$ nm) it was found that the desorption curve is composed of reversible paths and two small jumps in the adsorbed amount [16,18]. A similar behavior was observed for Ar adsorption on constricted pores with

different dimensions [7,38]. These results suggest that the desorption mechanism in pores with morphological defects strongly depends on pore geometry and adsorbate size. For a given pore model, as temperature increases the amount adsorbed at a certain value of P/P_0 decreases, capillary condensation and evaporation take place at higher values of P/P_0 , the hysteresis loop shrinks, and the jumps in the adsorption isotherms are less marked.

In Figure 4.4 we also compare our simulation results at 100 K with experiments for SBA-15 with the same mean pore diameter (6.4 nm) from Morishige *et al.* [37]. The shape of the experimental adsorption isotherm resembles that of pore model A, and the step due to capillary condensation is steep but not vertical. This can be due to the presence of a pore size distribution, as well as morphological and topological features (microporosity, interconnected pores, changes in pore shape, surface roughness, energetic heterogeneity). On the other hand, the experimental capillary condensation pressure is similar to what was obtained for pore model B, and N/N_0 is overestimated by all pore models. The lack of quantitative agreement between simulations and experiments could be due to at least two reasons. First, the intermolecular potential adsorbate-wall can be overestimating the attractive energy: for simulated Ar adsorption in regular cylindrical silica pores, it has been reported [7] that a reduction of 3% in selected parameters can lead to quantitative agreement in film thickness (t -plot) with experimental results. Second, the degree of surface disorder for pore model A is too high at the molecular level, leading to overestimation of N/N_0 and underestimation of the capillary condensation pressure. These conclusions are corroborated by our results for the isosteric heat of adsorption q_{st} for Kr at 100 K, which are presented in Figure 4.5. The experimental value of q_{st} at low coverages is 15 kJ/mol [19], in agreement with results for pore models B and C. At low pore filling fractions ($N/N_0 < 0.3$), q_{st} for pore model A largely overestimates the values of models B and C [Figure 4.5 (a)], since the

adsorbate-wall contribution to q_{st} for pore model A is significantly larger than those for the other pore models [Figure 4.5 (b)]. This explains why N/N_0 at a given pressure prior to capillary condensation is much larger for pore model A, and suggests that the degree of surface disorder for pore model A is too high at the molecular level. This conclusion is also supported by our results for Ar and Xe adsorption [16,18] and their comparison with available experimental data. Nevertheless, our simulated SANS results for pore model A (Figure 4.3) indicates that its roughness at length scales between 10 Å and 50 Å is in agreement with experimental measurements for real MCM-41 type materials [10,11]. Further improvements in pore model A are required so that its molecular-level roughness is in agreement with experimental results.

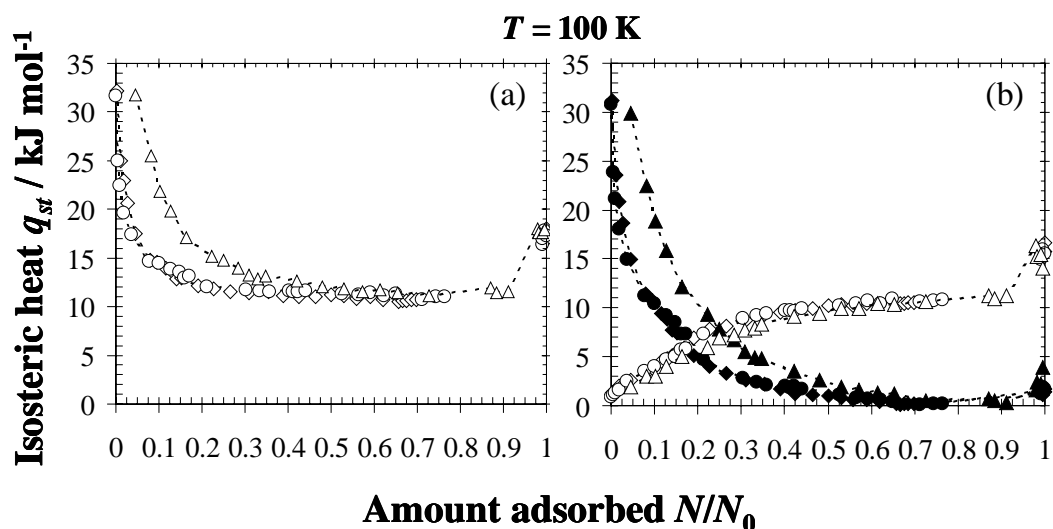


Figure 4.5. Isosteric heat of adsorption q_{st} as a function of coverage fraction N/N_0 , for Kr adsorption on atomistic silica mesopores at 100 K: (a) total q_{st} , and (b) adsorbate-wall (filled symbols) and adsorbate-adsorbate (open symbols) contributions to q_{st} . Symbols as in Figure 4.4.

We have used our pore models to discuss the effect of surface roughness and structural defects on the adsorption mechanism and on the nature of the dense phases. In Figure 4.6 we present plots of the local density profile $\rho(r, z)$, as well as

representative simulation snapshots for the three pore models at different values of P/P_0 and $T = 100$ K. For pore model A, ρ also depends on the angular coordinate θ , nevertheless, a plot of $\rho(r, z)$ can provide a suitable measure of the local state of the confined phase. As P/P_0 increases, the pore walls are covered by an adsorbate film whose thickness increases gradually with P/P_0 , until it reaches a point [$P/P_0 = 0.40$, Figure 4.6 (a)] when there is formation of a condensate “bridge” between low density regions of adsorbate in the center of the pore. Most of the low density regions condense suddenly at $P/P_0 = 0.43$ [Figure 4.6 (a)], which is also signaled by a jump in the adsorption isotherm (Figure 4.4). Finally, at $P/P_0 = 0.50$ the pore is filled with a condensed phase and a smaller jump in the isotherm is also observed (Figure 4.4). A similar behavior has been observed in past studies for adsorbents with distinct chemical and morphological heterogeneities [7,19,27,28,39-41], and is similar to the filling mechanism observed for pore model C [Figure 4.6 (c)]. As P/P_0 increases, we see again an increase in the adsorbed film thickness until it becomes unstable and condensation takes place in the constrictions [$P/P_0 = 0.26$, see Figure 4.6 (c)]. The size of the constriction ($D = 4.1$ nm) is comparable to the diameter at the narrowest part of pore model A ($D = 5.4$ nm), where the liquid-like “bridge” first forms [$P/P_0 = 0.40$, Figure 4.6 (a)]. This leads to the formation of hemispherical gas-liquid interfaces that coexist with condensed regions, as was observed for pore model A. These gas-like regions slightly shrink as P/P_0 increases, until the main cavity is suddenly filled with a condensed phase [Figure 4.6 (c)]. The adsorption isotherm also exhibits two jumps when these condensation processes take place (Figure 4.4). In contrast, for pore model B [Figure 4.6 (b)], the adsorbed film thickness increases with P/P_0 until it reaches its stability limit [$P/P_0 = 0.79$, Figure 4.6 (b)]. A slight increase in P/P_0 makes the pore to be suddenly filled with a condensed phase and a vertical jump is observed in the adsorption isotherm [Figure 4.6 (b) and Figure 4.4].

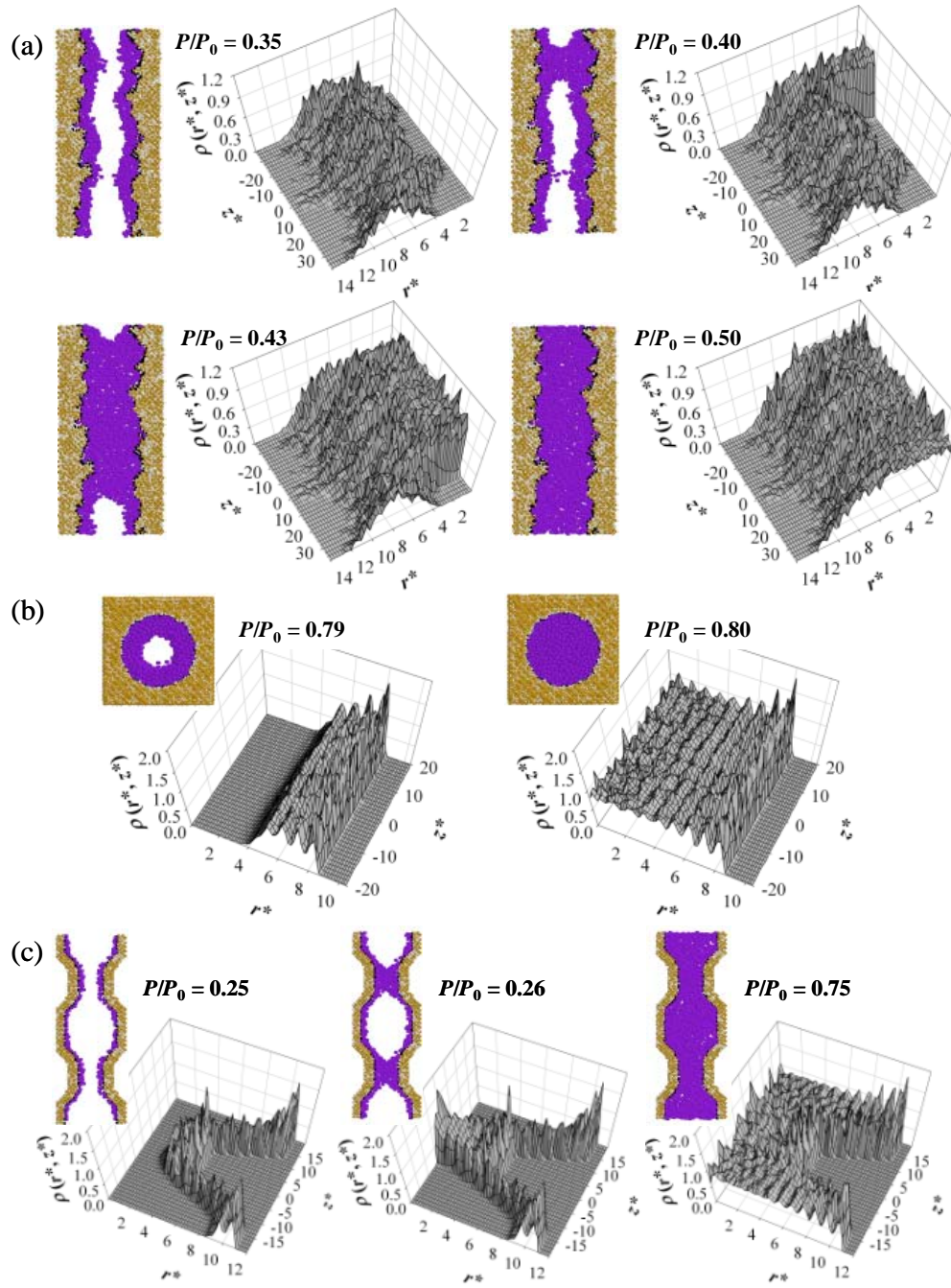


Figure 4.6. Local density profile $\rho(r, z)$, and front views or cross sections of representative simulation snapshots of the confined phase inside (a) pore model A, (b) pore model B, and (c) pore model C, for different values of P/P_0 at $T = 100$ K. Two simulation boxes aligned in the axial direction z are represented in the snapshots for pore model C, to help visualization of the confined phase features.

The adsorption mechanisms at $T = 87$ K for the three pore models are similar to those described at $T = 100$ K. In Figure 4.7 we show the 3D positional pair correlation function $g(R)$ for Kr inside the three pore models at $T = 87$ K and $P/P_0 = 1$. These functions suggest that the three pore models are filled with dense Kr with a liquid-like structure, even though the temperature is well below the bulk triple point (116 K). The maximum in the first peak of $g(R)$ is slightly larger for pore model B as compared to the other models, with Kr inside pore model A exhibiting the lowest value for this first peak. An investigation of the global and local structure of Kr freezing within these pores is currently in progress.

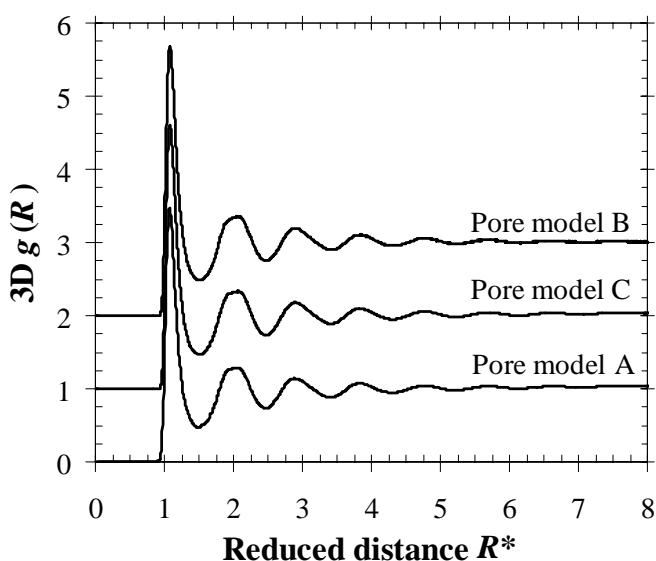


Figure 4.7. 3D positional pair correlation function $g(R)$ for Kr at $T = 87$ K and $P/P_0 = 1$.

4.3. Concluding Remarks

In this work we report the preparation of an atomistic silica mesopore (model A) that keep the morphological features of the MCM-41 lattice model developed by Siperstein and Gubbins [13]. The porous material is generated by carving out of a

silica block, the skeleton of the MCM-41 pore that was obtained from lattice Monte Carlo simulations. In order to discuss the effect of surface roughness and structural defects on krypton adsorption, we prepared two additional silica mesopores, a regular cylindrical pore (model B), and a cylindrical pore with constriction (model C). The three pore models have a similar average pore diameter. Adsorption isotherms, isosteric heats, density profiles and 3D positional pair correlation functions were obtained at $T = 100$ K and 87 K, below the bulk triple point of Kr (116 K), and compared with experimental data. Surface roughness and structural defects significantly affect Kr adsorption: marked differences were observed in the adsorption isotherms, isosteric heat curves and pore filling mechanisms. For instance, the adsorption branch for model A corresponds to a quasi-continuous pore filling involving coexistence of liquid-like “bridges” and gas-like regions, while the discontinuous adsorption branch for model B conforms to the classical picture of capillary condensation in regular nanopores. Adsorption on model C exhibits features from both models A and B, namely a pore filling mechanism with coexistence of hemispherical gas-liquid interfaces and condensed regions, and a discontinuous adsorption curve. It was also found that the features of the adsorption/desorption cycles for model A depend on the adsorbate: a large hysteresis loop with asymmetrical adsorption and desorption branches was observed for Ar [16] and Kr [17], but the adsorption/desorption isotherm for Xe in model A [16,18] was composed of both reversible/continuous and slightly irreversible/discontinuous paths. In contrast, symmetrical hysteresis loops were always obtained for the regular cylindrical nanopore (model B).

Our results suggest that the degree of surface disorder for pore model A is too high at the molecular level; however, simulated SANS spectrum shows that its roughness at larger length scales (10-50 Å) is in agreement with MCM-41

experimental results [10,11]. We are currently trying to improve our pore model so that its molecular roughness agrees with experimental data, by using better relaxation techniques to reconstruct the surface of the pore. This may allow us to obtain porous samples combining the correct atomistic roughness (similar to that for model B) and the correct surface disorder at larger length scales (similar to that for model A). We are also extending our work to develop realistic models [42] of SBA-15 materials, i.e. silica mesopores which are linked through microporous interconnections [43,44]; mesoscale, lattice models of these materials are available [45]. In a future work, we will also investigate freezing of simple adsorbates in these realistic models of mesoporous silica materials. Such a study will allow us to determine whether the disordered pore surface prevents or not crystallization of the confined fluid. Results shown in this chapter suggest that the dense phase of Kr inside the three pore models exhibit a liquid-like global structure. Nevertheless, a detailed investigation of the freezing behavior of Kr within these pores is currently in progress.

4.4. References

-
- [1] C. T. Kresge, M. E. Leonowicz, W. J. Roth, J. C. Vartuli and J. S. Beck, *Nature*, 359 (1992) 710.
 - [2] For recent reviews, see P. Selvam, S. K. Bhatia and C. G. Sonwane, *Ind. Eng. Chem. Res.*, 40 (2001) 3237; G. J. de A. A. Soler-Illia, C. Sanchez, B. Lebeau and J. Patarin, *Chem. Rev.*, 102 (2002) 4093; F. Schüth and W. Schmidt, *Adv. Mater.*, 14 (2002) 629.
 - [3] For a review, see L. D. Gelb, K. E. Gubbins, R. Radhakrishnan and M. Sliwinska-Bartkowiak, *Rep. Prog. Phys.*, 62 (1999) 1573.
 - [4] M. W. Maddox, J. P. Olivier and K. E. Gubbins, *Langmuir*, 13 (1997) 1737.
 - [5] B. Coasne, A. Grosman, C. Ortega and R. J. M. Pellenq, *Stud. Surf. Sci. Catal.*, 144 (2002) 35.
 - [6] Y. He and N. A. Seaton, *Langmuir*, 19 (2003) 10132.
 - [7] B. Coasne and R. J.-M. Pellenq, *J. Chem. Phys.*, 121 (2004) 3767; 120 (2004) 2913.

-
- [8] V. B. Fenelonov, A. Y. Derevyankin, S. D. Kirik, L. A. Solovyov, A. N. Shmakov, J.-L. Bonardet, A. Gedeon and V. N. Romannikov, *Micropor. Mesopor. Mat.*, 44-45 (2001) 33.
- [9] A. Berenguer-Murcia, J. García-Martínez, D. Cazorla-Amorós, A. Martínez-Alonso, J. M. D. Tascón and A. Linares-Solano, *Stud. Surf. Sci. Catal.*, 144 (2002) 83.
- [10] K. J. Edler, P. A. Reynolds and J. W. White, *J. Phys. Chem. B*, 102 (1998) 3676.
- [11] C. G. Sonwane, S. K. Bhatia and N. J. Calos, *Langmuir*, 15 (1999) 4603.
- [12] L. D. Gelb and K. E. Gubbins, *Langmuir*, 14 (1998) 2097; *Mol. Phys.*, 96 (1999) 1795.
- [13] F. R. Siperstein and K. E. Gubbins, *Mol. Sim.*, 27 (2001) 339; *Langmuir*, 19 (2003) 2049.
- [14] S. J. Gregg and K. S. W. Sing, *Adsorption, Surface Area and Porosity*, 2nd edition, Academic Press, London, 1982.
- [15] T. Takei and M. Chikazawa, *J. Ceram. Soc. Jpn.*, 106 (1998) 353.
- [16] B. Coasne, F. R. Hung, R. J.-M. Pellenq, F. R. Siperstein and K. E. Gubbins, *Langmuir*, submitted (2005).
- [17] F. R. Hung, B. Coasne, K. E. Gubbins, F. R. Siperstein, M. Thommes and M. Sliwiska-Bartkowiak, *Stud. Surf. Sci. Catal.*, accepted (2005).
- [18] B. Coasne, F. R. Hung, F. R. Siperstein and K. E. Gubbins, *Ann. Chim-Sci. Mat.*, in press (2005).
- [19] R. J.-M. Pellenq and P. E. Levitz, *Mol. Phys.*, 100 (2002) 2059.
- [20] H. Landmesser, H. Kosslick, W. Storek, and R. Frick, *Solid State Ionics*, 101-103 (1997) 271.
- [21] B. W. H. van Beest, G. J. Kramer and R. A. van Santen, *Phys. Rev. Lett.*, 64 (1990) 1955.
- [22] J. Puibasset and R. J.-M. Pellenq, *Phys. Chem. Chem. Phys.*, 6 (2004) 1933.
- [23] K. T. Tang and J. P. Toennies, *J. Chem. Phys.*, 80 (1984) 3726.
- [24] J. D. Gale, *Philos. Mag. B*, 73 (1996) 3.
- [25] N. H. de Leeuw, F. Manon Higgins and S. C. Parker, *J. Phys. Chem. B*, 103 (1999) 1270.
- [26] K. Binder, *Comp. Phys. Comm.*, 121-122 (1999) 168; and references therein.
- [27] L. Sarkisov and P. A. Monson, *Langmuir*, 17 (2001) 7600.
- [28] A. Vishnyakov and A. V. Neimark, *Langmuir*, 19 (2003) 3240.
- [29] J. D. F. Ramsay, *Adv. Coll. Interface Sci.*, 76-77 (1998) 13.
- [30] P. Levitz, G. Ehret, S. K. Sihna and J. M. Drake, *J. Chem. Phys.*, 95 (1991) 6151.
- [31] A. C. Mitropoulos, J. M. Haynes, R. M. Richardson and N. K. Kanellopoulos, *Phys. Rev. B.*, 52 (1995) 10035.
- [32] J. M. Drake, P. Levitz and J. Klafter, *Israel J. Chem.*, 31 (1991) 135.

-
- [33] R. J.-M. Pellenq and D. Nicholson, *J. Phys. Chem.*, 98 (1994) 13339.
- [34] D. Frenkel and B. Smit, *Understanding Molecular Simulation: from Algorithms to Applications*, 2nd ed., Academic Press, London (2002).
- [35] D. Nicholson and N. G. Parsonage, *Computer Simulation and the Statistical Mechanics of Adsorption*, Academic Press, London (1982).
- [36] R. Agrawal and D. A. Kofke, *Mol. Phys.*, 85 (1995) 43.
- [37] K. Morishige, K. Kawano and T. Hayashigi, *J. Phys. Chem. B.*, 104 (2000) 10298.
- [38] B. Coasne, K. E. Gubbins and R. J.-M. Pellenq, *Part. Part. Syst. Charact.*, 20 (2004) 1.
- [39] H. Bock and M. Schoen, *Phys. Rev. E*, 59 (1999) 4122.
- [40] J. Puibasset, *J. Chem. Phys.*, 122 (2005) 134710.
- [41] F. Detcheverry, E. Kierlik, M. L. Rosinberg, and G. Tarjus, *Phys. Rev. E*, 68 (2003) 061504.
- [42] A preliminary account of this work is presented in S. Bhattacharya, B. Coasne, F. R. Hung and K. E. Gubbins, *Stud. Surf. Sci. Catal.*, accepted (2005).
- [43] D. Zhao, J. Feng, Q. Huo, N. Melosh, G. H. Fredrickson, B. F. Chmelka and G. D. Stucky, *Science*, 279 (1998) 548.
- [44] A. Galarneau, H. Cambon, F. Di Renzo, R. Ryoo, M. Choi and F. Fajula, *New J. Chem.*, 27 (2003) 73.
- [45] S. Bhattacharya and K. E. Gubbins, *J. Chem. Phys.*, accepted (2005).

Chapter 5

Freezing of Krypton within Mesoporous Silica Materials: Effect of Pore Morphology and Surface Roughness

Freezing and melting of fluids confined in nanoporous materials have practical applications in adhesion, lubrication, characterization of porous materials, nanofabrication, etc. A large amount of experimental evidence [1,2] clearly indicates that the phase diagram of a substance can be significantly altered when confined within a porous material. Most of the early experimental studies [1,2] on freezing in confinement have been carried out using a wide variety of adsorbates and different siliceous materials, mainly controlled pore glasses (CPG) and Vycor glass. These materials exhibit a network of interconnected pores with narrow size distributions; although the shape of the pores is roughly cylindrical, they present a variable cross section, curvature and tortuosity [1]. On the other hand, templated mesoporous silica materials MCM-41 [3] and SBA-15 [4] consists of hexagonal arrays of cylindrical pores with diameters between 1.5 and 20 nm, narrow pore size distributions and negligible pore networking, as determined accurately from combined transmission electronic microscopy (TEM), X-ray diffraction and adsorption experiments [5-7]. It has been shown that the cylindrical mesopores in SBA-15 materials are connected through transversal microporous channels [8-10]; on the other hand, it is usually admitted that MCM-41 are made up of unconnected mesopores [9,11]. These properties make these materials ideal for fundamental studies aimed at determining the effect of surface forces, confinement and reduced dimensionality on the phase behavior of host molecules. Moreover, MCM-41 and SBA-15 materials are suitable for a number of applications in catalysis, adsorption, optics, as low dielectric constant materials to insulate integrated circuits, and as host materials for polymers, nanoparticles and enzymes [5-7].

Recent experimental studies of freezing and melting of small, non-polar molecules within templated mesoporous silica materials [1,2,12-19], as well as recent studies using silica porous glasses [1,2,20-24] show evidence of different freezing behaviors for the adsorbate molecules close to the pore wall and those in the center of the pore. The former region (termed “surface-bound” adsorbate) has an estimated thickness of up to four monolayers, and exhibits an amorphous or liquid-like structure due to the proximity to the pore walls. It has been suggested that the surface-bound adsorbate does not experience appreciable changes in structure upon freezing or melting [14,15,17,20,21]. For completely filled pores of relatively large diameters, the adsorbate molecules outside the surface-bound layers freeze into structures that are similar to the corresponding bulk crystal phases, but with a number of defects due to the confined geometry; for molecules having solid-solid phase transitions, some differences have been observed between the bulk and confined behavior [1,2,14,16,17,18]. Amorphous solid phases were always observed for smaller pores [14,15,17,20,21]. Significant hysteresis effects between freezing and melting were also present. For the small, non-polar adsorbate molecules considered in these studies, it was found that the freezing temperature inside the pore was always lower than that for the bulk, with the depression becoming larger as the pore size decreases. The freezing and melting behavior in confinement has been described in terms of macroscopic thermodynamic models such as the Gibbs-Thomson equation [1,2] and its modifications to consider the non-freezing surface-bound adsorbate [1,2,16], as well as other simple phenomenological models [22,25]. However, such macroscopic treatments break down for pores of small sizes, up to a few adsorbate molecular diameters [1,2]. Therefore, molecular simulations are well suited to study such phenomena and help in the analysis of experimental results.

Molecular simulation studies of freezing and melting of Lennard-Jones (LJ) fluids confined in structureless pores of slit-like [26,27] and cylindrical [28-33] geometry, have clearly established that the strength of the adsorbate-pore wall interactions as compared to the adsorbate-adsorbate intermolecular forces, as well as the pore size, determine the freezing temperature in confinement and the structure of the confined phases. Very recently, Nishio *et al.* [34-36] performed Molecular Dynamics (MD) simulations of freezing of LJ argon within a cylindrical pore representing a silica material. Such a nanopore was carved out of a cubic box containing oxygen atoms; the interactions of Ar with Si and H were not considered. Both ends of the cylindrical pore were in contact with gas reservoirs. In these studies, it was found that Ar crystallized for pores with diameter $D \geq 15\sigma_{ff}$ when the cooling rate is lower than a certain critical value; in contrast, for $D = 10\sigma_{ff}$ crystallization was not observed even at very low cooling rates, in agreement with the Grand Canonical Monte Carlo (GCMC) results of Sliwinska *et al.* [29] for structureless silica pores. Solid, amorphous Ar within a pore of $D = 10\sigma_{ff}$ exhibited a local icosahedral symmetry consistent with a glassy morphology [34-36]. Maddox *et al.* [37] have reported that pore models with a homogeneous adsorbate-wall interaction potential fail to reproduce the behavior of N_2 confined within MCM-41 type materials. A number of silica pore models have been used recently [34-44] to study adsorption of different pure substances and mixtures on MCM-41 type materials. Most of these pore models exhibit a regular cylindrical geometry with circular or hexagonal cross sections, but it is unclear whether those models are realistic representations of MCM-41, due to the lack of conclusive experiments regarding its pore surface roughness and morphology. Some experimental results [45,46] attribute some surface roughness to the pore walls, whereas others [47,48] suggest a smooth surface at molecular scales (3-7 Å) with roughness and other morphological defects (constrictions, tortuosity) at larger length scales (20-50 Å).

One possible approach to model porous solids is to mimic the synthesis process of the real material using molecular simulations, a strategy used in the past [49,50] to obtain realistic models for silica glasses. Recently, we developed a fully atomistic model of siliceous MCM-41 materials [51-53], based on the morphological features of a mesoscale model [54,55] obtained from lattice Monte Carlo simulations mimicking the synthesis of MCM-41 materials. In doing this “downscaling” process, atomic details can be included, and more accurate potentials can be used to model the adsorbate-wall interactions. Pores with an important degree of surface roughness and structural defects were obtained from this simulation protocol; therefore, the effect of these variables on the phase behavior in confinement can be assessed. In our previous work [51-53], we have studied adsorption of argon, krypton and xenon on this pore (termed model A) and compared with results obtained for a regular cylindrical pore (model B) and a cylindrical pore with constrictions (model C), all of them with a mean pore diameter of 6.4 nm. It was observed that pore surface roughness and structural defects significantly affect gas adsorption: marked differences were obtained in the adsorption isotherms, isosteric heat curves and pore filling mechanisms. Our previous results for gas adsorption [51-53] indicate that pore model A seems to be too rough at the molecular scale. Nevertheless, simulated small angle neutron scattering spectra (SANS) [52] indicate that, at length scales in the Porod range (10-50 Å) [56], the roughness of pore model A is in good agreement with experimental data for MCM-41 materials [47,48]. In contrast, models B and C are smooth at small length scales, in agreement with experiments, but do not exhibit the appropriate surface disorder at larger length scales. Despite the fact that none of our pore models match all the experimental data of real MCM-41 materials, they are well suited to separately study the effect of surface roughness and structural defects on the freezing behavior of Kr. Molecular simulations are well

suited for this purpose, which would be very difficult to accomplish from experiments alone.

The purpose of this chapter is to provide a preliminary account of our GCMC results for freezing of Kr within silica mesopores with an average pore diameter of 6.4 nm. Kr adsorption at low temperatures (77, 87 K) has been used in the past for characterization of porous materials with very low surface areas and volumes [57,58]. Three atomistic pore models were used: (1) the MCM-41 model developed in Refs. [51-53]; (2) a smooth, regular cylindrical pore; and (3) a cylindrical pore with constrictions. The rest of this chapter is organized as follows. Our simulation methods are presented in Section 5.1. Our main findings are presented and analyzed in Section 5.2, and finally, our concluding remarks are summarized in Section 5.3. Full details of this study will be published elsewhere [59].

5.1. Simulation Details

5.1.1. Models and methods

A detailed description of the simulation protocol used to generate and characterize our atomistic silica mesopore models has been reported elsewhere [51-53]; therefore, only a brief summary of such methodology will be presented here. Similarly, the mimetic simulation procedure to obtain mesoscale, lattice models of MCM-41 type materials has been described in detail in previous publications [54,55]. The lattice positions of the inorganic oxide segments from the mimetic simulations were scaled to obtain a material with a pore diameter $D = 6.4$ nm and a length $L = 28$ nm. We isolated one of these pores and carved out its morphology

from an atomistic box with a number of unit cells of cubic cristoballite. Following that, silicon atoms that are in an incomplete tetrahedral environment are removed, as well as oxygen atoms with two dangling bonds; oxygen atoms with one dangling bond are saturated with hydrogen atoms. This procedure ensures that all silicon atoms have no dangling bonds, all oxygen atoms have at least one saturated bond with a silicon atom, the atomistic simulation box has no net electrical charge and the pore surface is modeled in a realistic way. To mimic an amorphous silica surface, all the O, Si and H atoms were slightly displaced a random distance, and in a final step, the structure was further relaxed by performing a *NVT* Monte Carlo simulation using suitable potentials and parameters [52]. The generated atomistic silica mesopore (model A) has an average pore radius of 3.2 nm with a dispersion of ± 1 nm. This procedure to generate atomistic silica pores was originally proposed by Pellenq and Levitz [60] to model Vycor glass; Coasne *et al.* [40,42,43] showed that this technique can be used to prepare pores of various morphologies and/or topologies, such as cylindrical, hexagonal, ellipsoidal and constricted pores. We used a similar simulation protocol to generate two additional silica pores: a regular cylindrical pore with $D = 6.4$ nm (model B), and a cylindrical pore of diameter $D = 8.2$ nm with a constriction of $D = 4.1$ nm (model C). Similar constricted pores were considered in previous simulation studies [40,42,43,61,62]. The dimensions of pore model C are such that model B is an equivalent regular cylindrical pore with the same length, volume, and on average, the same degree of confinement. Both pore models B and C have a length of 15 nm, and periodic boundary conditions were applied in the axial direction for all three pore models. A schematic of the procedure used to generate the atomistic pores, as well as front views and cross sections of the three pore models used in this study are shown in Figure 5.1. Krypton was modeled as a Lennard-Jones (LJ) fluid with parameters taken from Ref. [60]: $\sigma_{ff} = 0.369$ nm, $\epsilon_{ff}/k_B = 170$ K. The interaction of Kr atoms with O, Si and H atoms in the substrate was modeled using

the PN-TraZ potentials and parameters, which have been used in the past to model gas adsorption in Vycor glass [60] and zeolites [63]. Values of the interaction parameters, as well as details of the intermolecular potential functions, can be found in the previous work by Pellenq and Levitz [60].

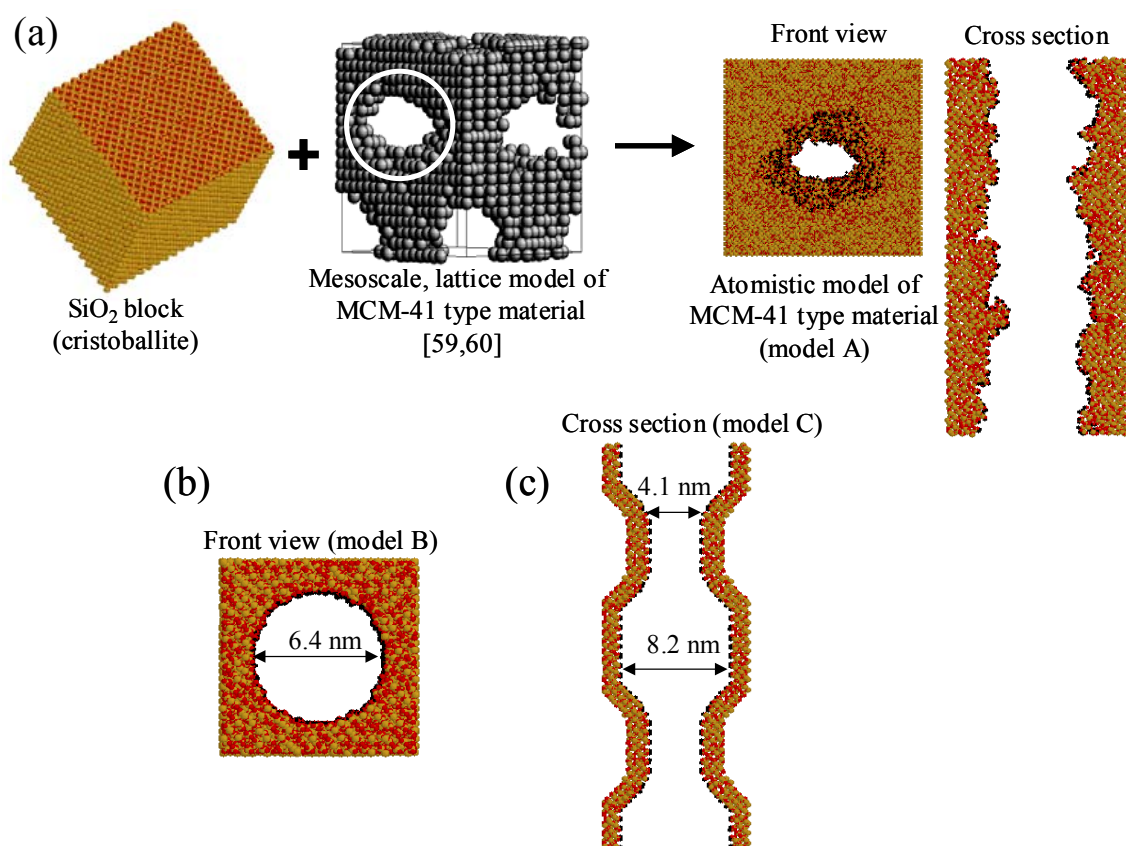


Figure 5.1. Scheme of the procedure used to generate atomistic silica pore models used in this study. Front views and/or cross sections of the three pore models are also shown. Oxygen, silicon and hydrogen atoms are depicted in red, tan and black, respectively. For model C, we have represented two simulation boxes aligned in the axial direction z .

We have used grand canonical Monte Carlo (GCMC) simulations to determine the equilibrium properties of the adsorbate within the pore. To speed up our simulation runs, we have used cell lists [64] to calculate all energy interactions; in addition, we used an energy grid [60] with an elementary cube size of about 1 \AA^3 , to

compute the adsorbate-wall potential energy. An accurate estimation of this energy is then obtained by linearly interpolating between the grid values. Thermodynamic properties were averaged over a minimum of 10^5 MC steps per particle (typical systems had up to 15000 particles); however, much longer runs were considered at lower temperatures and near the phase transitions. In our simulation runs we followed previous works [26,32,33] in choosing sets of temperature and chemical potential (T, μ) such that $\mu(T)$ corresponds to the liquid/vapor or solid/vapor coexistence pressure $P(T)$. Such a path implies that the confined phase is always in equilibrium with a saturated vapor in the bulk. The ideal gas equation and the properties of the LJ fluid at coexistence [65,66] were used to calculate the corresponding chemical potentials.

5.1.2. Structure analysis

In order to study the local freezing behavior of the adsorbate, we have measured bond order parameters that were sensitive to the degree of crystallinity in the system. No evidence of strong layering was observed, in contrast to what was observed in our previous work of freezing within multi-walled carbon nanotubes [32,33]. Therefore, to identify individual crystal-like molecules we have followed the methodology proposed by ten Wolde *et al.* [67], and measured the 3D local bond orientational order parameters $q_6(i)$, $q_4(i)$, $\hat{w}_6(i)$ and $\hat{w}_4(i)$, which are determined using the following equations:

$$q_l(i) = \left[\frac{4\pi}{2l+1} \sum_{m=-l}^l |\bar{q}_{lm}(i)|^2 \right]^{1/2} \quad (5.1)$$

$$\hat{w}_l(i) = \frac{1}{\left(\sum_{m=-l}^l |\bar{q}_{lm}(i)|^2 \right)^{3/2}} \sum_{\substack{m_1, m_2, m_3 = -l \\ m_1 + m_2 + m_3 = 0}}^l \begin{pmatrix} l & l & l \\ m_1 & m_2 & m_3 \end{pmatrix} \bar{q}_{lm_1}(i) \bar{q}_{lm_2}(i) \bar{q}_{lm_3}(i) \quad (5.2)$$

$$\bar{q}_{lm}(i) = \frac{1}{N_b(i)} \sum_{j=1}^{N_b(i)} Y_{lm}(\theta_{ij}, \phi_{ij}) \quad (5.3)$$

where θ_{ij} and ϕ_{ij} are the polar and azimuthal angles giving the orientation of a given nearest neighbor “bond” between molecules i and j , Y_{lm} are spherical harmonics [68], and the matrix in equation (5.2) is a representation of the Wigner $3J$ symbols [69]. As in our previous works [32,33], the nearest neighbors of a given particle i are those molecules j that are within a distance $r_b = 1.3\sigma_{ff}$ from particle i ; this distance corresponds to the first minimum of the radial distribution function in an fcc crystal at bulk coexistence. The 3D local order parameters $q_6(i)$, $q_4(i)$, $\hat{w}_6(i)$ and $\hat{w}_4(i)$ measure the local order around particle i ; values of these order parameters for a number of simple crystal geometries can be found in Ref. 67. Nevertheless, local order can be large for both liquid and solid, which can lead to nonzero values for the local order parameters [67]. However, in a solid the $\bar{q}_{6m}(i)$ add up coherently [which leads to nonzero values for the *global* order parameters, see equations (2.5)-(2.7)], whereas in a liquid they add up incoherently [67]. We have used this criterion to identify crystal-like molecules, and we have measured the number of coherent bonds (termed “connections”) for molecule i . Following ten Wolde *et al.* [67], for each molecule we defined a 13-dimensional complex vector $\mathbf{q}_6(i)$ with components:

$$\tilde{q}_{6m}(i) = \frac{\bar{q}_{6m}(i)}{\left(\sum_{m=-6}^6 |\bar{q}_{6m}(i)|^2 \right)^{1/2}} \quad (5.4)$$

For neighboring particles i and j , the dot product of their \mathbf{q}_6 vectors is calculated as:

$$\mathbf{q}_6(i) \cdot \mathbf{q}_6(j) = \sum_{m=-6}^6 \tilde{q}_{6m}(i) \tilde{q}_{6m}(j)^* \quad (5.5)$$

and particles i and j are “connected” if the dot product exceeds 0.5 [67]. A particle is identified as crystal-like if its number of connections is equal to, or larger than a threshold value of seven [see Ref. 67 for a discussion]. This procedure provides a measure of the local degree of crystallinity around particle i . Nishio *et al.* [36] used a slightly modified version of this method to study freezing of LJ Ar within a regular cylindrical pore of oxygen atoms mimicking a silica pore.

The freezing behavior in confinement was further analyzed by measuring renormalized 3D positional pair correlation functions $g(R)$, where R is the in-pore distance. Following the procedure reported in our previous work [33], we determined $g(R)$ for the adsorbate molecules close to the center of the pore, i.e. with reduced radial coordinate $r^* \leq 4$; in addition, we also measured a global $g(R)$ by considering all the particles inside the pore.

5.2. Results

In Figures 5.2 and 5.3 we present our results for the structure of Kr within a siliceous, regular cylindrical pore with $D = 6.4$ nm (reduced diameter

$D^* = D/\sigma_{ff} = 17.3$), at two different temperatures. At $T = 79$ K (Figure 5.2), which is well below the bulk triple point of Kr (116 K), there are a few clusters of crystal-like molecules (with seven or more coherent bonds, or connections, with their nearest neighbors); however, the confined phase exhibits a structure that is mainly non-crystalline, as can be observed from the representative simulation snapshot, the average number of connections per particle and the 3D $g(R)$ functions. At temperatures around 70 K (Figure 5.3), confined Kr experiences a change in its structure: molecules in the center of the pore exhibit a crystal-like morphology whereas particles close to the pore walls (the “surface-bound” adsorbate) still have a non-crystalline structure. The $g(R)$ function for Kr molecules with $r^* \leq 4$ suggest that those particles solidified into an fcc crystal, which is the stable crystalline structure for bulk Kr. This result is in agreement with previous experimental [15-22] and simulation [29,36] studies in silica pores of similar reduced diameters. The fcc crystal patterns can also be observed in the $g(R)$ function for the whole adsorbate, but they are not as evident as in the $g(R)$ for molecules in the center of the pore. This result contrasts to what was observed in our previous study of freezing of LJ CCl_4 within a multi-walled carbon nanotube of $D = 5.0$ nm (reduced diameter $D^* = 9.7$) [33], where the $g(R)$ function for the whole adsorbate showed no evidence of fcc crystallization (Figure 2.9). These results confirm that, as the pore diameter is reduced, the structure of the confined solid deviates more from the bulk solid morphology.

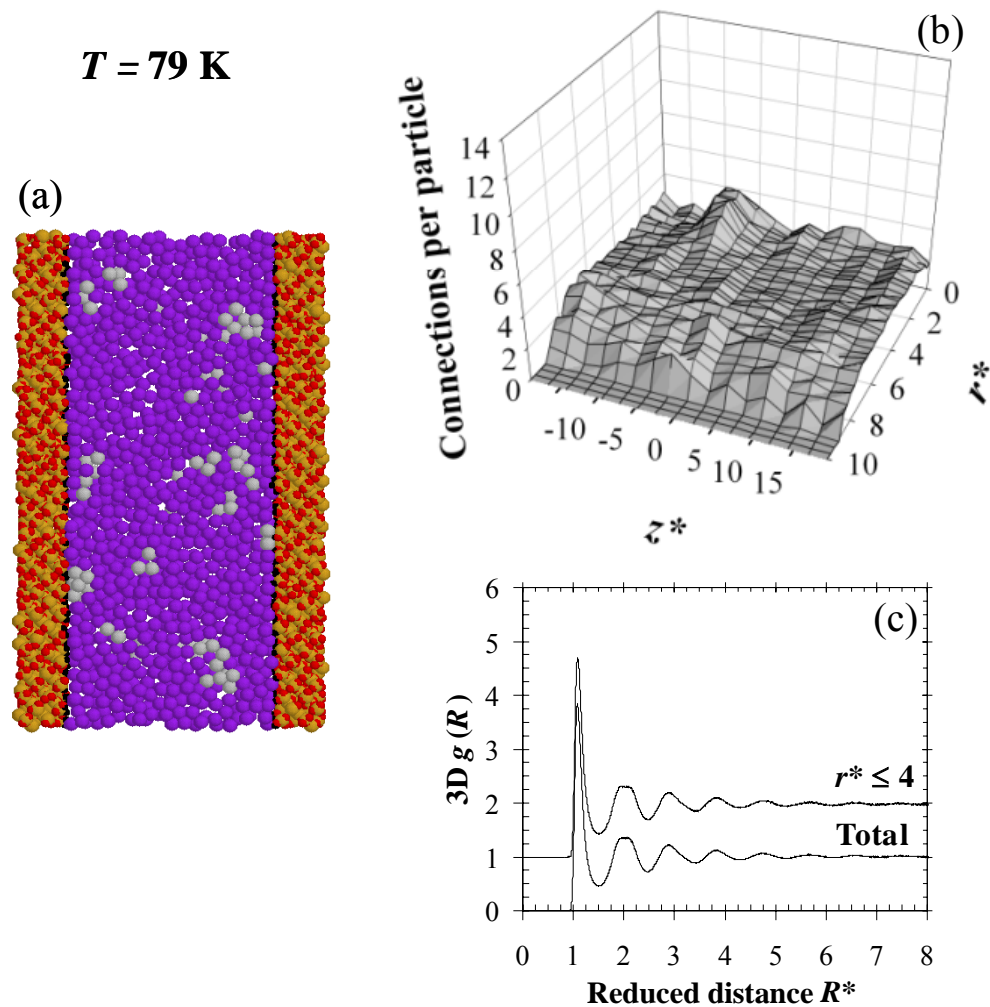


Figure 5.2. Kr within a siliceous regular cylindrical pore with $D = 6.4 \text{ nm}$ (pore model B) at $T = 79 \text{ K}$. (a) Cross section of a representative simulation snapshot. Crystal-like and noncrystal-like Kr molecules are depicted in gray and purple, respectively; oxygen, silicon and hydrogen atoms in the pore walls are represented in red, tan and black, respectively. (b) Average number of connections per particle, as a function of reduced radial and axial coordinates r^* and z^* . A Kr molecule is considered crystal-like if its number of connections is equal to or larger than seven. (c) 3D positional pair correlation functions $g(R)$ for all Kr molecules inside the pore, and for Kr molecules with $r^* \leq 4$. For clarity, the latter function has been shifted by +1.

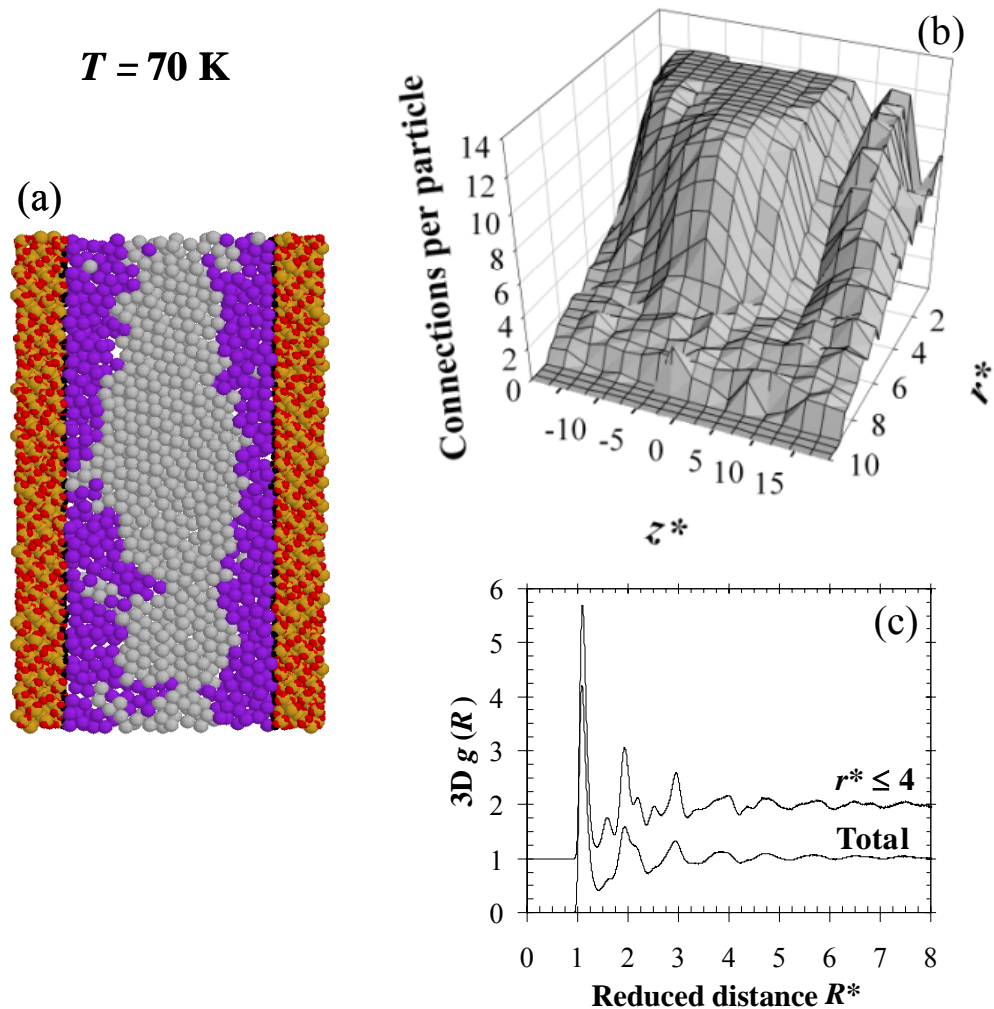


Figure 5.3. Kr within pore model B at $T=70$ K. (a) Cross section of a representative simulation snapshot. (b) Average number of connections per particle, as a function of reduced radial and axial coordinates r^* and z^* . (c) 3D positional pair correlation functions $g(R)$ for all Kr molecules inside the pore, and for Kr molecules with $r^* \leq 4$. Details are the same as in Figure 5.2.

Results for Kr confined in a cylindrical pore of $D = 8.2$ nm ($D^* = 22.2$) with a morphological defect, a constriction of $D = 4.1$ nm ($D^* = 11.1$) are presented in Figures 5.4-5.6. At $T=79$ K (Figure 5.4), confined Kr has a non-crystalline structure with patches of crystal-like molecules, as was observed for pore model B (Figure 5.2). As the temperature is reduced to $T=75$ K (Figure 5.5), we observe

the formation of a large cluster of crystal-like molecules inside the large pore cavity, with just a few small-size crystallites in the constriction. Lower temperatures ($T = 67$ K, Figure 5.6), as compared to what was obtained for pore model B ($T = 70$ K, Figure 5.3), are required for the molecules in the constriction to crystallize into an fcc structure. Particles close to the pore walls do not crystallize in this temperature range, as was observed previously for pore model B. Since pore models B and C have a similar mean pore diameter and equivalent molecular-level surface roughness, our results suggest that pore structural defects can alter the freezing behavior in confinement: Kr molecules in the constriction crystallize at lower temperatures ($T \sim 67$ K), whereas those in the big cavity crystallize at higher temperatures ($T \sim 75$ K), as compared to what was observed for crystallization in pore model B ($T \sim 70$ K). In addition, at the lowest temperatures considered in each case, the fcc-crystalline features are more evident in the $g(R)$ for the adsorbate in the central regions of pore model B [Figure 5.3 (c)], as compared to the equivalent $g(R)$ for Kr within model C [Figure 5.6 (c)]. This suggests that pore morphological defects, such as a constriction, can induce a larger number of defects in the confined crystalline phase, as compared to the case of a regular cylindrical pore.

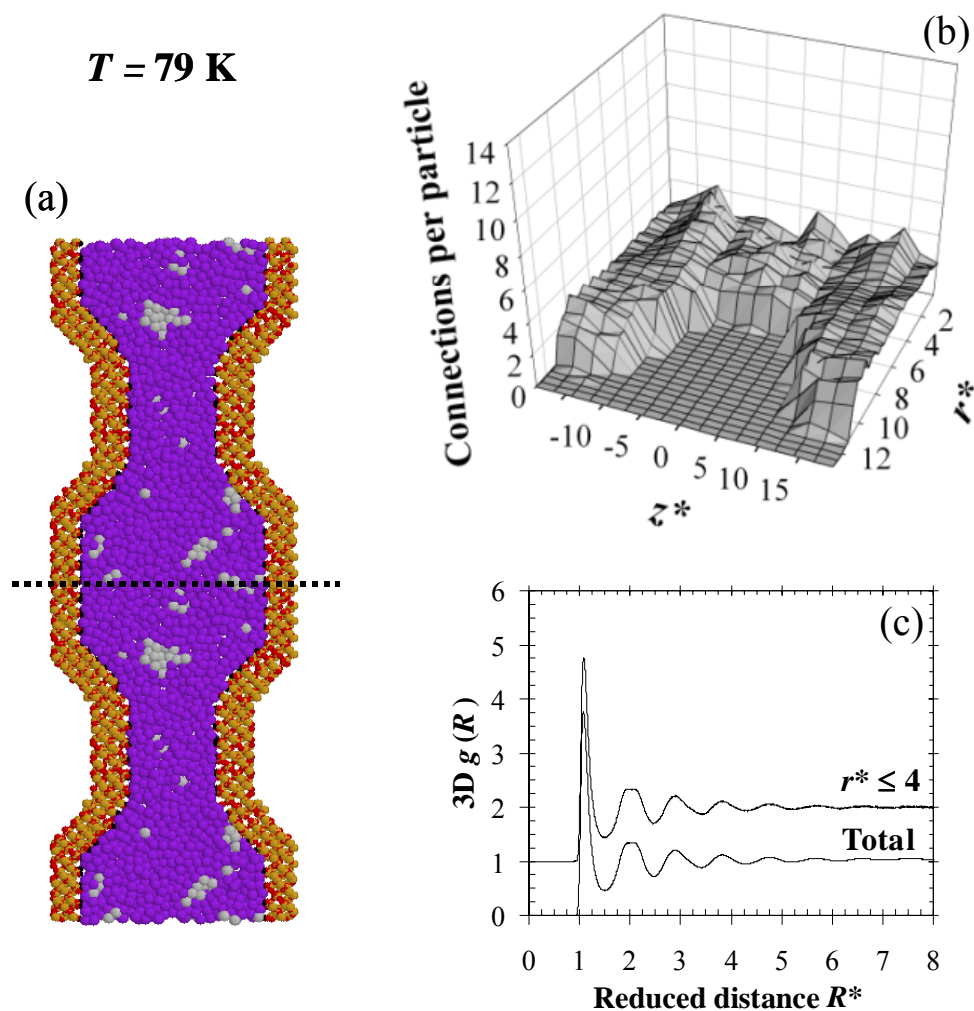


Figure 5.4. Kr within a siliceous cylindrical pore of diameter 8.2 nm with a constriction of diameter 4.1 nm (pore model C) at $T=79 \text{ K}$. (a) Cross section of a representative simulation snapshot. Crystal-like and noncrystal-like Kr molecules are depicted in gray and purple, respectively; oxygen, silicon and hydrogen atoms in the pore walls are represented in red, tan and black, respectively. We have represented two simulation boxes aligned in the axial direction z to facilitate visualization. (b) Average number of connections per particle, as a function of reduced radial and axial coordinates r^* and z^* . A Kr molecule is considered crystal-like if its number of connections is equal or larger than seven. (c) 3D positional pair correlation functions $g(R)$ for all Kr molecules inside the pore, and for Kr molecules with $r^* \leq 4$. For clarity, the latter function has been shifted by +1.

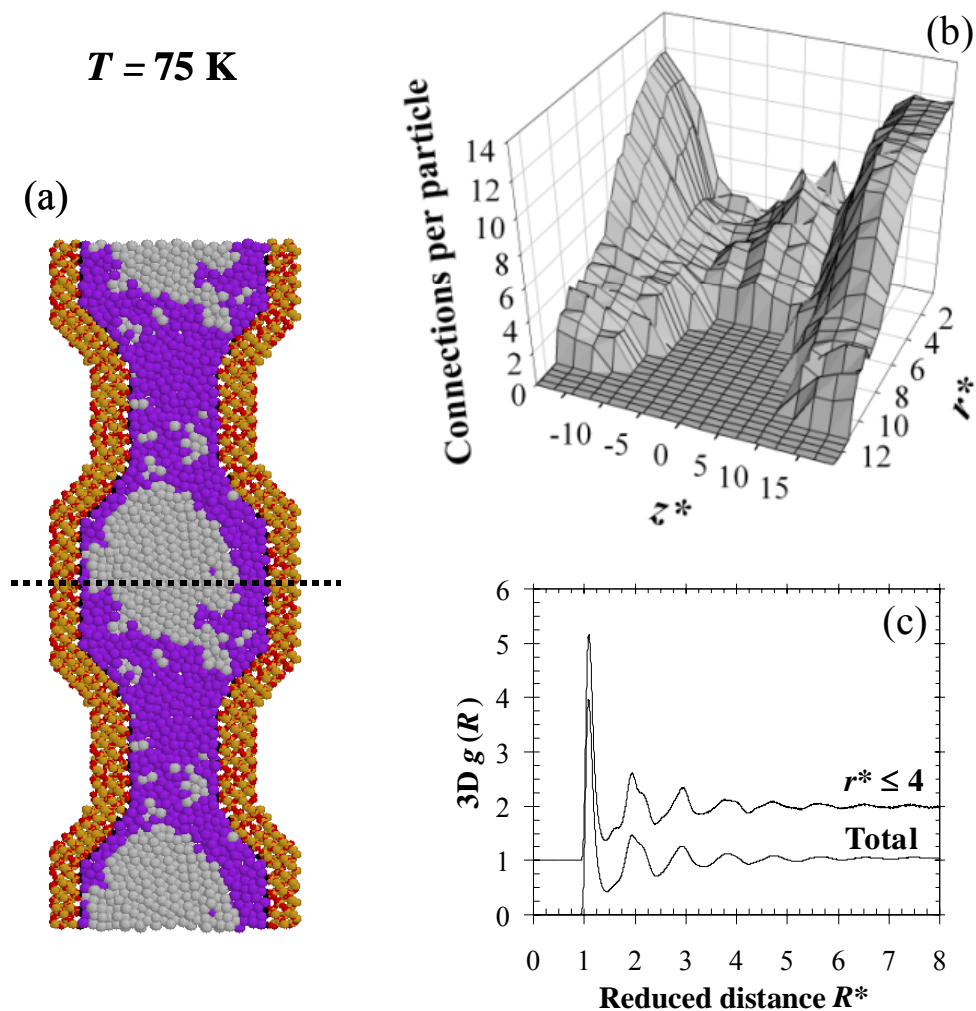


Figure 5.5. Kr within pore model C at $T=75 \text{ K}$. (a) Cross section of a representative simulation snapshot. (b) Average number of connections per particle, as a function of reduced radial and axial coordinates r^* and z^* . (c) 3D positional pair correlation functions $g(R)$ for all Kr molecules inside the pore, and for Kr molecules with $r^* \leq 4$. Details are the same as in Figure 5.4.

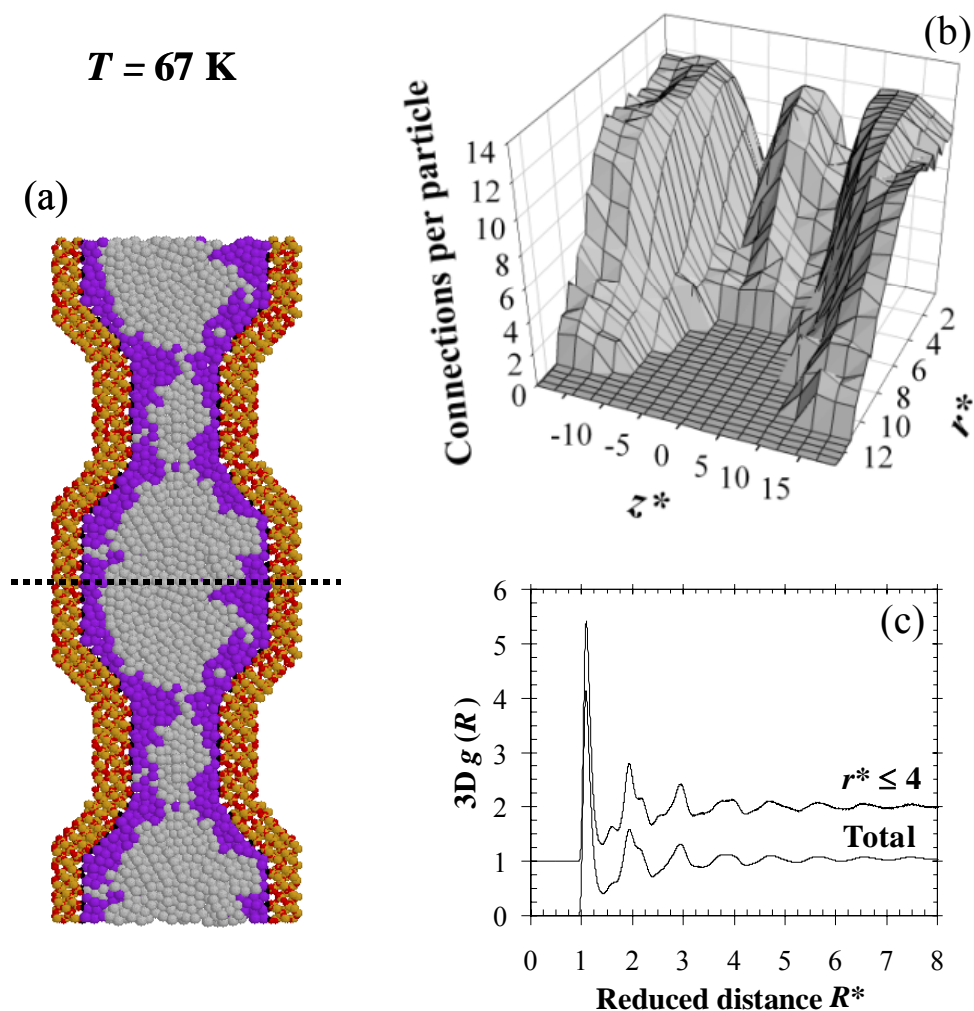


Figure 5.6. Kr within pore model C at $T=67$ K. (a) Cross section of a representative simulation snapshot. (b) Average number of connections per particle, as a function of reduced radial and axial coordinates r^* and z^* . (c) 3D positional pair correlation functions $g(R)$ for all Kr molecules inside the pore, and for Kr molecules with $r^* \leq 4$. Details are the same as in Figure 5.4.

Results for Kr confined in silica pore model A are presented in Figures 5.7 and 5.8. As was observed for pore models B and C, confined Kr has a non-crystalline structure at $T=79$ K, with a few small-size clusters of molecules with crystalline morphology. As the temperature is further reduced to 70 K (Figure 5.8), the central regions of the pore consists of relatively large patches of molecules with

crystalline and non-crystalline structure, in contrast to what was observed for pore model B where the adsorbate outside the surface-bound region presents a crystalline morphology (Figure 5.3). Pore model A exhibits an important degree of surface roughness at the molecular level, as compared to models B and C. As was observed for the case of a pore constriction, our results suggest that surface roughness can produce a decrease in the temperature at which crystallization takes place in confinement. As observed in pore models B and C, at the lowest temperature considered here we observe no evidence of crystallization in the surface-bound adsorbate. Nevertheless, we are currently performing parallel tempering Monte Carlo simulations [70] at temperatures lower than 79 K, in order to accurately determine the transition temperatures and study the low temperature behavior of both the surface-bound adsorbate and the molecules in the center of the pore.

Morishige *et al.* [15] have reported that the freezing temperature for Kr confined within SBA-15 with a mean pore diameter of 6.4 nm is $T \sim 92$ K. Our simulations give freezing temperatures inside the pore ($T \leq 70$ K) that are below the experimental value ($T \sim 92$ K). The lack of quantitative agreement between simulations and experiments could be due to several reasons. Our previous results for gas adsorption [51-53] indicate that pore model A seems to be too rough at the molecular scale, and our results suggest that surface roughness can produce a decrease in the crystallization temperature inside the pore. On the other hand, the pore morphology of models B and C at length scales in the Porod range (10-50 Å) [56] is not in agreement with experimental values [47,48], which can also produce a difference with the experimental freezing temperature in confinement. Nevertheless, our simulations show a reduction in the freezing temperature inside the pore, as compared to the bulk triple point of Kr (116 K), in qualitative agreement with the experimental results of Morishige *et al.* [15]. In addition, our

simulations provide a preliminary assessment of the effect of pore morphology and surface roughness on freezing in confinement.

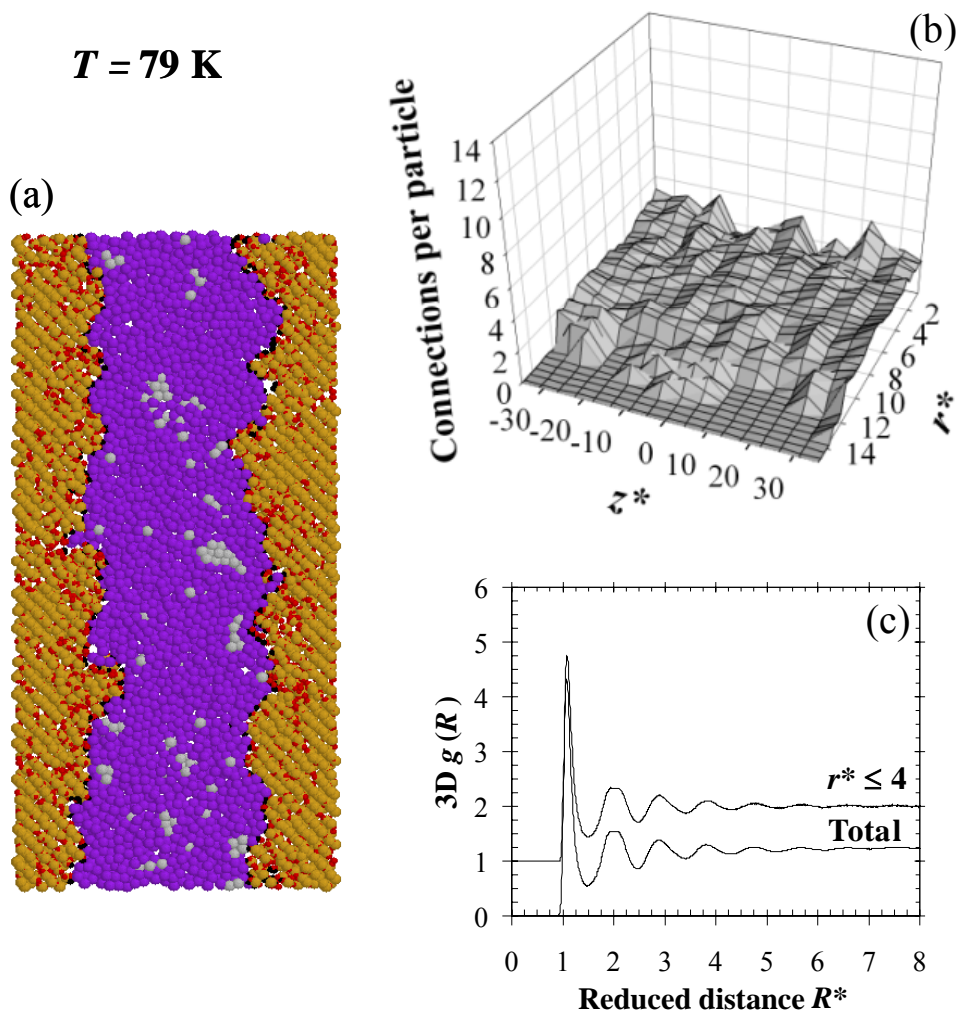


Figure 5.7. Kr within a siliceous cylindrical pore with average diameter of 6.4 nm (pore model A) at $T = 79 \text{ K}$. (a) Cross section of a representative simulation snapshot. Crystal-like and noncrystal-like Kr molecules are depicted in gray and purple, respectively; oxygen, silicon and hydrogen atoms in the pore walls are represented in red, tan and black, respectively. (b) Average number of connections per particle, as a function of reduced radial and axial coordinates r^* and z^* . A Kr molecule is considered crystal-like if its number of connections is equal or larger than seven. (c) 3D positional pair correlation functions $g(R)$ for all Kr molecules inside the pore, and for Kr molecules with $r^* \leq 4$. For clarity, the latter function has been shifted by +1.

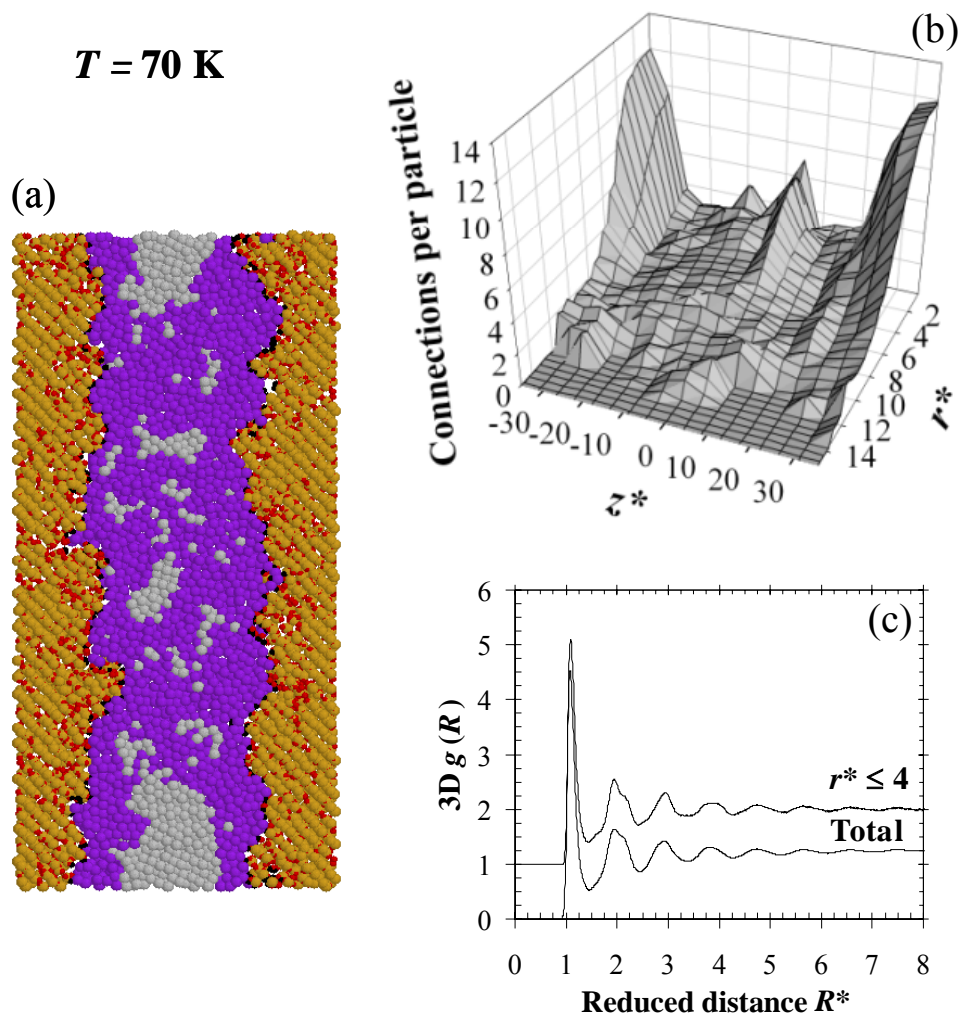


Figure 5.8. Kr within pore model A at $T=70 \text{ K}$. (a) Cross section of a representative simulation snapshot. (b) Average number of connections per particle, as a function of reduced radial and axial coordinates r^* and z^* . (c) 3D positional pair correlation functions $g(R)$ for all Kr molecules inside the pore, and for Kr molecules with $r^* \leq 4$. Details are the same as in Figure 5.7.

5.3. Concluding Remarks and Future Work

We have presented a preliminary account of our GCMC results for freezing of Kr within silica mesopores with an average pore diameter of 6.4 nm. Three atomistic pore models were used: (1) the MCM-41 model developed in Refs. [51-53] (pore model A); (2) a smooth, regular cylindrical pore (model B); and (3) a cylindrical pore of $D = 8.2$ nm with a constriction of $D = 4.1$ nm (model C). For the three pore models, we did not observe crystallization in the surface-bound adsorbate, and Kr in the center of the pore solidified into an fcc crystal (the bulk stable crystal). Our results suggest that the effect of pore constrictions and surface roughness is to decrease the temperature at which crystallization takes place inside the pore. Our simulations also suggest that these pore features can induce a larger number of defects in the confined crystalline phase. The crystallization temperatures in confinement are lower than the bulk values, in qualitative agreement with experimental studies. The lack of quantitative agreement between the freezing temperatures from our simulations and those from a recent experimental study for an equivalent system [15], suggest that improvements are required in our silica pores: model A has a somewhat excessive degree of molecular-level surface roughness, whereas at larger length scales (10-50 Å), models B and C exhibit pore morphologies that do not agree with experimental values. We are currently improving our pore models so that we obtain porous samples combining the correct atomistic roughness (similar to that for models B and C), and the correct surface disorder at larger length scales (similar to that for model A). We are also performing parallel tempering Monte Carlo simulations [70] for Kr within our silica pore models at temperatures lower than 79 K, in order to accurately determine the transition temperatures and efficiently study the low temperature behavior of both the surface-bound adsorbate and the molecules in the center of the pore. Parallel tempering techniques have been successfully used in the past to

study the freezing behavior of pure [32,33] and binary mixtures [71-74] of LJ molecules confined in strongly attractive pores. In addition, Molecular Dynamics (MD) simulations can be very useful to further analyze the nature of the confined phases (liquid, crystal or glassy).

5.4. References

-
- [1] L. D. Gelb, K. E. Gubbins, R. Radhakrishnan and M. Sliwinska-Bartkowiak, *Rep. Prog. Phys.*, 1999, **62**, 1573.
- [2] H. K. Christenson, *J. Phys.: Condens. Matter*, 2001, **13**, R95.
- [3] C. T. Kresge, M. E. Leonowicz, W. J. Roth, J. C. Vartuli and J. S. Beck, *Nature* **359**, 710 (1992).
- [4] D. Zhao, J. Feng, Q. Huo, N. Melosh, G. H. Fredrickson, B. F. Chmelka and G. D. Stucky, *Science* **279**, 548 (1998).
- [5] P. Selvam, S. K. Bhatia and C. G. Sonwane, *Ind. Eng. Chem. Res.* **40**, 3237 (2001).
- [6] G. J. de A. A. Soler-Illia, C. Sanchez, B. Lebeau and J. Patarin, *Chem. Rev.* **102**, 4093 (2002).
- [7] F. Schüth and W. Schmidt, *Adv. Mater.* **14**, 629 (2002).
- [8] M. Imperor-Clerc, P. Davidson and A. Davidson, *J. Am. Chem. Soc.* **122**, 11925 (2000).
- [9] R. Ryoo, C. H. Ko, M. Kruk, V. Antochshuk and M. Jaroniec, *J. Phys. Chem. B* **104**, 11465 (2000).
- [10] A. Galarneau, H. Cambon, F. Di Renzo and F. Fajula, *Langmuir* **17**, 8328 (2001).
- [11] S. Jun, S. H. Joo, R. Ryoo, M. Kruk, M. Jaroniec, Z. Liu, T. Ohsuna and O. Terasaki, *J. Am. Chem. Soc.* **122**, 10712 (2000).
- [12] P. L. Llewellyn, Y. Grillet, J. Rouquerol, C. Martin and J.-P. Coulomb, *Surf. Sci.* **352-354**, 468 (1996)
- [13] J. P. Coulomb, Y. Grillet, P. L. Llewellyn, C. Martin and G. André, in *Fundamentals of Adsorption 6* (F. Meunier, Ed.), Elsevier, Paris (1998), p. 147.
- [14] K. Morishige and K. Kawano, *J. Phys. Chem. B* **104**, 2894 (2000).
- [15] K. Morishige, K. Kawano and T. Hayashigi, *J. Phys. Chem. B* **104**, 10298 (2000).
- [16] K. Morishige and Y. Ogisu, *J. Chem. Phys.* **114**, 7166 (2001).

-
- [17] E. Gedat, A. Schreiber, J. Albrecht, Th. Emmler, I. Shenderovich, G. H. Findenegg, H. -H. Limbach, and G. Buntkowsky, *J. Phys. Chem. B* **106**, 1977 (2002).
- [18] G. Dosseh, Y. Xia, and C. Alba-Simionesco, *J. Phys. Chem. B* **107**, 6445 (2003).
- [19] K. Morishige, H. Uematsu and N. Tateishi, *J. Phys. Chem. B* **108**, 7241 (2004).
- [20] P. Huber and K. Knorr, *Phys. Rev. B* **60**, 12657 (1999).
- [21] D. Wallacher and K. Knorr, *Phys. Rev. B* **63**, 104202 (2001).
- [22] D. Wallacher, V. P. Soprunyuk, A. V. Kityk, and K. Knorr, *Phys. Rev. B* **66**, 014203 (2002).
- [23] V. P. Soprunyuk, D. Wallacher, P. Huber, K. Knorr, and A. V. Kityk, *Phys. Rev. B* **67**, 144105 (2003).
- [24] D. Wallacher, V. P. Sopronyuk, A. V. Kityk, P. Huber and K. Knorr, *Phys. Rev. B* **71**, 052102 (2005).
- [25] R. Denoyel and R. J.-M. Pellenq, *Langmuir* **18**, 2710 (2002).
- [26] M. Miyahara and K. E. Gubbins, *J. Chem. Phys.* **106**, 2865 (1997).
- [27] R. Radhakrishnan, K. E. Gubbins, and M. Sliwinska-Bartkowiak, *J. Chem. Phys.* **116**, 1147 (2002).
- [28] M. Maddox and K. E. Gubbins, *J. Chem. Phys.* **107**, 9659 (1997).
- [29] M. Sliwinska-Bartkowiak, J. Gras, R. Sikorski, R. Radhakrishnan, L. Gelb, and K. E. Gubbins, *Langmuir* **15**, 6060 (1999).
- [30] H. Kanda, M. Miyahara, and K. Higashitani, *Langmuir* **16**, 8529 (2000).
- [31] J. Hoffmann and P. Nielaba, *Phys. Rev. E* **67**, 036115 (2003).
- [32] F. R. Hung, G. Dudziak, M. Sliwinska-Bartkowiak and K. E. Gubbins, *Mol. Phys.* **102**, 223 (2004).
- [33] F. R. Hung, B. Coasne, K. E. Gubbins, E. E. Santiso, F. R. Siperstein and M. Sliwinska-Bartkowiak, *J. Chem. Phys.* **122**, 144706 (2005).
- [34] K. Nishio, J. Kōga, T. Yamaguchi and F. Yonezawa, *J. Phys. Soc. Japan* **73**, 627 (2004).
- [35] K. Nishio, J. Kōga, T. Yamaguchi and F. Yonezawa, *Phys. Rev. B* **69**, 214201 (2004).
- [36] K. Nishio, W. Shinoda, T. Morishita and M. Mikami, *J. Chem. Phys.* **122**, 124715 (2005).
- [37] M. W. Maddox, J. P. Olivier and K. E. Gubbins, *Langmuir* **13**, 1737 (1997).
- [38] C. A. Koh, T. Montanari, R. I. Nooney, S. F. Tahir and R. E. Westacott, *Langmuir* **15**, 6043 (1999).
- [39] L. D. Gelb, *Mol. Phys.* **100**, 2049 (2002).
- [40] B. Coasne, A. Grosman, C. Ortega and R. J. M. Pellenq, *Stud. Surf. Sci. Catal.* **144**, 35 (2002).
- [41] Y. He and N. A. Seaton, *Langmuir* **19**, 10132 (2003).

-
- [42] B. Coasne and R. J.-M. Pellenq, *J. Chem. Phys.* **121**, 3767 (2004).
- [43] B. Coasne and R. J.-M. Pellenq, *J. Chem. Phys.* **120**, 2913 (2004).
- [44] J. P. Fox and S. P. Bates, *Langmuir* **21**, 4746 (2005).
- [45] V. B. Fenelonov, A. Y. Derevyankin, S. D. Kirik, L. A. Solovyov, A. N. Shmakov, J.-L. Bonardet, A. Gedeon and V. N. Romannikov, *Micropor. Mesopor. Mat.* **44-45**, 33 (2001).
- [46] A. Berenguer-Murcia, J. García-Martínez, D. Cazorla-Amorós, A. Martínez-Alonso, J. M. D. Tascón and A. Linares-Solano, *Stud. Surf. Sci. Catal.* **144**, 83 (2002).
- [47] K. J. Edler, P. A. Reynolds and J. W. White, *J. Phys. Chem. B* **102**, 3676 (1998).
- [48] C. G. Sonwane, S. K. Bhatia and N. J. Calos, *Langmuir* **15**, 4603 (1999).
- [49] L. D. Gelb and K. E. Gubbins, *Langmuir* **14**, 2097 (1998).
- [50] L. D. Gelb and K. E. Gubbins, *Mol. Phys.* **96**, 1795 (1999).
- [51] B. Coasne, F. R. Hung, F. R. Siperstein and K. E. Gubbins, *Ann. Chim-Sci. Mat.*, in press (2005).
- [52] B. Coasne, F. R. Hung, R. J.-M. Pellenq, F. R. Siperstein and K. E. Gubbins, *Langmuir*, submitted (2005).
- [53] F. R. Hung, B. Coasne, K. E. Gubbins, F. R. Siperstein, M. Thommes and M. Sliwiska-Bartkowiak, *Stud. Surf. Sci. Catal.*, accepted (2005).
- [54] F. R. Siperstein and K. E. Gubbins, *Mol. Sim.* **27**, 339 (2001).
- [55] F. R. Siperstein and K. E. Gubbins, *Langmuir* **19**, 2049 (2003).
- [56] J. D. F. Ramsay, *Adv. Coll. Interface Sci.* **76-77**, 13 (1998).
- [57] S. J. Gregg and K. S. W. Sing, *Adsorption, Surface Area and Porosity*, 2nd edition, Academic Press, London (1982).
- [58] T. Takei and M. Chikazawa, *J. Ceram. Soc. Jpn.* **106**, 353 (1998).
- [59] F. R. Hung, B. Coasne, M. Sliwiska-Bartkowiak and K. E. Gubbins, *Phys. Rev. B*, to be submitted (2005).
- [60] R. J.-M. Pellenq and P. E. Levitz, *Mol. Phys.* **100**, 2059 (2002).
- [61] L. Sarkisov and P. A. Monson, *Langmuir* **17**, 7600 (2001).
- [62] A. Vishnyakov and A. V. Neimark, *Langmuir* **19**, 3240 (2003).
- [63] R. J.-M. Pellenq and D. Nicholson, *J. Phys. Chem.*, 98 (1994) 13339.
- [64] D. Frenkel and B. Smit, *Understanding Molecular Simulation: from Algorithms to Applications*, 2nd ed., Academic Press, London (2002).
- [65] D. A. Kofke, *J. Chem. Phys.* **98**, 4149 (1993).
- [66] R. Agrawal and D. A. Kofke, *Mol. Phys.* **85**, 43 (1995).
- [67] P. R. ten Wolde, M. J. Ruiz-Montero and D. Frenkel, *J. Chem. Phys.* **104**, 9932 (1996).
- [68] C. G. Gray and K. E. Gubbins, *Theory of Molecular Liquids*, Clarendon Press, Oxford (1984).

-
- [69] L. D. Landau and E. M. Lifshitz, *Quantum Mechanics*, Pergamon Press, New York (1965).
- [70] Q. Yan and J. J. de Pablo, *J. Chem. Phys.* **111**, 9509 (1999).
- [71] B. Coasne, K. E. Gubbins, F. R. Hung and M. Sliwinska-Bartkowiak, *Mol. Phys.* **102**, 2149 (2004).
- [72] B. Coasne, J. Czwartos, K. E. Gubbins, F. R. Hung and M. Sliwinska-Bartkowiak, *Adsorption* **11**, 301 (2005).
- [73] J. Czwartos, B. Coasne, K. E. Gubbins, F. R. Hung and M. Sliwinska-Bartkowiak, *Mol. Phys.*, in press (2005).
- [74] B. Coasne, J. Czwartos, K. E. Gubbins, F. R. Hung and M. Sliwinska-Bartkowiak, *Stud. Surf. Sci. Catal.*, accepted (2005).

Chapter 6

Conclusions and Future Directions

In this work we have presented a molecular simulation study aimed at understanding the phase behavior of pure, simple Lennard-Jones (LJ) fluids, when they are confined inside nanopores of cylindrical geometry. Our efforts have concentrated on studying freezing/melting transitions in non-interconnected pores that are completely filled with adsorbate molecules. We have performed two independent, but directly related studies: (1) freezing of carbon tetrachloride within multi-walled carbon nanotubes (MWCNT), and (2) capillary condensation and freezing of krypton within templated mesoporous silica materials (MCM-41). MWCNT are representative of materials with strongly attractive walls, i.e. the wall-adsorbate interactions are stronger than the adsorbate-adsorbate interactions. In contrast, for Kr within MCM-41 the wall-adsorbate interactions are weaker than the Kr-Kr interactions. One part of the latter series of studies was the development of atomistic models of MCM-41 type materials that include pore morphological defects and surface roughness. Therefore, we have included results for gas-liquid (capillary condensation) equilibria, since a comparison between simulation and experimental results for gas adsorption provide an assessment of our pore models as compared to the real material.

In the first part of our project, we performed a combined experimental and molecular simulation study [1-3] on freezing and melting of CCl_4 confined within open-tip MWCNT of diameter $D = 5.0$ nm ($D^* = D/\sigma_{ff} = 9.7$). The structure and thermodynamic stability of the confined phases, as well as the temperatures and the order of the phase transitions, were determined from parallel tempering grand canonical Monte Carlo simulations and free energy calculations. The multiple

transition temperatures observed in the simulations were consistent with the experimental transition temperatures, as determined from dielectric relaxation spectroscopy measurements. The simulations show that the adsorbate forms concentric molecular layers that solidify into quasi-2D hexagonal crystals with defects. Freezing in such layers occur via intermediate phases that show remnants of hexatic behavior, in direct analogy to the freezing mechanism previously described for LJ particles confined within slit pores [4,5]. The freezing/melting transitions in the layers close to the pore walls take place at temperatures above the bulk freezing point. In contrast, the adsorbate in the inner regions of the pore solidifies into frustrated crystals with a large number of defects at temperatures well below the bulk freezing point, due to the strong geometrical constraints. The simulations show evidence of a rich phase behavior in confinement. Five different phases were observed for this particular pore diameter. Some of these phases were found to be inhomogeneous (i.e. combinations of crystalline, liquid and frustrated crystalline regions) and stable over extended temperature ranges.

We also studied the effect of confinement on freezing and melting of CCl_4 inside open-tip MWCNT of different pore sizes [3,6]. Two different pore diameters D were considered in our dielectric relaxation spectroscopy measurements, 4.0 and 2.8 nm. The freezing behavior of LJ CCl_4 within model MWCNT of similar diameters, 3.9 and 2.8 nm ($D^* = 7.5$ and 5.5), was also investigated by means of molecular simulations in the grand canonical ensemble. A single transition temperature that was well above the bulk melting point was obtained for both pore sizes. These results contrast with our previous measurements using MWCNT with a pore diameter of 5.0 nm [1-3], where multiple transition temperatures above and below the bulk melting point of CCl_4 were observed. Our experimental measurements were in qualitative agreement with our molecular simulation results. Although the simulations overestimate the temperatures in which melting upon

confinement occurs, both simulations and experiments suggest that all regions of adsorbate freeze at the same temperature, and freezing occurs at higher temperatures upon reduction of the pore diameter. As observed for the case of $D = 5.0$ nm [1-3], the adsorbate within the smaller MWCNT forms concentric layers that solidify into quasi-2D hexagonal crystals with defects. Similarly, freezing in these layers take place via intermediate phases showing remnants of hexatic behavior. Due to strong geometrical constraints, the adsorbate in the inner regions of the smaller MWCNTs forms a highly localized row of particles at the center of the pore, exhibiting increases in the local density ρ_{inner}^* . All structure changes take place at temperatures above the bulk freezing point. Three different structures, some of them inhomogeneous, were found for the two pore sizes examined ($D = 3.9$ and 2.8 nm).

Further experiments with different techniques are needed to corroborate our observations. Differential scanning calorimetry experiments can help in corroborating the measured transition temperatures, while techniques such as x-ray diffraction, nuclear magnetic resonance (NMR) and neutron scattering are suitable to determine the structure of the adsorbed phase. From the simulation viewpoint, it would be interesting to determine the effect of bulk pressure on freezing in regular cylindrical pores; such an effect has been studied in the past for slit pores [7,8]. Moreover, calculations of the pressure in the radial and axial directions inside the pore can be used as a test of the mechanical stability of the structures obtained in our freezing studies. Another interesting study would be to analyze the possibility of solid-solid transformations within each layer of adsorbate upon changes on the diameter of the regular cylindrical pore, in direct analogy with previous studies in slit pore geometries [9-12].

In the second part of our project, we first developed an atomistic silica mesopore model [13-15] that keeps the morphological features of the MCM-41 lattice model of Siperstein and Gubbins [16,17]. The porous material was generated by carving out of a silica block, the skeleton of the MCM-41 pore that was obtained from lattice Monte Carlo simulations. In doing this “downscaling” process, atomic details were included in our model, more accurate potentials were used to represent the adsorbate-wall interactions, and the effect of pore surface roughness and structural defects on the adsorbate phase behavior were assessed. We first studied the effect of such variables on the gas-liquid equilibria in confinement, by performing Grand Canonical Monte Carlo (GCMC) simulations of krypton adsorption at 100 K and 87 K. Three pore models with an average pore diameter of 6.4 nm were considered in this study: 1) a pore that keeps the morphological features of the mesoscale model of Siperstein and Gubbins (model A); 2) a pore with regular cylindrical shape (model B); and 3) a cylindrical pore of $D = 8.2$ nm with constrictions of $D = 4.1$ nm (model C). Adsorption isotherms and isosteric heats of adsorption were measured for Kr [14]; similar results for argon and xenon adsorption were presented in other publications [13,15]. Surface roughness and structural defects significantly affect gas adsorption: marked differences were observed in the adsorption isotherms, isosteric heat curves and pore filling mechanisms. For instance, the adsorption branch for model A corresponds to a quasi-continuous pore filling involving coexistence of liquid-like “bridges” and gas-like regions, while the discontinuous adsorption branch for model B conforms to the classical picture of capillary condensation in regular nanopores. Adsorption on model C exhibits features from both models A and B, namely a pore filling mechanism with coexistence of hemispherical gas-liquid interfaces and condensed regions, and a discontinuous adsorption curve. It was also found that the features of the adsorption/desorption cycles for model A depend on the adsorbate: a large hysteresis loop with asymmetrical adsorption and desorption branches was

observed for Ar [13] and Kr [14], but the adsorption/desorption isotherm for Xe in model A [13,15] was composed of both reversible/continuous and slightly irreversible/discontinuous paths. In contrast, symmetrical hysteresis loops were always obtained for the regular cylindrical nanopore (model B).

Our results suggest that the degree of surface disorder for pore model A is too high at the molecular level, but its simulated small angle neutron scattering spectrum (SANS) shows that its roughness at larger length scales (10-50 Å) is in agreement with MCM-41 experimental results [18,19]. In contrast, models B and C are smooth at molecular length scales, but do not exhibit the appropriate surface disorder at length scales around 10-50 Å. We are currently trying to improve our models of MCM-41 porous materials, by starting from model A and using efficient relaxation techniques to reconstruct the surface of the pore. This may allow us to obtain porous samples combining the correct atomistic roughness (similar to that for model B and C) and the correct surface disorder at larger length scales (similar to that for model A). We are also extending our work to develop realistic models [20] of SBA-15 materials, i.e. silica mesopores linked through microporous interconnections [21,22]; mesoscale, lattice models of these materials are already available [23].

We also have presented a preliminary account of our GCMC results for freezing of Kr within silica mesopores, aimed at determining the effect of surface roughness and morphological defects on the transition temperatures and the structure of the confined phases. We have used the same three pore models described before, with an average pore diameter of 6.4 nm ($D^* = 17.3$). Full details of this study will be published elsewhere [24]. For the three pore models, we did not observe crystallization in the surface-bound adsorbate, and Kr in the center of the pore solidified into an fcc crystal (the bulk stable crystal). In contrast, our previous

studies [1-3,6] have showed that solid structures different from those observed in bulk systems are obtained for freezing inside pores of $D^* \leq 9.7$. Our results suggest that the effect of pore surface roughness and morphological defects, such as constrictions, is to decrease the temperature at which crystallization takes place inside the pore. Our simulations also suggest that these pore features can induce a larger number of defects in the confined crystalline phase. The crystallization temperatures in confinement are lower than the bulk values, in qualitative agreement with experimental studies [25], and in contrast to what was observed for CCl_4 freezing within MWCNT [1-3,6]. The lack of quantitative agreement between the freezing temperatures from our simulations and those from a recent experimental study for an equivalent system [25], suggest that improvements are required in our silica pores. We are also performing parallel tempering Monte Carlo simulations [26] for Kr within our silica pore models at temperatures lower than 79 K, in order to accurately determine the transition temperatures and efficiently study the low temperature behavior of both the surface-bound adsorbate and the molecules in the center of the pore. Parallel tempering techniques have been successfully used in the past to study the freezing behavior of pure [1,3] and binary mixtures [27-30] of LJ molecules confined in strongly attractive pores. In addition, we will perform Molecular Dynamics (MD) simulations to further analyze the nature of the confined phases (liquid, crystal or glassy).

Straightforward extensions of this work include studying the freezing behavior of other adsorbates in simple pore geometries (slit, regular cylinder). For example, it would be of interest to model CCl_4 with a five-site interaction potential [31]. Other examples can include simple dipolar fluids [32] and water [33,34]. Another direct extension of this project would be to use molecular simulation to study freezing transitions in pores that are not completely filled with adsorbate. For example, differential scanning calorimetry results in partially filled MCM-41 and SBA-15

pores suggest that, upon reduction of temperature, a liquid-like film of water adsorbed on the pore walls crystallizes; such a phenomena is not observed for completely filled pores or for melting [35]. Finally, we have shown that our methodology can be used to study freezing/melting of fluids inside complex pore geometries. Realistic models of other porous materials, such as silica glasses [36,37] and carbons [38,39] are available, and our methods can be easily extended to study freezing within such models. For complex models of porous carbons, a very recent molecular simulation study [40] shows evidence of solid-like N₂ in confinement, at temperatures higher than the bulk freezing point; studies of freezing within other models of porous carbons [38,39] are currently in progress [41].

References

- [1] F. R. Hung, G. Dudziak, M. Sliwinska-Bartkowiak and K. E. Gubbins, *Mol. Phys.* **102**, 223 (2004).
- [2] M. Sliwinska-Bartkowiak, F. R. Hung, E. E. Santiso, B. Coasne, F. R. Siperstein and K. E. Gubbins, *Adsorption* **11**, 391 (2005).
- [3] F. R. Hung, B. Coasne, K. E. Gubbins, E. E. Santiso, F. R. Siperstein and M. Sliwinska-Bartkowiak, *J. Chem. Phys.* **122**, 144706 (2005).
- [4] R. Radhakrishnan, K. E. Gubbins and M. Sliwinska-Bartkowiak, *J. Chem. Phys.* **116**, 1147 (2002).
- [5] R. Radhakrishnan, K. E. Gubbins and M. Sliwinska-Bartkowiak, *Phys. Rev. Lett.* **89**, 076101 (2002).
- [6] M. Jazdzewska, F. R. Hung, K. E. Gubbins and M. Sliwinska-Bartkowiak, *Phys. Chem. Chem. Phys.*, submitted (2005).
- [7] M. Miyahara, H. Kanda, M. Shibao and K. Higashitani, *J. Chem. Phys.* **112**, 9909 (2000).
- [8] H. Kanda, M. Miyahara and K. Higashitani, *J. Chem. Phys.* **120**, 6173 (2004).
- [9] C. Ghatak and K. G. Ayappa, *Phys. Rev. E* **64**, 051507 (2001); K. G. Ayappa and C. Ghatak, *J. Chem. Phys.* **117**, 5373 (2002).
- [10] A. Vishnyakov and A. V. Neimark, *J. Chem. Phys.* **118**, 7585 (2003).
- [11] A. Patrykiewicz, L. Sałamacha, and S. Sokołowski, *J. Chem. Phys.* **118**, 1891 (2003).

-
- [12] H. Bock, K. E. Gubbins and K. G. Ayappa, *J. Chem. Phys.* **122**, 094709 (2005).
- [13] B. Coasne, F. R. Hung, R. J.-M. Pellenq, F. R. Siperstein and K. E. Gubbins, *Langmuir*, submitted (2005).
- [14] F. R. Hung, B. Coasne, K. E. Gubbins, F. R. Siperstein, M. Thommes and M. Sliwinska-Bartkowiak, *Stud. Surf. Sci. Catal.*, accepted (2005).
- [15] B. Coasne, F. R. Hung, F. R. Siperstein and K. E. Gubbins, *Ann. Chim-Sci. Mat.*, in press (2005).
- [16] F. R. Siperstein and K. E. Gubbins, *Mol. Sim.* **27**, 339 (2001).
- [17] F. R. Siperstein and K. E. Gubbins, *Langmuir* **19**, 2049 (2003).
- [18] K. J. Edler, P. A. Reynolds and J. W. White, *J. Phys. Chem. B* **102**, 3676 (1998).
- [19] C. G. Sonwane, S. K. Bhatia and N. J. Calos, *Langmuir* **15**, 4603 (1999).
- [20] A preliminary account of this work is presented in S. Bhattacharya, B. Coasne, F. R. Hung and K. E. Gubbins, *Stud. Surf. Sci. Catal.*, accepted (2005).
- [21] D. Zhao, J. Feng, Q. Huo, N. Melosh, G. H. Fredrickson, B. F. Chmelka and G. D. Stucky, *Science* **279**, 548 (1998).
- [22] A. Galarneau, H. Cambon, F. Di Renzo, R. Ryoo, M. Choi and F. Fajula, *New J. Chem.* **27**, 73 (2003).
- [23] S. Bhattacharya and K. E. Gubbins, *J. Chem. Phys.*, accepted (2005).
- [24] F. R. Hung, B. Coasne, M. Sliwinska-Bartkowiak and K. E. Gubbins, *Phys. Rev. B*, to be submitted (2005).
- [25] K. Morishige, K. Kawano and T. Hayashigi, *J. Phys. Chem. B* **104**, 10298 (2000).
- [26] Q. Yan and J. J. de Pablo, *J. Chem. Phys.* **111**, 9509 (1999).
- [27] B. Coasne, K. E. Gubbins, F. R. Hung and M. Sliwinska-Bartkowiak, *Mol. Phys.* **102**, 2149 (2004).
- [28] B. Coasne, J. Czwartos, K. E. Gubbins, F. R. Hung and M. Sliwinska-Bartkowiak, *Adsorption* **11**, 301 (2005).
- [29] J. Czwartos, B. Coasne, K. E. Gubbins, F. R. Hung and M. Sliwinska-Bartkowiak, *Mol. Phys.*, in press (2005).
- [30] B. Coasne, J. Czwartos, K. E. Gubbins, F. R. Hung and M. Sliwinska-Bartkowiak, *Stud. Surf. Sci. Catal.*, accepted (2005).
- [31] For example, see L. S. Bartell and J. Chen, *J. Phys. Chem.* **96**, 8801 (1992); T. M. Chang, K. A. Peterson and L. X. Dang, *J. Chem. Phys.* **103**, 7502 (1995); J.-C. Soetens, G. Jansen and C. Millot, *Mol. Phys.* **96**, 1003 (1999).
- [32] S. H. L. Klapp and M. Schoen, *J. Chem. Phys.* **117**, 8050 (2002).
- [33] K. Koga, G.T. Gao, H. Tanaka and X.C. Zeng, *Nature* **412**, 802 (2001).
- [34] W. H. Noon, K. D. Ausman, R. E. Smalley and J. Ma, *Chem. Phys. Lett.* **355**, 445 (2002).

-
- [35] A. Schreiber, I. Ketelsen and G. H. Findenegg, *Phys. Chem. Chem. Phys.* **3**, 1185 (2001).
- [36] L. D. Gelb and K. E. Gubbins, *Langmuir* **14**, 2097 (1998)
- [37] R. J.-M. Pellenq and P. E. Levitz, *Mol. Phys.* **100**, 2059 (2002).
- [38] J. Pikunic, C. Clinard, N. Cohaut, K. E. Gubbins, J. M. Guet, R. J.-M. Pellenq, I. Rannou and J.-N. Rouzaud, *Langmuir* **19**, 8565 (2003).
- [39] S. K. Jain, J. Pikunic, R. J.-M. Pellenq and K. E. Gubbins, *Adsorption* **11**, 355 (2005).
- [40] M. J. Biggs, A. Buts and D. Williamson, *Langmuir* **20**, 5786 (2004).
- [41] B. Coasne *et al.*, in preparation (2005).